ENFOQUE UTE

REVISTA

Facultad Ciencias de la Ingeniería e Industrias
eISSN:13906542

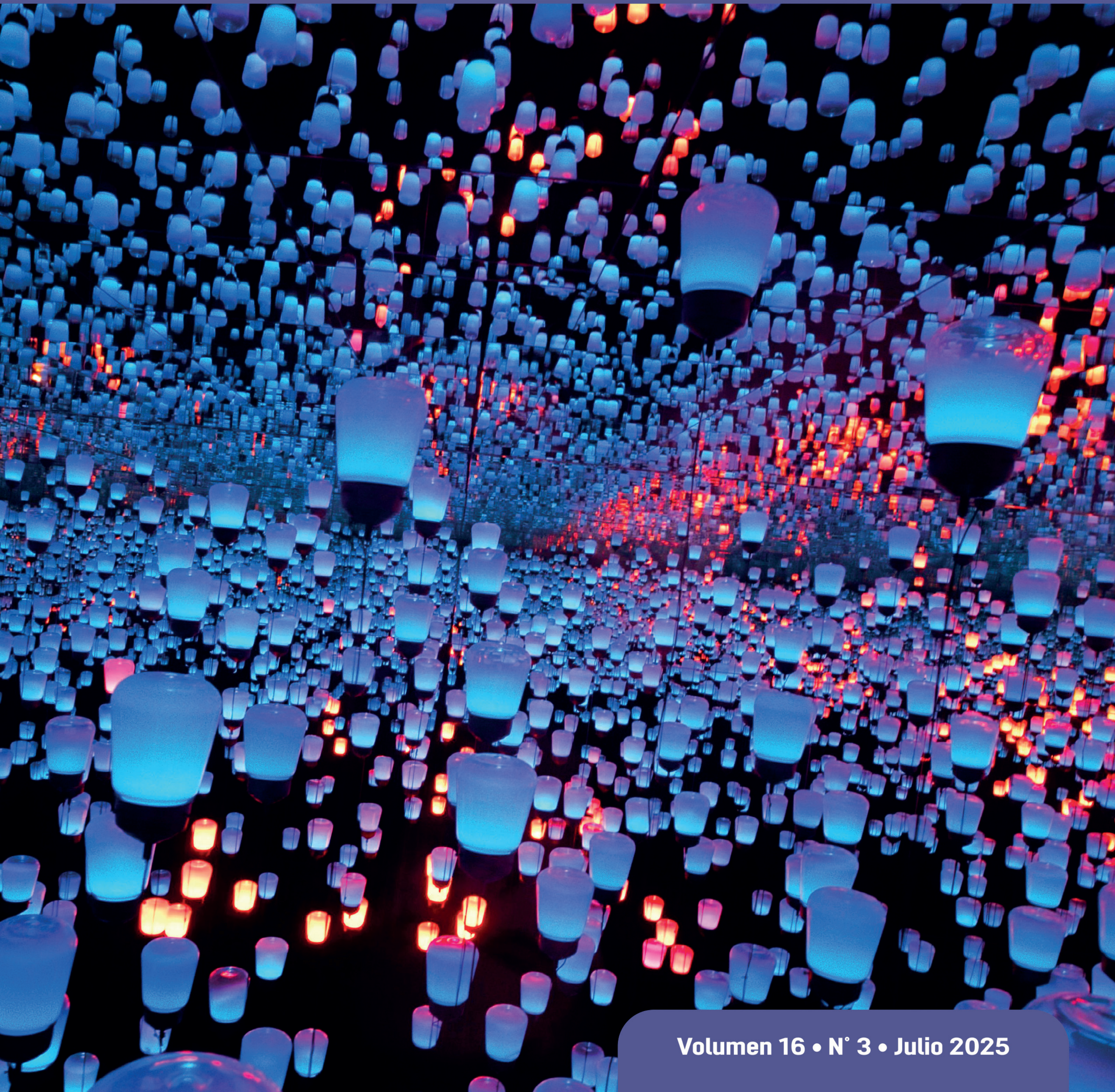

Volumen 16 • N° 3 • Julio 2025

Sumario

ENFOQUE UTE REVISTA
Facultad Ciencias de la Ingeniería e Industrias
eISSN:13906542

Editorial

It is a pleasure to present Volume 16, Issue 3 of Enfoque UTE, which features six original Research Articles covering several areas of engineering. Each article included in this issue has undergone a rigorous peer-review process by at least two national and international experts, ensuring both scientific relevance and technical quality.

The issue opens with a contribution by Darío Calderón et al., who present an experimental study on sediment transport and flow behavior in a bifurcated open channel with a mobile sand bed—advancing our understanding of fluvial dynamics in environmental and hydraulic engineering.

Continuing with this issue, J. E. López Velástegui et al. present a study of the development of a biodegradable plate made from sugarcane bagasse, proposing a sustainable alternative to disposable plastics.

Another important contribution is presented by Cristian H. Martínez-Reátegui et al. This research team presents the design and evaluation of an aerodynamic fairing for electric motorcycles using CFD and FEA simulations. This research contributes to the fields of mechanical and electrical engineering, with implications for sustainable mobility and energy efficiency.

In the area of environmental engineering, Vianey A. Burboa Charis et al. present a study on enhancing methane production from nixtamalization wastewater using iron-impregnated activated carbon. The results provide new insights into anaerobic digestion processes and the use of conductive materials for environmental biotechnology applications.

In the area of food and agricultural engineering, Monserrath Vásquez et al. develop and characterize a yogurt-like product based on Lupinus mutabilis and arracacha starch. Their study bridges nutrition, microbiology, and functional plant-based food development, addressing the growing demand for sustainable and health-oriented products.

Finally, Stephanny H. Briones Zambrano et al. evaluate the effects of different weed control techniques on the early growth of Schizolobium parahyba, contributing to sustainable forestry practices and offering useful insights for agricultural and natural resource management.

Together, these six articles demonstrate the interdisciplinary nature of the journal and its commitment to supporting research that connects innovation with real-world applications. We hope this issue will be of great interest to researchers and practitioners working across the diverse fields represented in Enfoque UTE.

Dr. Oscar Martínez Mozos
Universidad Politécnica de Madrid
Editor-in-Chief

Dr. Diego Guffanti Martínez
Universidad UTE
Editor-in-Chief

Dr. Wilson Pavón
Universidad UTE
Managing Editor

ENFOQUE
UTE
REVISTA
Facultad Ciencias de la Ingeniería e Industrias
eISSN:13906542

Editorial

UTE EC

Es un placer presentar el *Volumen 16, Número 3* de *Enfoque UTE*, el cual presenta seis Artículos de Investigación originales que abarcan varias áreas de la ingeniería. Cada artículo incluido en este número ha pasado por un riguroso proceso de revisión por pares realizado por al menos dos expertos nacionales e internacionales, lo que garantiza tanto la relevancia científica como la calidad técnica.

El número comienza con una contribución de Darío Calderón et al., quienes presentan un estudio experimental sobre el transporte de sedimentos y el comportamiento del flujo en un canal abierto bifurcado con un lecho móvil de arena, lo que mejora nuestra comprensión de la dinámica fluvial en la ingeniería ambiental e hidráulica.

Continuando con este número, J. E. López Velástegui et al. presentan un estudio sobre el desarrollo de un plato biodegradable hecho a partir de bagazo de caña de azúcar, proponiendo una alternativa sostenible a los plásticos desechables.

Otra contribución importante es presentada por Cristian H. Martínez-Reátegui et al.. Este equipo de investigación presenta el diseño y la evaluación de un carenado aerodinámico para motocicletas eléctricas utilizando simulaciones CFD y FEA. Esta investigación contribuye a los campos de la ingeniería mecánica y eléctrica, con implicaciones para la movilidad sostenible y la eficiencia energética.

En el área de ingeniería ambiental, Vianey A. Burboa Charis et al. presentan un estudio sobre el aumento de la producción de metano a partir de aguas residuales de nixtamalización utilizando carbón activado impregnado con hierro. Los resultados proporcionan nuevas perspectivas sobre los procesos de digestión anaerobia y el uso de materiales conductores para aplicaciones de biotecnología ambiental.

En el área de la ingeniería alimentaria y agrícola, Monserrath Vásquez et al. desarrollan y caracterizan un producto tipo yogurt a base de *Lupinus mutabilis* y almidón de arracacha. Su estudio conecta nutrición, microbiología y el desarrollo de alimentos funcionales de origen vegetal, abordando la creciente demanda de productos sostenibles y orientados a la salud.

Finalmente, Stephanny H. Briones Zambrano et al. evalúan los efectos de diferentes técnicas de control de malezas sobre el crecimiento temprano de *Schizolobium parahyba*, contribuyendo a prácticas forestales sostenibles y ofreciendo ideas útiles para la gestión agrícola y de recursos naturales.

En conjunto, estos seis artículos demuestran la naturaleza interdisciplinaria de la revista y su compromiso con el apoyo a investigaciones que conectan la innovación con aplicaciones del mundo real. Esperamos que este número sea de gran interés para investigadores y profesionales que trabajan en los diversos campos representados en *Enfoque UTE*.

Dr. Oscar Martínez Mozos
Universidad Politécnica de Madrid
Editor en Jefe

Dr. Diego Guffanti Martínez
Universidad UTE
Editor en Jefe

Dr. Wilson Pavón
Universidad UTE
Editor Ejecutivo

ENFOQUE UTE REVISTA
Facultad Ciencias de la Ingeniería e Industrias
RESEARCH ARTICLE
ENFOQUE UTE, VOL. 16, NO. 3, pp. 1-15, E-ISSN: 1390-6542
RECEIVED MARCH 21, 2025; ACCEPTED MAY 22, 2025; PUBLISHED ONLINE JULY 1, 2025;
DATA OF CURRENT VERSION JULY 1, 2025; PUBLISHED IN VOLUME 16, ISSUE 3 (JULY 2025).

Experimental Analysis of the Relationship between Flow Velocities and Sediment Transport in a Laboratory Channel Featuring a Lateral Bifurcation and Sand Bed

Darío Calderón[1], Khaled Hamad-Mohamed[2], Jorge Escobar-Ortiz[3*]

Abstract — **This experimental study investigates the relationship between flow velocities and sediment transport in a laboratory flume featuring a 90° lateral bifurcation with a mobile sediment bed composed of medium sand (D_{50} = 1.06 mm). The experiment was conducted at the Center for Research and Studies in Water Resources Engineering of the National Polytechnic School (CIERHI-EPN) using a scaled, fixed-geometry open-channel model under subcritical flow conditions with a constant discharge of 40 l/s. The objective is to establish empirical, experimentally validated correlations between flow structures and sediment dynamics in bifurcated channels. Instantaneous flow velocities were recorded at over 180 points using an Acoustic Doppler Velocimeter (ADV), and topographic measurements of the sediment bed were used to quantify scour and deposition. A total of 43.3 l of sand was scoured (with maximum depth of 15.01 cm), 8.0 l was redeposited (up to 8.49 cm thick), and 35.3 l was transported beyond the mobile bed. Results indicate that flow is predominantly one-dimensional in the upstream channel, while the bifurcation induces complex three-dimensional velocity components (Vx, Vy, Vz) associated with shear layers, vortex formation, and sediment redistribution. Compared to previous studies that focused on fixed beds or numerical simulations, this research provides high-resolution, experimental evidence of the link between secondary flow structures and sediment transport patterns under mobile-bed conditions. The findings contribute to improved predictive capabilities for morphodynamic behavior in natural bifurcations and support the development of more efficient sediment control and hydraulic design strategies.**

Keywords: **bifurcation, Acoustic Doppler Velocimeter (ADV), sediment transport, open-channel flow.**

* *Authors acknowledge the support provided by Escuela Politécnica Nacional. Corresponding author:*jorge.escobaro@epn.edu.ec

1. Darío Calderón Author is with the Centro de Investigaciones y Estudios de Ingeniería de los Recursos Hídricos & Departamento de Ingeniería Civil y Ambiental at Escuela Politécnica Nacional, Quito 170517, Ecuador. E-mail: dario.calderon@epn.edu.ec, ORCID number https://orcid.org/0000-0003-2171-5809
2. Khaled Hamad-Mohamed Author is with the Centro de Investigaciones y Estudios de Ingeniería de los Recursos Hídricos & Departamento de Ingeniería Civil y Ambiental at Escuela Politécnica Nacional, Quito 170517, Ecuador. E-mail: khaled.hamad@epn.edu.ec, ORCID number https://orcid.org/0000-0001-9365-9602
3. Jorge Escobar-Ortiz Author is with the Centro de Investigaciones y Estudios de Ingeniería de los Recursos Hídricos & Departamento de Ingeniería Civil y Ambiental at Escuela Politécnica Nacional, Quito 170517, Ecuador. E-mail: jorge.escobaro@epn.edu.ec, ORCID number https://orcid.org/0000-0003-3862-1657

DOI: https://doi.org/10.29019/enfoqueute.1150
Associate Editor: *Marcelo Mosquera*

Resumen — **Este estudio experimental investiga la relación entre las velocidades del flujo y el transporte de sedimentos en un canal de laboratorio con una bifurcación lateral de 90°, equipado con un lecho móvil compuesto por arena media (D_{50} = 1.06 mm). El experimento se realizó en el Centro de Investigaciones y Estudios en Ingeniería de los Recursos Hídricos de la Escuela Politécnica Nacional (CIERHI-EPN), utilizando un modelo físico de canal abierto con geometría fija, operado en condiciones de flujo subcrítico y con un caudal constante de 40 l/s. El objetivo es establecer correlaciones empíricas validadas experimentalmente entre las estructuras del flujo y la dinámica del sedimento en canales bifurcados. Se registraron velocidades instantáneas del flujo en más de 180 puntos mediante un velocímetro acústico Doppler (ADV), y se realizaron mediciones topográficas del lecho para cuantificar la socavación y la sedimentación. En total, se socavaron 43.3 l de arena (con una profundidad máxima de 15.01 cm), se redepositaron 8.0 l (con espesores de hasta 8.49 cm), y se transportaron 35.3 l más allá del lecho móvil. Los resultados indican que el flujo es predominantemente unidimensional en el canal de aproximación, mientras que la bifurcación induce componentes tridimensionales del flujo (Vx, Vy, Vz), asociados a capas de corte, formación de vórtices y redistribución de sedimentos. En comparación con estudios previos que se enfocan en lechos fijos o simulaciones numéricas, esta investigación aporta evidencia experimental de alta resolución sobre la relación entre estructuras de flujo secundario y patrones de transporte de sedimentos en condiciones de lecho móvil. Los hallazgos contribuyen a mejorar la capacidad predictiva del comportamiento morfodinámico en bifurcaciones naturales y respaldan el desarrollo de estrategias más eficientes para el control de sedimentos y el diseño hidráulico.**

Palabras Clave: **bifurcación, velocímetro acústico Doppler (ADV), transporte de sedimentos, flujo en canal abierto.**

I. INTRODUCTION

RIVER bifurcations, also known as diffluences, are critical geomorphological features where a single channel divides into two downstream branches, influencing flow partitioning, sediment transport, and channel stability. These junctions are fundamental in river deltas, alluvial fans, braided rivers, avulsions, anastomosing rivers, meanders or sinuous curves or bends in rivers, floodplains and meanders rectification and engineered waterway networks [1], where their stability dictates the long-term morphological evolution of riverine environments [2]. Mismanagement of sediment transport at bifurcations can lead to excessive deposition, erosion, or channel abandonment, which are crucial factors for hydraulic infrastructure design [3].

Among the key hydrodynamic processes governing bifurcated flows is the Bulle effect —a three-dimensional phenomenon in which near-bed, low-momentum flow and sediment are preferentially diverted into one branch of the bifurcation, often the lateral or secondary channel. This effect, driven by counter-rotating secondary vortices, causes an asymmetrical distribution of sediment load and contributes to scour in the main branch and deposition near the secondary channel entrance [4], [5]. As such, the Bulle effect introduces a nonlinear sediment partitioning mechanism that cannot be captured by depth-averaged models, highlighting the need for detailed experimental and three-dimensional analysis in bifurcation studies.

Despite their significance, bifurcations have historically received less attention compared to confluences. However, recent experimental, numerical, and field-based studies have refined our understanding of bifurcation dynamics. Laboratory experiments have demonstrated that bifurcation asymmetry —especially at large divergence angles— tends to promote channel abandonment through sediment plugging, reinforcing previous theories on the self-strangulation of secondary branches [6]. These studies, while insightful, have focused primarily on simplified configurations or idealized bifurcation angles under controlled conditions. In parallel, high-resolution numerical models have examined the influence of downstream boundary conditions and branch lengths on bifurcation stability [7].

However, such simulations are typically conducted under fixed-bed assumptions and symmetrical layouts, which limits their ability to replicate morphodynamic processes associated with mobile-bed conditions and sharp-angle bifurcations. The present study complements these efforts by experimentally investigating an asymmetrical bifurcation with a mobile sediment bed under controlled flow conditions, enabling direct observation of sediment dynamics and quantification of erosion–deposition patterns in geometries not fully addressed in prior work.

Numerical simulations have significantly contributed to understanding and predicting sediment partitioning at river bifurcations. For instance, [8] developed a one-dimensional morphodynamic model that incorporates erodible banks and local channel width adjustments. Their findings demonstrated that gravel-bed bifurcations naturally evolve toward asymmetric stable configurations, where one branch consistently captures most of the flow and sediment. Similarly, [9] implemented a field-validated framework for predicting water and sediment fluxes across delta bifurcations under varying discharge conditions. By integrating graph-based models and nodal relations derived from channel geometry and hydraulics, they achieved accurate partitioning estimates even in data-sparse environments. These studies underline the capacity of 1D and 3D models to reveal how sediment loads and planform variables control morphological evolution and long-term avulsion or stabilization patterns.

In contrast, simulations and field studies incorporating tidal influences highlight different stabilization mechanisms. [10] investigated two highly asymmetric, tide-affected bifurcations in the Kapuas River delta. Their findings revealed that neither transverse bed slopes nor inlet steps were sufficient to stabilize bifurcations dominated by suspended sediment transport. Instead, bed material sorting and the geometry of the side branches —particularly inlet width and depth— played critical roles in determining sediment division. These observations suggest that tidal dynamics may reduce branch dominance by dampening flow gradients, thus promoting morphological resilience in systems where fluvial and tidal forcings interact.

Field-scale research has reinforced the practical relevance of computational findings by validating them under real-world conditions. For example, [11] developed a quasi-two-dimensional model for braided gravel-bed rivers that revealed how small changes in the upstream Shields parameter can trigger shifts between symmetric and asymmetric bifurcation equilibria. However, their model assumes fixed banks and simplified loop geometries, limiting its applicability to natural systems with variable planform and mobile boundaries.

In a complementary approach, [12] implemented a physically-based moving boundary model to simulate sediment-laden inflows into lakes and reservoirs. Their results demonstrated how delta progradation and bottomset mud deposition are tightly coupled to turbidity current dynamics, but the scenarios assume stratified standing water and do not include fluvial bifurcation under open-channel flow. These examples illustrate how numerical modeling has advanced our understanding of bifurcation dynamics and deltaic evolution, while also highlighting the need for controlled experimental data to validate assumptions and extend their applicability to non-idealized channel systems.

Advances in bifurcation research have practical implications for river engineering and sediment management. Hydraulic interventions such as dredging and artificial bifurcation stabilization can trigger systemic morphological adjustments, including the formation of wedge-shaped sand plugs, channel abandonment, and significant redistribution of bed material across distributaries. [6] demonstrated experimentally that high diversion angles promote sediment deposition at the bifurcation's outer bank, leading to self-reinforcing sand plug growth and eventual disconnection of the diverted branch. Similarly, [10] showed that in tidally influenced bifurcations, interventions modifying the inlet geometry or flow distribution may alter the sediment-to-water division ratio. Such changes can destabilize the sediment balance and accelerate or inhibit branch siltation, depending on the interplay between bed material sorting, secondary flows, and tidal modulation. These findings underscore the necessity of adaptive sediment management strategies that integrate hydrodynamic and morphodynamic feedbacks to prevent unintended channel evolution and maintain long-term stability.

Emerging methodologies, such as high-resolution satellite imaging and computational fluid dynamics (CFD) simulations, are transforming bifurcation stability studies. Remote sensing techniques using Landsat imagery have facilitated long-term monitoring of bifurcation evolution, while advanced modeling platforms like Delft3D have provided new insights into the impacts of climate change and human interventions on bifurcation dynamics [7]. However, such numerical models have typically been applied under idealized conditions involving symmetrical geometries and fixed beds. As a result, they do not fully capture the morphodynamic complexity of acute-angle bifurcations with mobile sediment beds. The present experimental study addresses this gap by investigating, under controlled laboratory conditions, how flow redistribution affects sediment transport and local bed evolution in an asymmetrical bifurcation with a mobile granular bed.

However, despite these advances, a detailed understanding of how three-dimensional flow structures interact with sediment dynamics in sharp-angle lateral bifurcations under mobile bed conditions remains limited. Most existing studies either focus on fixed-bed scenarios, large-scale river systems with complex boundary conditions, or numerical predictions that require experimental validation. There is still a need for controlled laboratory experiments that can isolate the effects of velocity gradients, vortex shapes, and flow partitioning on localized scour and sediment deposition. Addressing this gap is crucial for improving sediment management strategies and informing the design of stable bifurcation systems.

This research aims to bridge existing knowledge gaps by conducting controlled laboratory experiments in a bifurcated channel with a mobile sediment bed. Using high-precision Acoustic Doppler Velocimetry (ADV), this study investigates the correlation between velocity distribution, sediment transport, and bifurcation stability. The experimental findings enable the identification of quantifiable relationships between hydrodynamic patterns and morphodynamic responses, offering a foundation for improving conceptual understanding and informing the calibration and validation of future numerical or field-based predictive models. These insights also support practical sediment management strategies in hydraulic engineering, with direct applications to river stabilization, flood mitigation, and waterway navigation management.

II. MATERIALS AND METHODS

A. Conceptual Framework, Experimental Design, and Benchmarking with Previous Studies

This study was initiated through a comprehensive review of the existing literature and the conceptual design of a physical modeling facility at the Center for Research and Studies in Water Resources Engineering (CIERHI) of the National Polytechnic School (EPN). The experimental platform was developed within a laboratory equipped with a closed-loop water recirculation system capable of delivering up to 100 l/s, constrained by pump power and head losses. The working area, approximately 200 m², was limited by the presence of adjacent experimental setups. In addition, a total of 800 kg (480 l) of non-cohesive sediment was available for experimental use.

These physical and operational constraints defined the configuration of the facility, including the geometry of the flume, slope selection, sediment retention and collection systems, and the positioning of the water intake and measurement units. The system incorporated complementary structures —such as dissipation tanks, sediment traps, scaffolding, and walkways— to ensure safe operation and facilitate accurate data acquisition. Preliminary hydraulic calculations were carried out to define the channel length, width, depth, and slope required to generate the desired sediment transport regime under subcritical conditions.

The sediment used consisted of uniform quartz sand with a median diameter D_{50} = 1.06 mm, selected for its well-documented behavior in experimental studies of sediment mobility and morphodynamics. This grain size falls within the range commonly employed in laboratory bifurcation studies [13] and ensures fully turbulent flow, bedload-dominated transport, and rapid morphological adjustment, enabling the identification of scour and deposition processes within practical timeframes. The uniformity of the material minimizes grain-size sorting effects and supports the reproducibility of bedforms, while avoiding cohesion or clustering that might interfere with sediment transport dynamics.

The geometric configuration of the experimental facility was established based on hydraulic design criteria and sediment transport considerations. The height of the mobile bed was defined through the estimation of local scour using five different analytical methods commonly applied in bridge foundation design [14]. Among these, the method proposed by [15] yielded the most critical depth (h = 0.32 m), and a conservative design thickness of h = 0.30 m was adopted for construction. The channel width was set to b = 0.60 m to allow high-resolution velocity profiling across five transverse sections spaced 10 cm apart using an Acoustic Doppler Velocimeter (ADV). The length of the approach channel (L = 4.0 m) was experimentally calibrated to ensure fully developed flow before the bifurcation, while the downstream main channel (L = 2.0 m) and the secondary branch (L = 0.94 m) were designed to accommodate the sand bed, flow redistribution, and sediment transport beyond the bifurcation node.

The selected discharge of Q = 40 l/s and the normal flow depth above the bed (d_0 = 0.24 m) were determined iteratively to ensure that the dimensionless shear stress remained below the critical Shields parameter for incipient motion and that the resulting critical slope was lower than the channel slope (S = 0.1 %). The sidewall height (H = 0.60 m) was chosen to safely contain both the mobile bed and the constant water depth, maintaining a freeboard of 0.06 m. The resulting design velocity near the bifurcation junction was approximately U_0 = 0.28 m/s.

The experimental sediment consisted of non-cohesive quartz sand with a median grain size D_{50} = 1.06 mm, selected for its proven suitability in morphodynamic flume studies. Previous experiments on mobile-bed bifurcations have employed similar particle sizes ranging from 0.5 mm to 1.1 mm [13], [16], [17], which ensure bedload-dominated transport under turbulent conditions and allow for rapid morphological response without cohesive interference. Furthermore, the adopted geometric parameters—including a 0.30 m sand thickness, 0.60 m flume width, and 4.0 m approach length—align with established experimental configurations in the literature and are consistent with validated setups for bifurcation flow-sediment interaction studies.

Previous research has demonstrated the effectiveness of physical models in analyzing sediment–flow interactions at bifurcations. [18] studied sediment transport in 90° diversions, confirming the importance of controlled laboratory conditions. However, this study was based on a fixed-bed experimental setup with relatively short test durations (45-75 minutes), which limited the observation of long-term morphological evolution and bed feedback processes. [6] showed that bifurcation angles significantly influence sediment deposition and channel evolution, underscoring the need for precise geometric control in physical experiments. Nevertheless, these experiments were focused on idealized geometries and did not address configurations with sharp angles and fully mobile sediment beds, nor did they quantify the uncertainty associated with measured flow velocities.

To address these limitations, the present study introduces a mobile-bed laboratory setup with over 180 high-resolution velocity measurements, using the SonTek FlowTracker2 ADV. The instrument provides velocity accuracy within 1 % of the measured value per second, with uncertainty analysis grounded in Interpolated Variance Estimator (IVE) and ISO-748 methods [19]. Moreover, quality control is ensured through parameters such as Signal-to-Noise Ratio (SNR ≥ 10 dB) and velocity standard error (< 0.01 m/s), as specified in the manufacturer's guidelines [20], [21]. This methodology enhances the reliability of the experimental data and addresses gaps in precision and representativeness noted in earlier studies.

B. Experimental Flume Configuration and Hydraulic Setup

Based on the hydraulic and sediment transport design considerations, the physical modeling facility was constructed at the Center for Research and Studies in Water Resources Engineering (CIERHI), located in Quito, Ecuador. The experimental flume consists of a prismatic, transparent acrylic channel measuring 4.0 m in length, 0.60 m in width and height, with a longitudinal slope of 0.1 %. Transparent acrylic walls were selected due to their smoothness and high optical clarity, which are ideal for flow visualization and accurate ADV measurements in laboratory conditions. A 90° lateral bifurcation branches off the main channel into a secondary arm measuring 2.0 m in length, with identical cross-sectional dimensions and slope.

The bifurcation zone was designed to simulate natural sediment–flow interactions and includes a mobile sediment bed with a uniform thickness of 0.30 m, extending 1.70 m along the main channel and 0.93 m along the secondary branch. The bed was filled with well-sorted quartz sand characterized by a median grain size D_{50} = 1.06 mm, with D_{16} = 0.85 mm, D_{84} = 1.40 mm, a specific weight of 1660 kg/m³, a uniformity coefficient C_u = 1.49, and a curvature coefficient C_c = 1.03.

To realistically represent fluvial bifurcations under controlled laboratory conditions, the channel geometry was deliberately configured with a sharp divergence angle (~90°) and uniform rectangular cross-sections in both branches. This planform asymmetry is frequently encountered in natural systems such as deltas and distributary networks, where it promotes the development of flow separation zones, secondary vortices, and sediment plug formation. The flat bed and constant slope further enable precise control over sediment mobilization and redistribution. This configuration allows for the reproduction and monitoring of key morphodynamic processes —such as branch flow redistribution, vortex-driven transport, and localized scour— that are essential to the stability and evolution of natural and engineered bifurcations.

Flow control at the downstream end of the secondary channel is achieved using a vertically adjustable gate positioned 0.132 m from the channel top (0.468 m from the bottom), regulating flow to maintain a water depth of 0.24 m above the sand bed. The calculated recirculating flow rate was 40 l/s. Fig. 1A) shows the perspective view of the setup, while Fig. 1. B) details the sand bed and its key dimensions.

C. Preliminary Calibration and Bed Adjustment for Equilibrium Conditions

Preliminary testing involved verifying watertightness, expected flow patterns, and initial sediment behavior. It was found that the original geometry of the bed did not allow an adequate development of sediment transport phenomena, especially in the secondary channel, whose short length prevented the sedimentation of sand in the area downstream of the main mound that was being formed. Therefore, the distribution of the sand bed was adjusted with the purpose of locating it in the areas of greatest occurrence of sediment transport phenomena, shortening its length in the main channel by 0.30 m and extending it in the secondary channel by 0.30 m, but maintaining its width and height, resulting in the final configuration shown in Fig. 1. B).

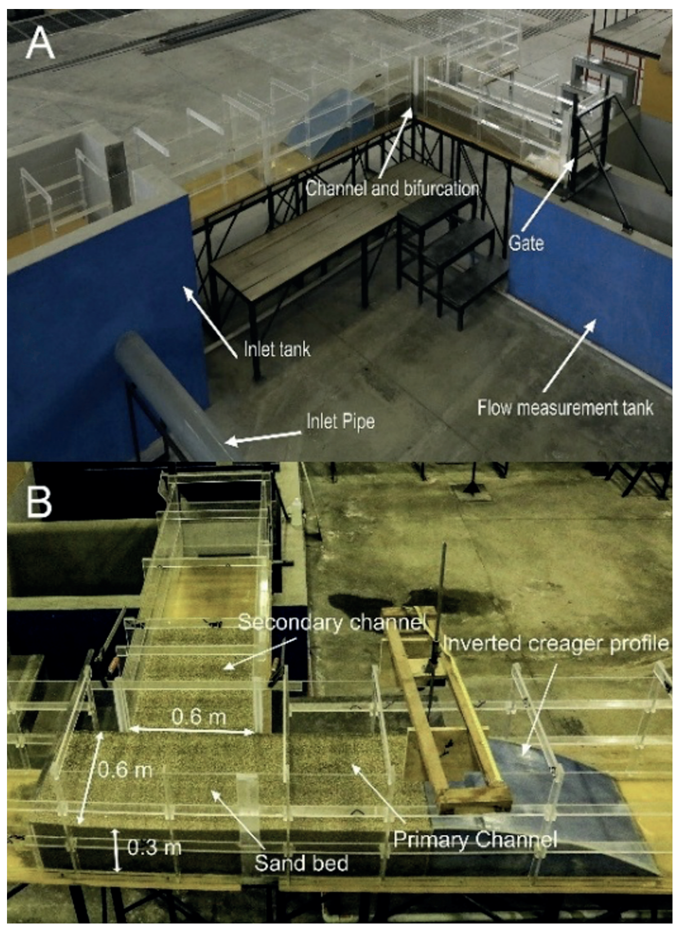

Fig. 1. Experimental facilitie A) Perspective view. B) Sand bed and its main dimensions.

Boundary conditions were defined to remain constant throughout testing (flow rate Q = 40 l/s, water depth d_0 = 0.24 m, channel width b = 0.60 m and channel slope S = 0.1 %), the average velocity calculated for the main approach channel is U_0 = 0.28 m/s, while flow velocities and sediment transport varied spatially in the area of the bifurcation, which will be further detailed below. A flow rate of 40 l/s was maintained continuously for 24 hours until a relative equilibrium between scour and deposition was reached, the criterion used to determine bed equilibrium is the absence of movement in the sediments while the water is still flowing [22] It should be emphasized that the subsequent velocity measurement was performed only after equilibrium had been reached in the sediment transport, i.e. when no more spatial variations of the bed were recorded, so that the movement of the sand particles would not affect the validity of the velocities obtained.

D. Bathymetric Survey of the Mobile Bed and Resolution Constraints

The topographic survey of the sand bed (bathymetry) was carried out at the bifurcation of the experimental facility. For this purpose, mobile limnimeters were used following a matrix or grid drawn every 3 cm in the X and Y directions. For both channels there are limitations on bed edge measurements, it was not possible to topographically survey the edges of the sand bed with a thickness between 1.0 and 4.5 cm due to the physical impossibility of lowering the limnimeters in these areas located next to the acrylic pieces that compose the main and secondary channels. Details of their dimensions and location are shown in Fig. 2, where the cross and normal sections at whose intersections the flow velocities were measured are also shown, as explained in the following section.

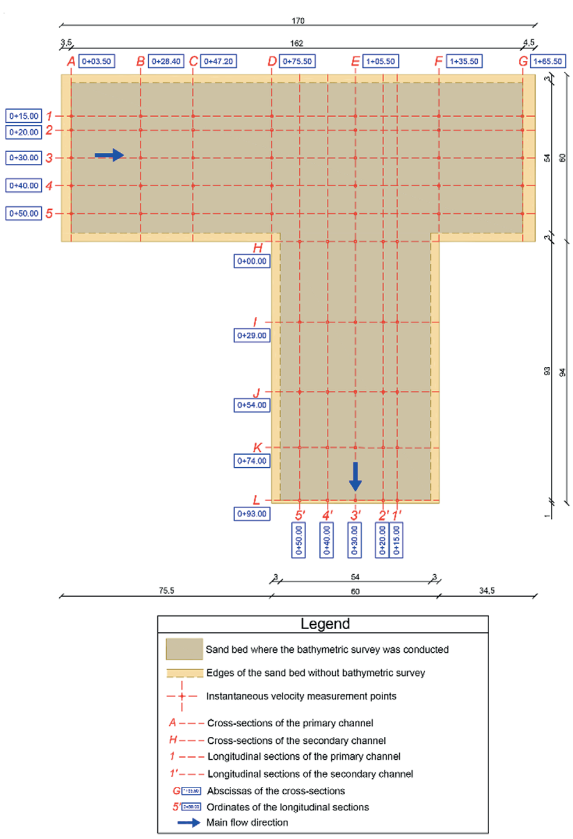

Fig. 2. Dimensions and location of the surveyed sand bed and remaining edges.

The sediment used in this study —uniform quartz sand with a median grain size of approximately 1.06 mm— is typically transported as bedload, primarily through rolling and saltation under subcritical flow conditions. Due to its relatively high settling velocity, this particle size exhibits limited suspension unless subjected to intense turbulence or near-flood conditions. The dominance of near-bed transport in such granulometric ranges justifies the use of fine-resolution bathymetric grids (3 cm × 3 cm), as most morphological changes —such as scour and deposition— occur close to the sediment–flow interface and within short spatial scales [23], [24].

Moreover, the well-sorted nature of the sediment (with a uniformity coefficient C_u = 1.49) facilitates coherent bedform development and predictable mobilization once the Shields threshold is exceeded. In contrast to poorly sorted mixtures, uniform sediments promote synchronized particle entrainment and well-defined morphological structures such as ripples or dunes, enhancing the reproducibility and interpretability of bathymetric measurements [25], [26]. Thus, both the granulometry and the high-resolution survey strategy contribute to the robustness of the morphological data collected in this flume experiment.

E. Three-Dimensional Velocity Measurement and Experimental Flow Characterization

Flow directions were defined with X as the longitudinal axis, Y as transverse, and Z as vertical (Fig. 3), allowing systematic assessment of velocity components within both channels.

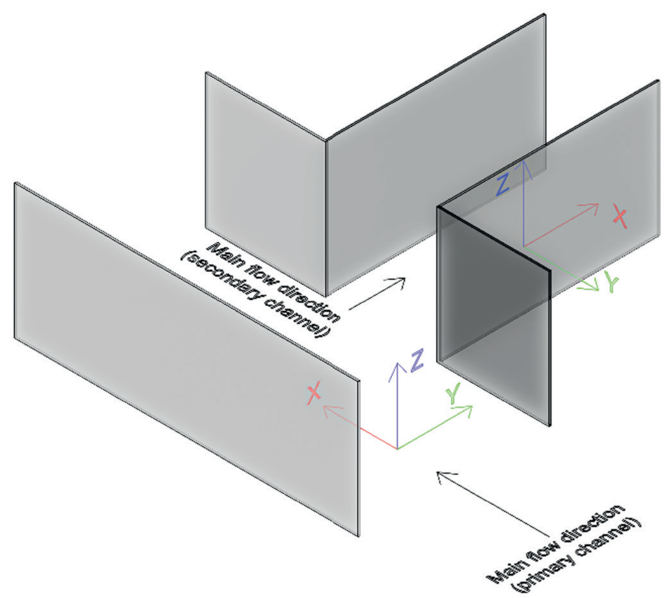

Fig. 3. Schematic of the spatial directions or components (X, Y, Z) adopted for the flow in the primary and secondary channels.

Instantaneous flow velocities were taken at more than 180 points, defined by the intersection between cross sections (YZ planes), normal (XZ planes) and longitudinal (XY planes); distributed as follows:

- By varying the abscissae X, 7 cross sections were chosen for the main channel (A, B, C, D, E, F and G) and

5 cross sections for the secondary channel (H, I, J, K and L); these were defined according to the physical space available for the location of the ADV and its support on the channels.

- By varying the Y ordinates, 5 normal sections were chosen for the main channel (1, 2, 3, 4 and 5) and 5 normal sections for the secondary channel (1', 2', 3', 4' and 5'); these were defined according to the lateral distance that the equipment must have from the solid objects for optimum performance.
- Varying the Z dimensions, 3 longitudinal sections were chosen for both channels (α, β and γ); these were defined according to the minimum submergence and the vertical distance that the equipment must have from solid objects for optimum performance.

The distribution of the velocity measurement points is shown in the Fig. 4, Fig. 5, Fig. 6 and Fig. 7. These locations enabled a comprehensive spatial characterization of velocity fields [27] demonstrated the efficacy of ADV technology in capturing secondary flows relevant to sediment transport. [10] further validated the precision of ADV measurements in asymmetric bifurcation setups.

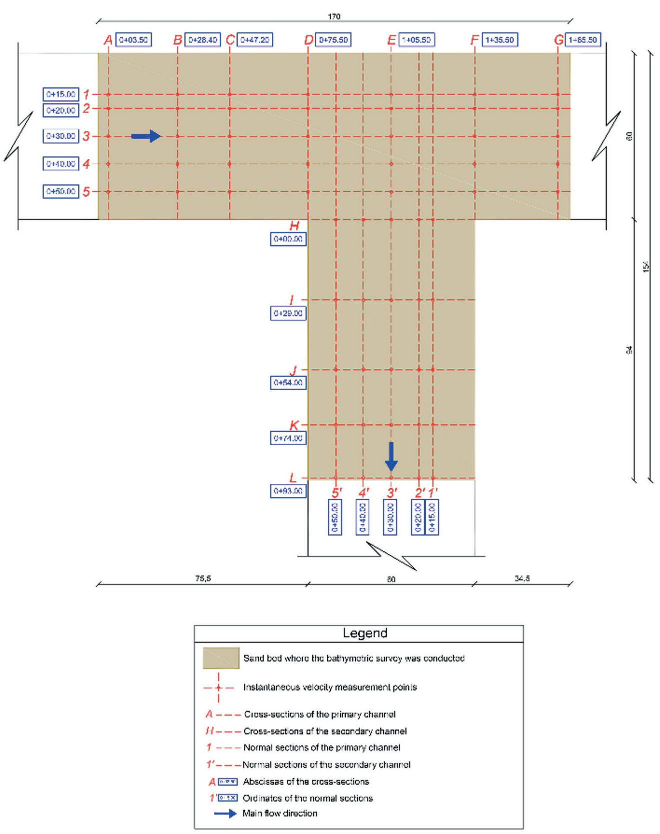

Fig. 4. Plan view diagram showing the position of the points and sections where instantaneous flow velocity measurements were taken.

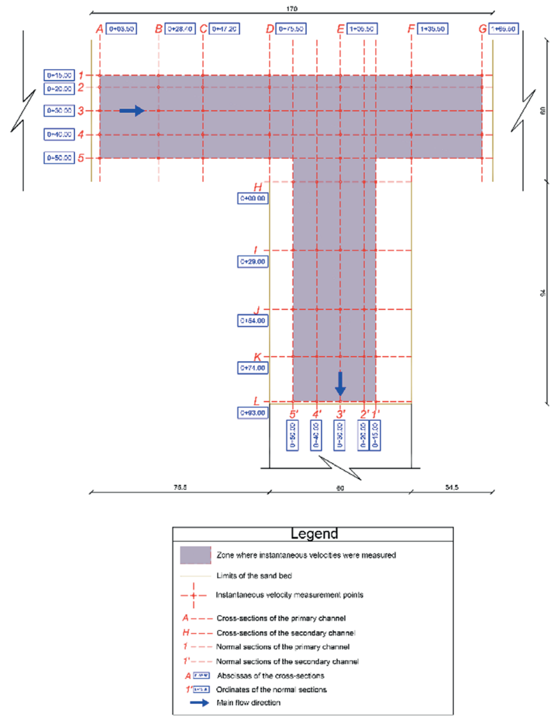

Fig. 5. Plan view diagram showing the position of the points, sections, and area where instantaneous flow velocity measurements were taken.

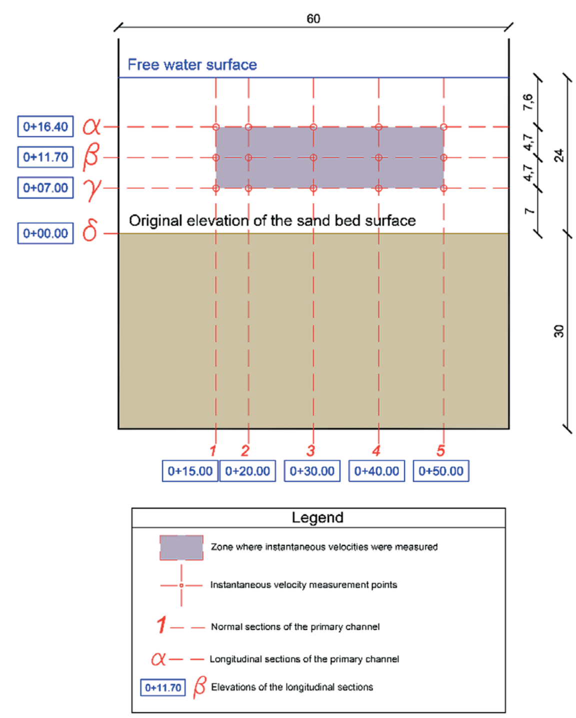

Fig. 6. Section view diagram showing the position of the points, sections, and area where instantaneous flow velocity measurements were taken in the primary channel.

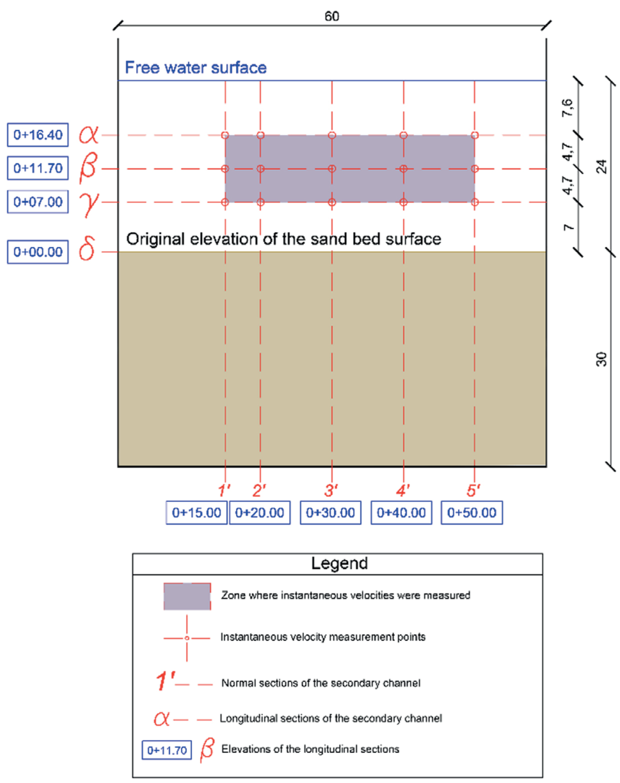

Fig. 7. Section view diagram showing the position of the points, sections, and area where instantaneous flow velocity measurements were taken in the secondary channel.

For measuring instantaneous flow velocities, an Acoustic Doppler Velocimeter (ADV) was used, specifically the SonTek FlowTracker2, a high-technology instrument designed for three-dimensional velocity data acquisition in shallow flows [28]. Measurements were taken at over 180 locations within the bifurcation zone. At each point, velocity data were recorded for a total duration of 40 seconds, with a data output interval of 0.5 seconds, yielding 80 instantaneous velocity readings per point. The sampling rate, data filtering, and averaging were managed via the manufacturer's software suite.

The ADV probe includes a central transmitter and three acoustic receivers. To ensure data quality, care was taken to position the sampling volume at least 5 cm away from solid boundaries and above the active layer of the mobile sediment bed, avoiding signal reflection or acoustic interference. According to the manufacturer, the Signal-to-Noise Ratio (SNR) must remain between 10 and 50 dB to ensure reliable velocity measurements, and the standard deviation of the horizontal components should remain below 0.01 m/s [20] These thresholds were verified in real time during acquisition.

Although ADVs provide high-resolution data, they can be affected by sediment suspension, signal scattering near the bed, and low flow turbulence near walls. In this study, potential disturbances were mitigated by positioning the probe well within the flow core and rejecting outlier values based on velocity standard deviation and SNR thresholds. Similar protocols have been employed in previous laboratory studies of sediment transport in bifurcations [5], [29], where ADV performance has proven adequate under controlled conditions with mobile beds.

Studies such as those by [30] have employed similar measurement techniques to analyze velocity distribution and sediment transport in bifurcated channels, confirming the effectiveness of these methods in obtaining precise and detailed hydrodynamic data in physical models. Once the optimal conditions for proper device operation were verified, instantaneous velocities were recorded at the previously specified points as part of the experimental trials to quantitatively characterize the main hydrodynamic phenomena occurring within the setup.

To ensure that the flow conditions are representative of natural bifurcations, the experimental design was guided by dimensionless parameters commonly used in fluvial hydraulics, including Froude number, aspect ratio, and bifurcation angle. The selected slope (0.1 %), sediment size ($D_{50} \approx 1.06$ mm), and flow rates were calibrated to promote sediment mobility under turbulent flow while reproducing features such as vortex formation, flow separation, and localized scour —characteristic of bifurcating river systems. These emergent phenomena have been reported in both field and laboratory studies [5], [6], confirming the morphological and hydrodynamic similarity between the experimental setup and natural conditions.

These methodological choices align with best practices in sediment transport research and contribute to the broader understanding of hydrodynamic processes governing bifurcation stability and sediment partitioning.

III. RESULTS AND DISCUSSION

The magnitudes of the resultant velocity vectors for the mean velocities Vx, Vy, and Vz of the circulating flow over the sand bed in the experimental setup are graphically represented for the three longitudinal sections α, β, and γ. Analysis of the spatial velocity field in the three longitudinal sections (α, β, and γ) provides essential data on the changes in hydrodynamic flow conditions leading to scour and sediment deposition in the bifurcation zone. Studies such as [2] and [30] confirm that the interaction between velocity fields and sediment motion is crucial in bifurcations, influencing both scouring and deposition processes.

Recent numerical studies, such as those by [8], have validated experimental observations by simulating velocity distributions and sediment behavior in bifurcations. These models confirm the existence of secondary circulations and velocity gradients that govern sediment transport, reinforcing the experimental findings of this study (Table I).

A. Velocity Variability in Longitudinal Sections

The graphical representation of resultant velocity vectors for mean velocities Vx, Vy, and Vz (calculated from the average instantaneous velocities) allows for the identification of flow acceleration, deceleration, and vortex formation in each longitudinal section, which are essential in understanding sediment transport mechanisms. The spatial distribution of velocity magnitudes along the longitudinal sections reveals significant changes in flow characteristics induced by the bifurcation. The graphical representation of resultant velocity vectors—computed from the mean components Vx, Vy, and Vz obtained from time-averaged instantaneous data—facilitates the identification of flow acceleration, deceleration, and vortex formation. These phenomena are essential to understanding sediment transport mechanisms within the bifurcation zone.

Numerical simulations by [8] predicted counter-rotating vortices forming before the bifurcation apex, a phenomenon that was also observed experimentally by [27] and [31]. These vortices influence near-bed sediment transport, leading to uneven sediment distribution between the branches.

1. Longitudinal Section α

Fig. 8. illustrates the velocity distribution for longitudinal section α, located at a height of 0.164 m from the original sand bed level.

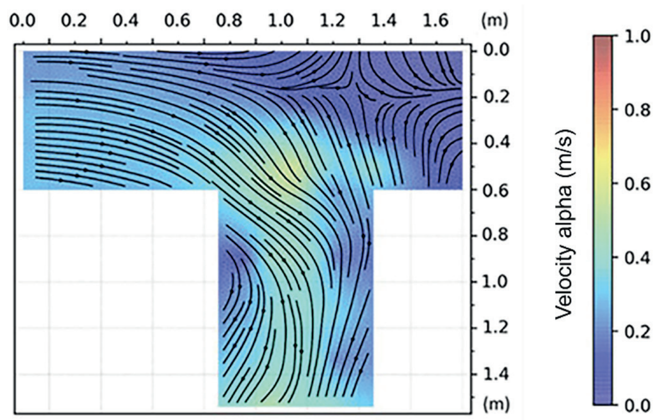

Fig. 8. Magnitudes of the resultant velocity vectors V for the mean velocities Vx, Vy, and Vz in longitudinal section α at a height of 0.164 m.

Analysis for the Primary Channel

In the primary channel, a progressive reduction in the Vx component is observed from Section A to Section F, while the Vy component increases near the bifurcation zone. This trend aligns with findings from [27], who observed similar velocity redistribution patterns in experimental bifurcations, emphasizing their crucial role in sediment transport.

The Vx velocity component exhibits values around 0.28 m/s at abscissa 0.035 m (Section A), progressively decreasing until reaching 0.00 m/s or slightly negative values at abscissa 1.655 m (Section G). The lowest Vx values for this channel are observed near the left boundary.

The Vy velocity component exhibits values around 0.00 m/s at abscissa 0.035 m (Section A), progressively increasing until reaching 0.52 m/s at abscissa 1.055 m (Section E) located at the center of the lateral bifurcation. The lowest Vy values are observed near the left boundary of the channel.

In the dead volume zone at the end of the primary channel extension, between abscissas 1.355 m (Section F) and 1.655 m (Section G), counterclockwise vertical-axis vortices form due to flow division, confirmed by the presence of both positive and negative velocity values at abscissas 1.355 m and 1.655 m. These vortices contribute to localized energy dissipation on 90° lateral diversions [31], similar to the observations made by [2] in their studies on bifurcation-induced transport mechanisms.

TABLE I
SUMMARY OF INSTANTANEOUS VELOCITY EXTREMES AND RESULTANTS

LONGITUDINAL SECTION α								
Main Channel								
	Normal Velocity Vx				**Transverse Velocity Vy**		**Resultant Velocity V**	
	Maximum		**Minimum**		**Maximum**	**Minimum**	**Maximum**	**Minimum**
Value (m/s)	0.29		0		0.52	0	0.56	0
Cross Section (Abscissa m)	A (0.035)	A (0.035)	G (1.655)	F (1.355)	E (1.055)	G (1.655)	E (1.055)	G (1.655)
Normal Section (Ordinate m)	3 (0.30)	5 (0.50)	1 (0.05)	2 (0.20)	5 (0.50)	1 (0.15)	5 (0.50)	1 (0.15)
Secondary Channel								
	Normal Velocity Vx				**Transverse Velocity Vy**		**Resultant Velocity V**	
	Maximum		**Minimum**		**Maximum**	**Minimum**	**Maximum**	**Minimum**
Value (m/s)	0.39		0.09		-0.44	0	0.52	0.11
Cross Section (Abscissa m)	L (0.930)		I (0.290)		H (0.000)	K (0.740)	H (0.000)	I (0.290)

	Normal Velocity Vx				Transverse Velocity Vy		Resultant Velocity V	
	Maximum		Minimum		Maximum	Minimum	Maximum	Minimum
Normal Section (Ordinate m)	2’ (0.20)		5’ (0.50)		3’ (0.30)	3’ (0.30)	3’ (0.30)	5’ (0.50)
LONGITUDINAL SECTION β								
Main Channel								
	Normal Velocity Vx				**Transverse Velocity Vy**		**Resultant Velocity V**	
	Maximum		**Minimum**		**Maximum**	**Minimum**	**Maximum**	**Minimum**
Value (m/s)	0.29		0		0.49	0.01	0.53	0.03
Cross Section (Abscissa m)	A (0.035)	A (0.035)	F (1.355)		E (1.055)	G (1.655)	E (1.055)	G (1.655)
Normal Section (Ordinate m)	3 (0.30)	5 (0.50)	4 (0.40)		5 (0.50)	1 (0.15)	5 (0.50)	1 (0.15)
Secondary Channel								
	Normal Velocity Vx				**Transverse Velocity Vy**		**Resultant Velocity V**	
	Maximum		**Minimum**		**Maximum**	**Minimum**	**Maximum**	**Minimum**
Value (m/s)	0.4		0.18		-0.37	0.01	0.48	0.18
Cross Section (Abscissa m)	L (0.930)		I (0.290)		H (0.000)	J (0.540)	I (0.290)	I (0.290)
Normal Section (Ordinate m)	1’ (0.15)		5’ (0.50)	1’ (0.15)	3’ (0.30)	1’ (0.15)	3’ (0.30)	5’ (0.50)

LONGITUDINAL SECTION γ						
Main Channel						
	Normal Velocity Vx		**Transverse Velocity Vy**		**Resultant Velocity V**	
	Maximum	**Minimum**	**Maximum**	**Minimum**	**Maximum**	**Minimum**
Value (m/s)	0.3	0.01	0.48	0	0.53	0.02
Cross Section (Abscissa m)	A (0.035)	G (1.555)	E (1.055)	B (0.284)	E (1.055)	G (1.655)
LONGITUDINAL SECTION γ						
Main Channel						
Normal Section (Ordinate m)	5 (0.50)	5 (0.50)	5 (0.50)	12 (0.20)	5 (0.50)	1 (0.15)
Secondary Channel						
	Normal Velocity Vx		**Transverse Velocity Vy**		**Resultant Velocity V**	
	Maximum	**Minimum**	**Maximum**	**Minimum**	**Maximum**	**Minimum**
Value (m/s)	0.38	0.2	0.53	-0.01	0.63	0.21
Cross Section (Abscissa m)	J (0.540)	H (0.000)	L (0.930)	J (0.540)	L (0.930)	H (0.000)
Normal Section (Ordinate m)	4’ (0.40)	1’ (0.15)	5’ (0.50)	1’ (0.15)	5’ (0.50)	1’ (0.15)

Analysis for the Secondary Channel

In the secondary channel, a progressive increase in the Vx component is observed from Section H to Section L, while the Vy component is higher near the bifurcation zone.

The Vx velocity component exhibits values around 0.21- 0.26 m/s at abscissa 0.000 m (Section H), progressively increasing until reaching 0.32 – 0.39 m/s at abscissa 0.930 m (Section L); this trend indicates flow stabilization downstream, as the absence of additional geometric disturbances allows the flow to regain its uniform characteristics; however, variability is observed near the channel boundaries, particularly at ordinates 0.15 m (Section 1') and 0.50 m (Section 5'), with fluctuations evident at abscissas 0.29 m (Section I), 0.54 m (Section J), and 0.74 m (Section K). The lowest Vx values for this channel are observed near the right boundary.

The Vy velocity component exhibits values from 0.44 to 0.09 m/s at abscissa 0.000 m (Section H) and from 0.07 to 0.37 m/s at abscissa 0.930 m (Section L), show no clear trend. [10] A large vertical axis vortex with clockwise rotation, elongated and oval section, is identified along the X-axis; this vortex with low velocities is located on the right side of the secondary channel, in the area approximately between the intersection points of sections H and 5', H and 3', L and 5', and L and 3'. Similar vortex formations have been reported by [10], besides, studies by [6] demonstrated that vortex-induced flow changes can enhance sediment accumulation along the inner bank of a bifurcated branch, just like the results of this study.

In summary, in section α, positioned 0.164 m above the original sand bed level, Vx velocity components tend to decrease at the end of the primary channel and accelerate along the secondary channel, particularly at its central ordinates. Meanwhile, Vy velocity components show higher values in the bifurcation zone of both channels, reinforcing the velocity redistribution effect of the bifurcation.

2. Longitudinal Section β

Fig. 9. illustrates the velocity distribution for longitudinal section β, located at a height of 0.117 m from the original sand bed level.

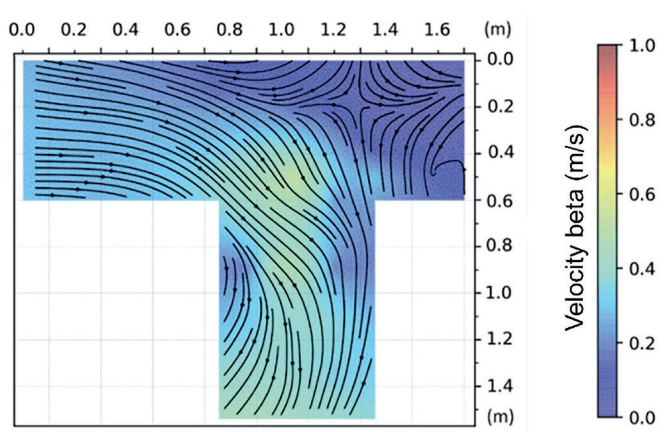

Fig. 9. Magnitudes of the resultant velocity vectors V for the mean velocities Vx, Vy, and Vz in longitudinal section β at a height of 0.117 m.

Analysis for the Primary Channel

In longitudinal section β, located 4.7 cm below section α, the resultant velocity vectors V and their Vx and Vy components exhibit similar values, flow patterns and trends as those observed in section α; however, a notable difference is observed: in section β, the area occupied by vorticity zones (regions of low positive and negative velocities) is larger in the plan view, particularly at the downstream end and along the left side of the primary channel.

The increase in the vorticity region at greater depths suggests an intensification of turbulence, which aligns with the experimental observations of [30], where turbulence intensity was found to increase with depth in bifurcated flow conditions. This behavior is crucial in sediment transport dynamics, as reported by [27], who demonstrated that secondary flow patterns at deeper layers influence the redistribution of sediment within bifurcation zones.

Analysis for the Secondary Channel

As in the primary channel, in longitudinal section β, similar flow patterns and velocity trends and variations are maintained; however, a notable difference is observed: the plan-view area occupied by the low-velocity zone, which is the section of a vortex on the right side of the secondary channel, is slightly reduced. Similarly, the low-velocity area on the left side of the channel is smaller, indicating that flow velocities Vx, Vy and vectors V are slightly higher at this elevation; it suggests more active sediment transport.

In summary, in section β, positioned 0.117 m above the original sand bed level, the same velocity trends observed in section α are maintained, but with slightly higher velocities near the edges of both channels, except in the dead zone of the primary channel.

3. Longitudinal Section γ

Fig. 10 illustrates the velocity distribution for longitudinal section γ, located at a height of 0.070 m from the original sand bed level.

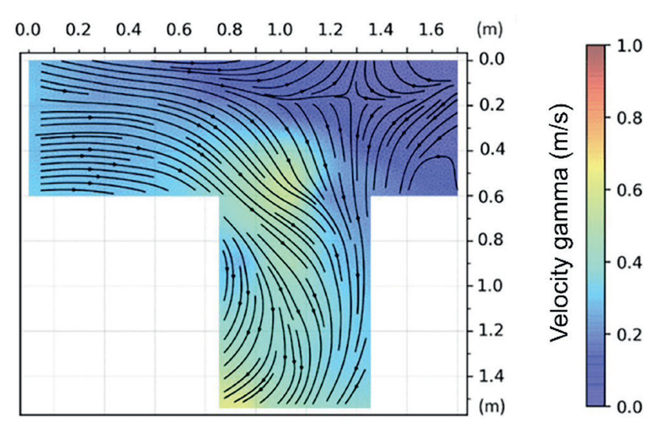

Fig. 10. Magnitudes of the resultant velocity vectors V for the mean velocities Vx, Vy, and Vz in longitudinal section γ at a height of 0.070 m.

Analysis for the Primary Channel

In longitudinal section γ, located 4.7 cm below section β, the resultant velocity vectors V and their Vx and Vy components exhibit similar values, flow patterns and trends as those observed in section β; however, a notable difference is observed: in section γ, the area occupied by vorticity zones (regions of low positive and negative velocities) is larger in the plan view, particularly at the vicinity of the intersection between Sections F and 5. In addition, the area of high speeds was increased at the vicinity of the intersection between Sections E and 5, being evidence of increased vorticity and turbulence in the center of the bifurcation.

Analysis for the Secondary Channel

As in the primary channel, in longitudinal section γ, similar flow patterns and velocity trends and variations are maintained; however, a notable difference is observed: the low velocity zone corresponding to the lower section of the vertical axis vortex in the right center of the channel, has an even smaller area than in section β, which is indicative of its conical and inclined shape, i.e., its diameter is smaller as the flow deepens and always remains next to the channel wall. No velocity measurements were recorded exactly in the center of the vortex in the section γ, due to significant sediment deposition in these areas, which prevents the ADV from being positioned, given the manufacturer's minimum distancing recommendations. The values plotted for this zone in Fig. 10. are interpolations of the data around it, therefore sedimentation does not affect the validity of the data. In addition, significant increases in velocities Vx, Vy and V are recorded, especially in sections L and the right zone of section K.

In summary, in section γ, positioned 0.070 m above the original sand bed level, the same velocity trends observed in section α and β are maintained, but with higher velocities near the edges of both channels, except in the dead zone of the primary channel. There is a vertical axis vortex in the right center of the secondary channel, it's conical and has an inclined shape.

B. Analysis of Sediment Transport Phenomena

Fig. 11 and 12 qualitatively illustrate the sand bed formations after reaching a relative equilibrium in sediment transport within the experimental setup. These formations result in scour in some areas and sediment deposition in others, affecting both channels of the experimental installation.

Fig. 13 provides a quantitative representation of sediment transport phenomena (scour and sedimentation) through a three-dimensional depiction and topographic contour lines, where the 0.00 m level represents the original elevation of the sand bed before water flow circulation began.

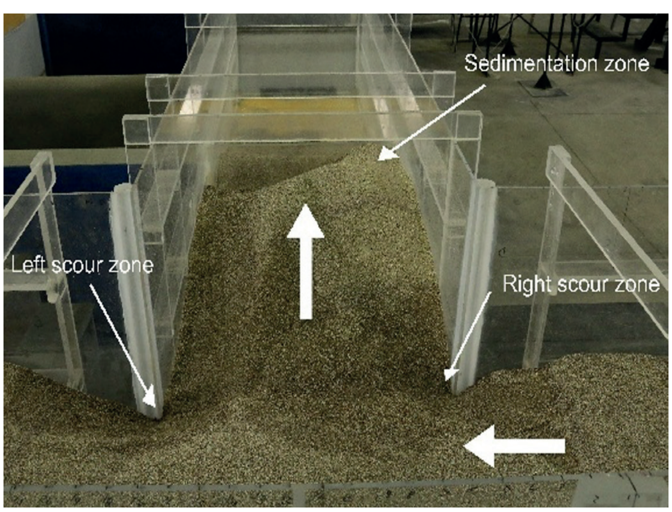

Fig. 11. Lateral perspective view of the scour and sedimentation zones in the sand bed of the experimental setup.

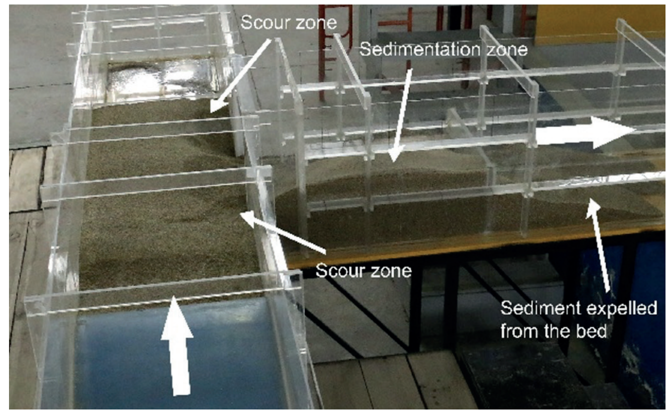

Fig. 12. Frontal perspective view of the scour and sedimentation zones in the sand bed of the experimental setup.

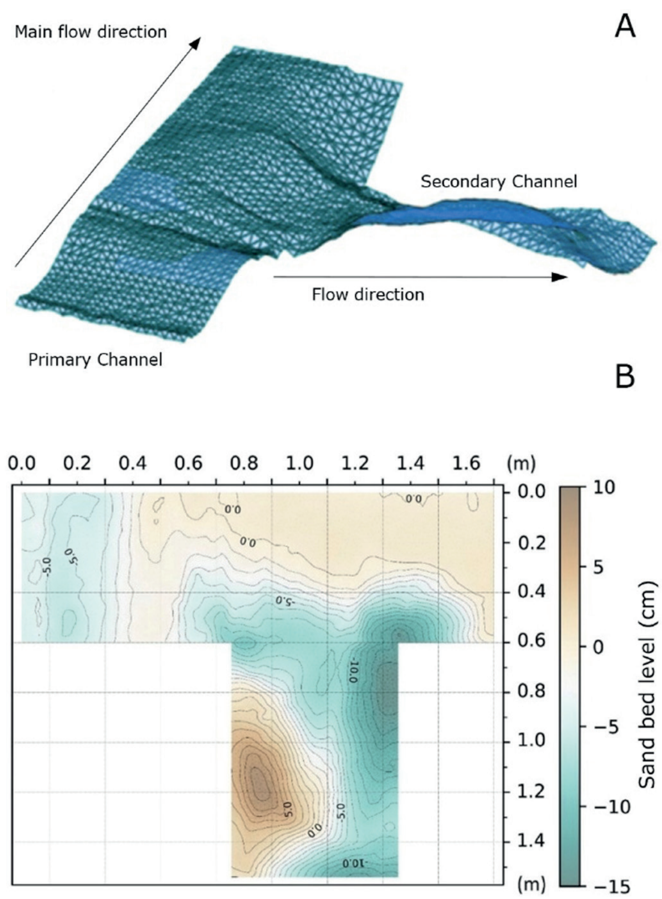

Fig. 13. A) Three-dimensional representation of the sand bed in the bifurcation zone after reaching a relative equilibrium in sediment transport. B) Topographic contour lines of the sand bed.

Sediment transport in the experimental setup is predominantly concentrated in the bifurcation zone, particularly along the edges connecting the two channels, specifically at the intersection of Sections D and F with Section H. The primary channel exhibits only scour processes, whereas the secondary channel experiences both scour and sedimentation phenomena.

In the primary channel, sediment transport is concentrated in Sections 4 and 5 (right zone) near the bifurcation. Conversely, in Sections 1 and 2 (left zone) and further downstream of Section 3 (central zone), the sand bed remains largely undisturbed. Unrelated scour phenomena are observed in Sections A and B, occurring due to the transition from a solid, fixed bed with an inverted Creager profile to a mobile, erodible sediment bed at the entrance of the primary channel. These localized scour effects are unrelated to the bifurcation and are therefore excluded from further analysis. At abscissa 0.472 m (Section C), the original bed level is maintained, as the influence of the bifurcation on flow and sediment dynamics is still minimal in this region.

From abscissa 0.500 m onward, intense scour phenomena develop in the right and central regions of the primary channel, progressively increasing toward edge DH at abscissa 0.755 m, where a maximum scour depth of 8.71 cm is recorded. The scour extends in both X and Y directions within the secondary channel, forming an irregular pattern in the plan view.

At abscissa 1200 m, a more intense scour phenomenon occurs, increasing towards edge FH at abscissa 1355 m, where a maximum scour depth of 14.41 cm is reached. Similar to the previous case, this scour is concentrated around the edge, forming a distinct oval shape in the plan view, with its major axis oriented toward the secondary channel and its minor axis toward the primary channel. Beyond abscissa 1.700 m, the sediment level remains relatively undisturbed.

In the secondary channel, sediment transport affects the entire sand bed surface, with both scour and sedimentation phenomena present. These two processes are separated by the 0.0 m topographic contour line, as shown in Fig. 13B).

- In Sections 1' and 2' (left zone), only scour is observed.
- In Sections 3', 4', and 5' (center and right zone), both scour and sedimentation occur.

The most intense scour in the experimental setup is recorded at abscissa 0.000 m in the secondary channel, resulting from a combined effect of flow redirection at edges FH and DH.

- A maximum scour depth of 9.91 cm is recorded to the right at abscissa 0.000 m, ordinate 0.57 m.
- A maximum scour depth of 15.01 cm is recorded to the left at abscissa 0.120 m, ordinate 0.03 m.

These scour zones are the deepest observed within the experimental setup.

- The scour associated with edge DH extends approximately to abscissa 0.180 m (between axes H and I).
- The scour associated with edge FH extends approximately to abscissa 0.740 m (axis K).

At abscissa 0.180 m, at the far-right edge of the channel, the 0.0 m topographic contour line begins, enclosing the sediment deposition volume on the right side of the secondary channel, extending downstream to its final section at abscissa 0.930 m.

- To the left of the 0.0 m level, the entire scoured zone of the secondary channel is located, covering most of its surface in the plan view.

The oval and concentric pattern of the sediment deposition contours indicates that flow conditions favor sediment transport from the eroded bifurcation zone and its deposition downstream to the right. The sedimentation rate increases toward the centroid of the deposited volume, located at abscissa 0.540 m, ordinate 0.51 m, reaching a maximum height of 8.49 cm. Sedimentation extends downstream up to abscissa 0.930 m (Section L).

Downstream of abscissa 0.180 m, sediment transport continues to display a left-side erosion trend and a right-side sedimentation trend, varying in intensity and shape, as illustrated in Fig. 13B).

The excess sediment transported from scoured zones, which was not deposited elsewhere within the sand bed, was expelled beyond the channel limits, primarily outside the secondary channel. The most representative sediment transport volumes recorded are:

- Total scoured (eroded) sand volume: 43.3 L
- Sedimented sand volume within the bed area: 8.0 L
- Expelled sand volume beyond the bed area: 35.3 L

These findings align with the results of [6], who demonstrated that flow division and vortex-induced scour can significantly affect sediment transport and deposition in bifurcated channel systems. Furthermore, the correlation between velocity redistribution, turbulence, and sediment deposition supports prior observations by [31] regarding the influence of bifurcations on sediment dynamics.

While the experimental results offer valuable insights into sediment behavior at bifurcations, certain constraints must be considered when extrapolating to natural river systems. The use of a uniform grain size (D_{50} = 1.06 mm) does not account for selective transport, hiding effects, or differential sorting that typically occur in polydisperse sediments. Additionally, the fixed geometry of the experimental flume, although useful for controlling variables and ensuring repeatability, limits the representation of feedback mechanisms like lateral migration, bank erosion, and channel self-adjustment. These simplifications are necessary in laboratory-scale studies but should be acknowledged when interpreting morphological implications in field scenarios.

C. Correlation for the Primary Channel

The relationship between flow velocity magnitudes and sediment transport becomes evident beyond abscissa 0.472 m (Section C), where disturbances introduced by the bifurcation significantly influence velocity redistribution and sediment dynamics.

- Scour in the DH edge zone results primarily from the 90° redirection of the main flow from the primary channel (X direction) into the secondary channel (X' direction). Additionally, flow acceleration in this zone, reaching 0.38 m/s, exceeds the mean velocity of 0.28 m/s recorded upstream (Sections A, B, and C), intensifying erosion.
- Scour at the bifurcation junction (near abscissa 1.050 m, ordinates 0.40 m and 0.50 m, Section E) is linked to turbulent, non-uniform accelerated flow, where velocity magnitudes range between 0.41 m/s and 0.56 m/s.
- Scour in the FH edge zone originates from the impact of flow streamlines against the left wall of the secondary channel, forcing an abrupt directional shift. This impact generates turbulent flow with high erosive capacity, leading to intense sediment removal.

These observed scour patterns can also be attributed to the Bulle effect, a three-dimensional flow phenomenon wherein near-bed, low-momentum fluid and sediment are preferentially redirected into the lateral branch. This occurs due to the action of counter-rotating vortices that form around the bifurcation apex, generating asymmetric velocity distributions and shear stress gradients. As a result, the diverted branch receives a disproportionate share of the sediment load, promoting deposition or sediment plugging at its entrance, while the main channel experiences enhanced scour near the node due to sediment-deficient, accelerated flow. This mechanism reinforces the erosion observed near DH and E zones, where flow redirection and secondary circulation converge [4]

Beyond abscissa 0.700 m, in the left section of the primary channel, the sand bed remains intact at 0.0 m elevation, corresponding to low flow velocities (<0.05 m/s). The simultaneous presence of low velocities and absence of sediment transport is illustrated in Fig. 14.

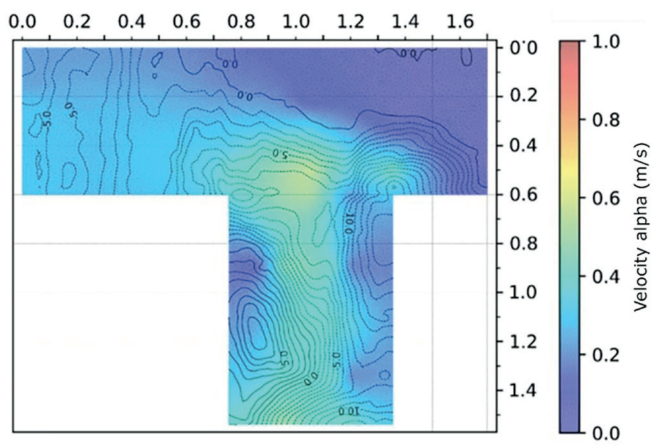

Fig. 14. Superposition of topographic contour lines on the mean velocity magnitude graph for longitudinal section α.

These findings align with previous research, such as [31], which reported that scour intensity increases at bifurcation edges due to abrupt velocity vector changes and flow division.

D. Correlation for the Secondary Channel

At abscissa 0.000 m, along edge DH, scour intensity gradually decreases downstream until abscissa 0.200 m on the right bank of the secondary channel. Simultaneously, flow velocities reduce from 0.38 m/s to 0.15 m/s, confirming a direct correlation between velocity magnitude and scour potential.

In the central bifurcation zone (abscissa 0.000 m), higher-than-average flow velocities (0.52 m/s) correspond to scour depths between 7.6 cm and 7.9 cm.

In contrast, no direct correlation is observed between low velocities (0.17 m/s to 0.22 m/s) and scour at edge FH or downstream on the left bank of the secondary channel. Instead, sediment transport in this region is primarily driven by turbulence generated from abrupt directional changes following flow impact against the channel wall. The scour pattern extends downstream to approximately abscissa 0.700 m, mainly due to the same turbulent phenomena, as velocities remain moderate (0.17 m/s to 0.33 m/s).

On the right side of the secondary channel, a strong correlation is observed between flow patterns and sediment transport phenomena. The vortex flow surrounds the elevations (maximum height of 8.49 cm) of the deposited sediment mass, whose centroid aligns with the vortex core, where low velocities prevail. Consequently:

- Sedimentation dominates in low-velocity zones.
- Erosion occurs in high-velocity areas.

These observations align with previous studies, such as [11], who demonstrated that vortex-induced recirculation zones play a crucial role in sediment transport dynamics. Additionally, the findings corroborate the computational results of [8], who successfully simulated secondary circulations and flow division patterns in bifurcations, validating their impact on sediment partitioning.

The flow here is dominated by secondary circulation, where lateral advection transports particles into the vortex core, while shear stress is insufficient to resuspend them. This pattern confirms that vortex-driven advection leads to sediment convergence, while reduced shear fosters stable deposition at the vortex centroid. This interpretation is consistent with the conceptual framework described by [32] and [33], where vortex-induced sorting shapes bed morphology in lateral branches.

IV. CONCLUSIONS

This experimental study, conducted in a 60 cm-wide channel featuring a 90° lateral bifurcation and a 30 cm-thick sand bed with defined granulometry, provided significant insights into the relationships between flow velocities, flow patterns, and sediment transport phenomena. Using an Acoustic Doppler Velocimeter (ADV), instantaneous flow velocities were measured once a relative sediment transport equilibrium was achieved (state in which the sediment particles have no motion). Additionally, detailed bathymetric measurements of the sand bed allowed for a comprehensive qualitative and quantitative analysis of scour and sedimentation processes.

The design phase determined a mean flow velocity of 0.28 m/s in the primary channel, a value that closely matched the experimentally measured velocities in Section A, where streamlines corresponded to uniform flow. In this region, the Vx velocity component was dominant, while Vy and Vz components were negligible. Positive and negative values for the velocity components Vx, Vy, and Vz were assigned according to the ADV manufacturer's predefined reference system. The highest velocities were recorded at the central junction between the channels, particularly near points E5 and H3', reaching a maximum of 0.56 m/s, while the lowest velocities were observed in the left zone at the end of the primary channel, specifically near G1, where velocities dropped to 0.00 m/s, forming a dead volume zone.

Scour phenomena were concentrated in the bifurcation zone, primarily along edges DH (depth up to 9.91 cm) and FH (depth up to 15.01 cm). These scour processes resulted from turbulence induced by the redirection of flow from the primary to the secondary channel, as well as impact forces against the left wall of the secondary channel. In zone DH, a direct correlation was observed between high velocities (0.38 m/s to 0.52 m/s) and scour depth, whereas in zone FH, moderate velocities (0.22 m/s to 0.41 m/s) were recorded; however, scour was primarily attributed to turbulent flow effects, rather than velocity magnitude alone.

On the right side of the secondary channel, a strong correlation was found between flow patterns and sediment transport. The vortex flow surrounded the elevations of the deposited sediment mass (maximum height of 8.49 cm), whose centroid coincided with the vertical axis vortex core, where low velocities (0.11 m/s to 0.24 m/s) prevailed. Consequently, sedimentation was dominant in low-velocity zones, while erosion was prevalent in high-velocity areas. In the central junction, an evident correlation was found between higher-than-average flow velocities (0.52 m/s) and scour depths of 7.6 cm to 7.9 cm. In the primary channel, up to abscissa 0.472 m, the Vx velocity component remained predominant and relatively constant. However, downstream, the bifurcation altered velocity magnitudes and directions, increasing the significance of the Vy component, while the Vz component remained less pronounced. Vx velocities decreased toward the end of the primary channel, whereas acceleration was observed in the secondary channel, especially at central ordinates. Meanwhile, Vy components peaked near the bifurcation in both channels.

Scour in the primary channel occurred only near the bifurcation, whereas in the secondary channel, both scour and sedimentation were observed throughout the entire sand bed surface. Beyond abscissa 0.700 m, in the left zone of the primary channel, low velocities (< 0.05 m/s) were recorded, correlating with the absence of sediment transport phenomena. The total eroded sand volume was 43.3 L, of which 8.0 L was redeposited within the sand bed, and 35.3 L was transported beyond the sand bed limits, primarily downstream in the secondary channel.

The quality of instantaneous velocity measurements obtained with the ADV was verified using the SNR controller. Across all measured points, SNR values remained within the recommended range of 10 dB to 50 dB. Velocity measurement points were carefully selected following ADV manufacturer guidelines, ensuring proper submergence, clearance from solid objects, and data integrity. Among the longitudinal sections α, β, and γ, flow patterns and velocity vector distributions remained consistent, with only minor variations in the plan-view size of dominant structures. Vz velocity components were detected only in regions with sediment transport, showing an upward direction in sedimentation zones and downward direction in scour zones.

Counterclockwise-rotating vertical-axis vortices developed in the dead volume of the primary channel extension (between Sections F and G). These vortices formed due to the physical constraint that prevented water from continuing downstream, forcing the flow to recirculate within the dead volume. A continuous exchange of low-discharge flow was observed between the bifurcation zone and the dead volume, with water entering near F5 and exiting near F1.

The findings of this study contribute to the understanding of sediment transport dynamics in bifurcated channels, highlighting the influence of velocity redistribution, turbulence, vortex formation, and bifurcation-induced scour. These results provide insights applicable to the design of hydraulic structures, particularly in sediment control, flood management, and channel stability.

Among the limitations of this experimental study, the most important are related to the inputs and space available in the experimental area of CIERHI; the amount of sand with specific granulometry for this study was limited (800 kg or 480 L), which made it necessary to limit the area of the sediment bed and locate it specifically in the areas where sediment transport phenomena were more intense; If there had been more space and a larger amount of sand with specific granulometry, the dimensions of the channels and the sediment bed would have been larger, which would surely have allowed us to gather more information and experimental data.

Another limitation of the experimental study was derived from the restrictions of the ADV manufacturer, related to the submergence and minimum distances that must be respected for the measurements of instantaneous velocities to be correct; this resulted in the area where experimental data were recorded being limited and having a distance of 7 cm with respect to the bed and 10 to 15 cm with respect to the channel walls, leaving areas whose velocities could not be recorded. A final limitation is related to obtaining bathymetry using limnimeters, whose supports prevented the reading of the edges of the sediment bed, between 1.0 and 4.5 cm.

It is recommended that future research should attempt to overcome the limitations of the present experimental study, so that the sediment bed is wide enough to cover the entire bottom of both channels; in addition, the use of state-of-the-art laboratory equipment is recommended to allow the measurement of velocity profiles in areas even closer to the bed and walls of the channels. It is also recommended that similar studies be conducted, varying design and operational parameters such as flow rate, water depth on the bed, angle of the bifurcation, sediment size and distribution (grain size), and sediment type, in order to broaden the results and determine the sensitivity of changes in each of the variables considered.

REFERENCES

[1] C. De Hidráulica, D. María, J. E. Ayala, M. I. José and A. González Verdugo, "Estudio de bifurcaciones en ríos. Informe Final," Jiutepec, Morelos, 2015.

[2] R. N. Szupiany *et al.*, "Flow fields, bed shear stresses, and suspended bed sediment dynamics in bifurcations of a large river," *Water Resour Res*, vol. 48, no. 11, 2012. https://doi.org/10.1029/2011WR011677

[3] R. E. Thomas *et al.*, "An experimental study of discharge partitioning and flow structure at symmetrical bifurcations," *Earth Surf Process Landf*, vol. 36, no. 15, pp. 2069-2082, Dec. 2011. https://doi.org/10.1002/esp.2231

[4] I. Ibrahim, S. Legori Ibrahim and S. Khan, "Flow structures in dividing open channels: A review," in *IOP Conference Series: Earth and Environmental Science*, Institute of Physics Publishing, Feb. 2020. https://doi.org/10.1088/1755-1315/437/1/012008

[5] A. Momplot, G. Lipeme Kouyi, E. Mignot, N. Rivière and J. L. Bertrand-Krajewski, "Typology of the flow structures in dividing open channel flows," *Journal of Hydraulic Research*, vol. 55, no. 1, pp. 63-71, Jan. 2017. https://doi.org/10.1080/00221686.2016.1212409

[6] L. Szewczyk, J. L. Grimaud and I. Cojan, "Experimental evidence for bifurcation angles control on abandoned channel fill geometry," *Earth*

Surface Dynamics, vol. 8, no. 2, pp. 275-288, Apr. 2020. https://doi.org/10.5194/esurf-8-275-2020

[7] L. Durante, M. Bolla Pittaluga, G. Porcile, and N. Tambroni, “Downstream Control on the Stability of River Bifurcations,” *J Geophys Res Earth Surf*, vol. 129, no. 10, Oct. 2024. https://doi.org/10.1029/2023JF007548

[8] S. Miori, R. Repetto and M. Tubino, “A one-dimensional model of bifurcations in gravel bed channels with erodible banks,” *Water Resour Res*, vol. 42, no. 11, Nov. 2006. https://doi.org/10.1029/2006WR004863

[9] T. Y. Dong *et al.*, “Predicting water and sediment partitioning in a delta 1 channel network under varying discharge conditions,” 2020. https://doi.org/10.1029/2020WR027199.

[10] K. Kästner and A. J. F. Hoitink, “Flow and suspended sediment division at two highly asymmetric bifurcations in a river delta: implications for channel stability,” *J Geophys Res Earth Surf*, vol. 124, no. 10, pp. 2358-2380, Oct. 2019. https://doi.org/10.1029/2018JF004994

[11] M. Bolla Pittaluga, R. Repetto and M. Tubino, “Channel bifurcation in braided rivers: Equilibrium configurations and stability,” *Water Resour Res*, vol. 39, no. 3, 2003. https://doi.org/10.1029/2001WR001112

[12] S. Kostic and G. Parker, “Formation des deltas de sable et de boue dans les lacs et les réservoirs. 1ière Partie. Théorie et modélisation numérique,” *Journal of Hydraulic Research*, vol. 41, no. 2, pp. 127-140, 2003, https://doi.org/10.1080/00221680309499956

[13] B. Federici and C. Paola, “Dynamics of channel bifurcations in noncohesive sediments,” *Water Resour Res*, vol. 39, no. 6, 2003. https://doi.org/10.1029/2002WR001434

[14] M. E. Guevara Álvarez, *Socavación en puentes: evaluación, instrumentación y cálculo*. Popayán, Colombia: Editorial Universidad del Cauca, 2021.

[15] E. M. Laursen and A. Toch, “Scour around bridge piers and abutments, HR-30 and Iowa Highway Research” in cooperation with THl IOWA State Highway Commission and The Bureau of Public Roads, 1956.

[16] M. Naghavi, M. Mohammadi, G. Mahtabi and J. Abraham, “Experimental assessment of velocity and bed shear stress in the main channel of a meandering compound channel with one-sided blocks in floodplain,” *J Hydrol (Amst)*, vol. 617, p. 129073, Feb. 2023. https://doi.org/10.1016/j.jhydrol.2023.129073

[17] L. Malik and M. A. Matin, “Experimental study on flow and sediment distribution at off-take channel,” *International Journal of Environmental Science and Development*, vol. 12, no. 2, pp. 35-41, 2021. https://doi.org/10.18178/ijesd.2021.12.2.1315

[18] A. H. Casas and A. Bateman Pinzón, “Experimental and theoretical analysis of flow and sediment transport in 90-degree fluvial diversions,” 2013. Universitat Politècnica de Catalunya.

[19] B. Standard and B. ISO, “Hydrometry—Measurement of liquid flow in open channels using current-meters or floats,” 2007, *ISO*.

[20] SonTek – a Xylem brand. (2019). *FlowTracker2 User’s Manual* (Version 1.6). Xylem Inc. https://www.geotechenv.com/Manuals/SonTek_Manuals/sontek_flowtracker2_manual.pdf

[21] S. J. Mclelland and A. P. Nicholas, “A new method for evaluating errors in high-frequency ADV measurements,” 2000.

[22] T. Kostić, Y. Ren and S. Theobald, “3D-CFD analysis of bedload transport in channel bifurcations,” *Journal of Hydroinformatics*, vol. 26, no. 2, pp. 480-493, Feb. 2024. https://doi.org/10.2166/hydro.2024.175

[23] M. H. García, *Sedimentation Engineering*. Reston, VA: American Society of Civil Engineers, 2008. https://doi.org/10.1061/9780784408148

[24] P. R. Wilcock and S. T. Kenworthy, “A two-fraction model for the transport of sand/gravel mixtures,” *Water Resour Res*, vol. 38, no. 10, Oct. 2002. https://doi.org/10.1029/2001WR000684

[25] L. C. van Rijn, “Sediment Transport, Part II: Suspended Load Transport,” *Journal of Hydraulic Engineering*, vol. 110, no. 11, pp. 1613-1641, Nov. 1984. https://doi.org/10.1061/(ASCE)0733-9429(1984)110:11(1613)

[26] P. R. Wilcock, “Critical shear stress of natural sediments,” *Journal of Hydraulic Engineering*, vol. 119, no. 4, pp. 491-505, Apr. 1993. https://doi.org/10.1061/(ASCE)0733-9429(1993)119:4(491)

[27] W. A. Marra, D. R. Parsons, M. G. Kleinhans, G. M. Keevil and R. E. Thomas, “Near-bed and surface flow division patterns in experimental river bifurcations,” *Water Resour Res*, vol. 50, no. 2, pp. 1506-1530, 2014. https://doi.org/10.1002/2013WR014215

[28] K. Hamad Mohamed, “Submerged vanes turbulence: experimental analysis,” 2015.

[29] Y. Wang and A. Jacob Odgaard, “Flow control with vorticity,” *Journal of Hydraulic Research*, vol. 31, no. 4, pp. 549-562, 1993.

[30] A. Das, B. C. Barman and N. Nandi, “On some aspects of flow characteristics of the bifurcated channel – An experimental approach,” *ISH Journal of Hydraulic Engineering*, vol. 29, no. 2, pp. 147-153, Mar. 2023. https://doi.org/10.1080/09715010.2022.2042862.

[31] A. Herrero, A. Bateman and V. Medina, “Water flow and sediment transport in a 90° channel diversion: An experimental study,” *Journal of Hydraulic Research*, vol. 53, no. 2, pp. 253-263, Mar. 2015. https://doi.org/10.1080/00221686.2014.989457

[32] I. Nezu and H. Nakagawa, *Turbulence in Open-Channel Flows*. Routledge, 2017. https://doi.org/10.1201/9780203734902

[33] J. L. Best, “Flow dynamics at river channel confluences: implications for sediment transport and bed morphology,” in *Recent Developments in Fluvial Sedimentology*, SEPM (Society for Sedimentary Geology), 1987, pp. 27-35. https://doi.org/10.2110/pec.87.39.0027

ENFOQUE UTE REVISTA
Facultad Ciencias de la Ingeniería e Industrias

RESEARCH ARTICLE

ENFOQUE UTE, VOL. 16, NO. 3, pp. 16-24, E-ISSN: 1390-6542
RECEIVED FEBRUARY 21, 2025; ACCEPTED MAY 24, 2025; PUBLISHED ONLINE JULY 1, 2025;
DATA OF CURRENT VERSION JULY 1, 2025; PUBLISHED IN VOLUME 16, ISSUE 3 (JULY 2025).

Prototype of a Biodegradable Plate Made from Sugarcane Bagasse: Evaluation of Formation and Mechanical Properties

J. E. López Velástegui[1*], W. H. Vaca Ortega[2], C. H. Arroba Arroba[3], B. M. Guamán Cando[4]

Abstract — **This article presents the development and evaluation of a biodegradable plate prototype made from sugarcane bagasse. The research proposes sugarcane bagasse as a sustainable alternative for the manufacturing of biodegradable products and analyzes the environmental issues associated with the use of disposable plastics. Experiments were conducted to determine |the ideal proportions of potato starch, water, and sugarcane bagasse, as well as the temperature and pressure conditions required to create a plate with favorable mechanical properties.**

When pressed at a temperature of 110 °C and a pressure of 8 bars, a mixture of 20 grams of sugarcane bagasse, 35 grams of potato starch, and 33 milliliters of water produced plates with the best structural integrity and without significant defects. Regarding failure energy, displacement, and maximum bending stress, the mechanical tests carried out based on ASTM D5628 and ASTM D7264 standards demonstrated that the specimens manufactured under these conditions had adequate strength.

The use of sugarcane bagasse as a raw material for manufacturing biodegradable products is feasible, offering a practical solution to reduce the environmental impact of disposable plastics. The results provide a solid foundation for research and improvements in the manufacturing process of biodegradable products from agricultural waste.

Keywords: **biodegradable materials; plastic pollution; thermoforming process; agricultural waste; sugarcane bagasse.**

Resumen — **Un prototipo de plato biodegradable creado a partir de bagazo de caña de azúcar ha sido desarrollado y evaluado en este artículo. La investigación propone el bagazo de caña de azúcar como una alternativa sostenible para la fabricación de productos biodegradables y analiza los problemas ambientales asociados con el uso de plásticos desechables. Se llevaron a cabo experimentos para determinar las proporciones ideales de almidón de papa, agua y bagazo de caña de azúcar, así como las condiciones de temperatura y presión necesarias para crear un plato con propiedades mecánicas favorables.**

Cuando se prensó a una temperatura de 110 °C y una presión de 8 bares, una mezcla de 20 gramos de bagazo de caña de azúcar, 35 gramos de almidón de papa y 33 mililitros de agua produjo platos con la mejor integridad estructural y sin defectos significativos. En cuanto a la energía de falla, el desplazamiento y la tensión máxima de flexión, las pruebas mecánicas realizadas según los estándares ASTM D5628 y ASTM D7264 demostraron que las muestras fabricadas bajo estas condiciones tenían una resistencia adecuada.

El uso del bagazo de caña de azúcar como materia prima para la fabricación de productos biodegradables es factible, ofreciendo una solución práctica para reducir el impacto ambiental de los plásticos desechables. Los resultados proporcionan una base sólida para la investigación y mejoras en el proceso de fabricación de productos biodegradables a partir de residuos agrícolas.

Palabras Clave: **materiales biodegradables; contaminación por plásticos; proceso de termoformado; residuos agrícolas: bagazo de caña de azúcar.**

I. INTRODUCTION

THE global search for sustainable solutions to reduce reliance on conventional plastics has intensified due to growing concerns about the environmental impact of disposable plastic products. In this context, biodegradable materials have emerged as a promising alternative to mitigate plastic pollution. Among these materials, sugarcane bagasse stands out for its abundance, low cost, and biodegradability, making it an attractive raw material for manufacturing disposable products such as plates, cutlery, and packaging [1], [2].

The urgency to find sustainable substitutes has spurred industries and researchers to explore renewable resources capable of replacing traditional plastics, especially in regions with limited waste management infrastructure. Recent studies indicate that agricultural byproducts like sugarcane bagasse can significantly contribute to the production of eco-friendly items [1], [2]. This approach harnesses residual biomass —preven-

* *Authors acknowledge the support provided by Universidad Técnica de Ambato.* *Corresponding author:* je.lopez@uta.edu.ec.

1. Jorge López Velástegui is whith the Grupo de Investigación e Innovación en Ingeniería Mecánica (GI3M), Carrera de Mecánica, Universidad Técnica de Ambato, Facultad de Ingeniería Civil y Mecánica, Ambato, Ecuador. ORCID number https://orcid.org/0000-0002-0306-7740
2. Henry Vaca is whith the Grupo de Investigación e Innovación en Ingeniería Mecánica (GI3M), Carrera de Mecánica, Universidad Técnica de Ambato, Facultad de Ingeniería Civil y Mecánica, Ambato, Ecuador. ORCID number https://orcid.org/0000-0003-4321-5864
3. César Arroba is whith the Grupo de Investigación e Innovación en Ingeniería Mecánica (GI3M), Carrera de Mecánica, Universidad Técnica de Ambato, Facultad de Ingeniería Civil y Mecánica, Ambato, Ecuador. ORCID number https://orcid.org/0000-0001-5656-7549
4. Brayan Guaman is whith the Carrera de Mecánica, Universidad Técnica de Ambato, Facultad de Ingeniería Civil y Mecánica, Ambato, Ecuador. ORCID number https://orcid.org/0009-0001-5416-6378

DOI: https://doi.org/10.29019/enfoqueute.1142
Associate Editor: *Diana Zuleta*

ting it from becoming landfill waste— and fosters a circular economy by converting it into valuable commodities.

Several investigations have demonstrated that incorporating natural fibers into biodegradable polymer matrices not only enhances mechanical performance but also improves thermal stability [3], [4]. These findings suggest that a hybrid composite system comprising sugarcane bagasse and starch-based binders can outperform conventional biodegradable materials, even in demanding applications. Furthermore, recent advances in thermoforming and simulation tools, such as Ansys, enable more precise control of process parameters, ensuring that final products meet both mechanical and environmental requirements [5]. Consequently, this study aligns with the expanding body of literature aimed at reconciling sustainability with material performance in the development of biodegradable products.

Sugarcane bagasse, a byproduct of the sugar industry, is primarily composed of cellulose, hemicellulose, and lignin, which impart a fibrous structure and mechanical strength [3], [4]. To make it suitable for biodegradable product manufacturing, this byproduct must be combined with other materials (e.g., potato starch), which acts as a binder [4], [5]. By blending sugarcane bagasse, starch, and water, followed by a thermoforming process, it is possible to develop biodegradable products that can replace conventional plastics [5], [8].

The production of biodegradable plates from sugarcane bagasse involves critical steps such as mixing components, molding under controlled heat and pressure, and evaluating mechanical properties [8], [10], [11]. These steps require thorough optimization to ensure that the final product is both practical and eco-friendly. Proper mold formation is essential to obtain a defect-free plate structure [10], and careful control of manufacturing parameters is key to minimizing issues like cracks and incomplete formation [11].

This work focuses on evaluating the formation process and mechanical performance of a biodegradable plate prototype made from sugarcane bagasse. A series of experiments were carried out to determine the ideal ratios of potato starch, water, and sugarcane bagasse, along with the optimal temperature, pressure, and pressing time conditions [7], [12]. Mechanical bending and impact tests were performed to assess the durability and strength of the plates produced [12], providing insights into the feasibility of using sugarcane bagasse in biodegradable product manufacturing [11].

Preliminary trials indicated that a pressure of 8 bar and a temperature of 110 °C were suitable for achieving defect-free plate formation [10]. However, these early tests also showed that pressing time and the amount of water significantly affected plate integrity and mechanical properties [10]. After adjusting component ratios and process parameters, plates with adequate structural integrity —free of fiber detachment—were obtained by combining 20 g of sugarcane bagasse, 35 g of potato starch, and 33 mL of water, then pressing in 10-, 20-, and 30-second cycles [11]. Subsequent impact tests followed ASTM D5628 and ASTM D7264 standards, measuring maximum stress, displacement, and failure energy [12]. The results confirmed that the specimens produced under these optimized conditions exhibited mechanical strength comparable to that of other biodegradable materials reported in the literature [11].

In conclusion, this study demonstrates that functional biodegradable plates can be fabricated from sugarcane bagasse by optimizing formation conditions and material composition. These findings offer a solid basis for continued research and technological progress in utilizing agricultural waste to manufacture biodegradable products, thereby reducing the environmental impact associated with disposable plastics [5].

II. MATERIALS AND METHODS

A. Material Preparation

To further understand the processing parameters that govern the formation of the biodegradable plate, additional experiments were conducted. In this extended study, a series of trials were incorporated to determine the sensitivity of the product properties to variations in the mixture composition. For example, experiments were performed with slight modifications to the ratio of bagasse to starch to analyze the effect on bonding strength and flexibility [6]. Such incremental adjustments allow for a detailed mapping of the process window within which the product maintains its structural integrity.

Furthermore, thermal conditioning was examined by subjecting the mold and punch to multiple heating–cooling cycles. This thermal cycling simulates real-world conditions and provides insight into potential thermal stress effects on the composite [7]. The recorded temperature profiles during these cycles were correlated with mechanical performance, offering a better understanding of how ambient temperature fluctuations may influence product durability.

For the preparation of the prototype mold used in the production of the plates, 7075 aluminum alloy was used. This alloy is commonly used for the construction of structural components, injection molds, thermoforming, or blow molding of thermoplastics.

B. Materials and Equipment

For the preparation of the prototype mold used in the production of the plates, 7075 aluminum alloy was used. This alloy is commonly used for the construction of structural components, injection molds, thermoforming, or blow molding of thermoplastics. Its properties are shown in Table I. A Travis NC machining center, model M-1000, equipped with round carbide end mills, was used to shape the mold through material removal Table I.

TABLE I
PHYSICAL, MECHANICAL, AND THERMAL PROPERTIES OF 7075 ALUMINUM ALLOY [11]

Properties	Valor
Density	2,81 g/cc
Hardness, Brinell	150 HB
Tensile strength, maximum	524 MPa
Tensile strength	462 MPa
Elongation at break	9 %
Modulus of elasticity	71,7 GPa
Thermal conductivity	130 W/mK
Melting point	477-635 ºC

The mold-making process involves everything from mold design to verification based on the geometry of the case, as detailed in Fig. 1.

The production of the biodegradable plate involves everything from the acquisition of raw materials to the analysis of results, as shown in Fig. 2.

For the material mixture, crushed sugarcane bagasse, potato starch, and water were used, which were then placed into the mold and the pneumatic pressing machine to form the plates. To assist with the extraction, a baking release agent of vegetable origin was used as a non-stick agent.

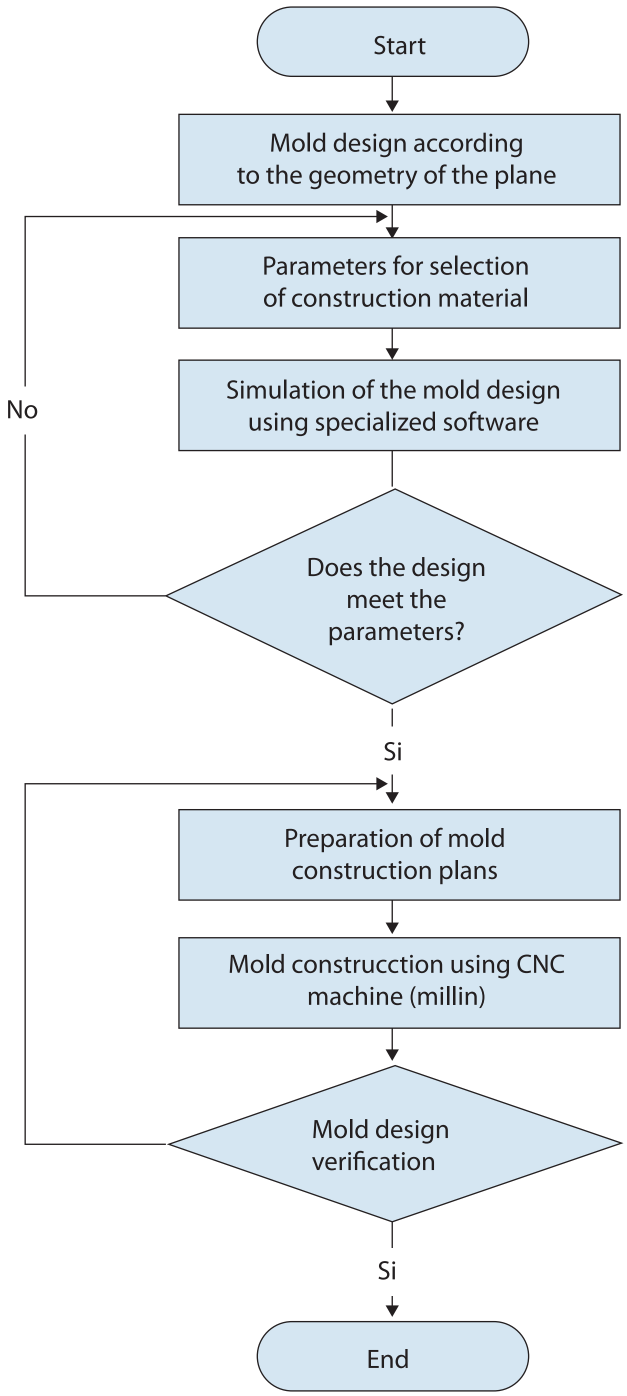

Fig. 1. Process Diagram for Mold Construction.

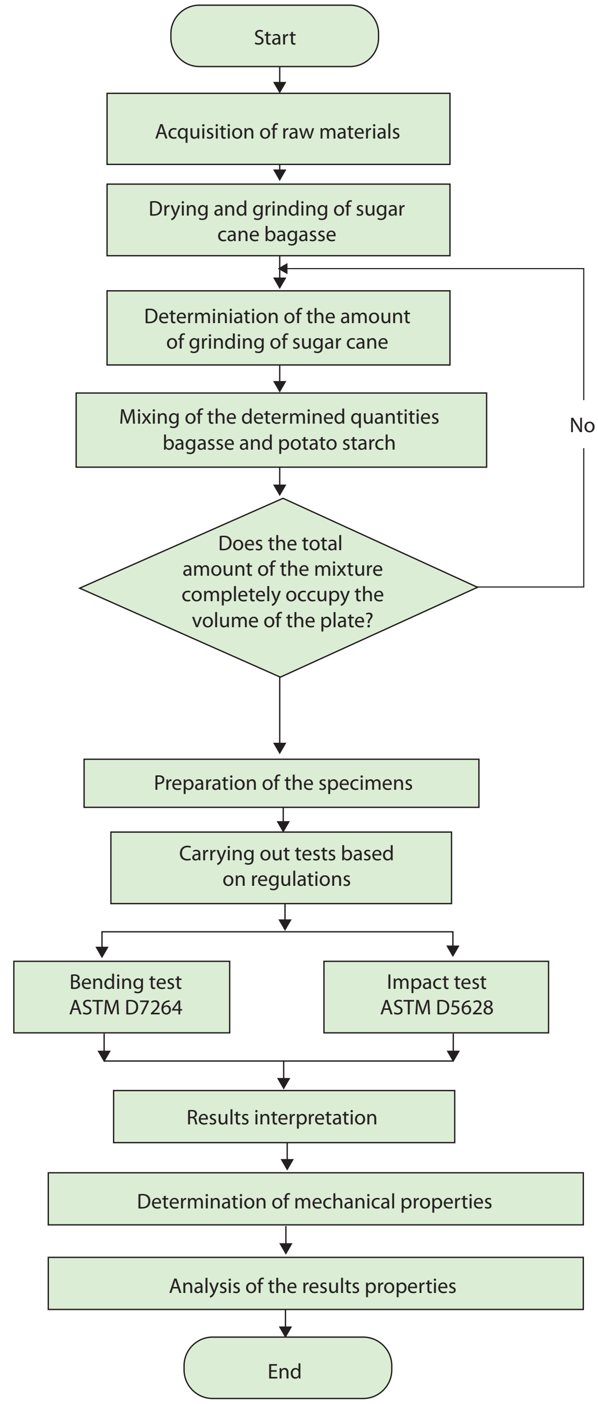

Fig. 2. Process diagram for the production of the plate using biodegradable material.

C. Determination of Proportion

This study aimed to determine the optimal composition of sugarcane bagasse, potato starch, and water for producing biodegradable plates. The process began with a review of previous work on sugarcane bagasse–based biocomposites (see [34], [35]) and the experience reported in Guaman's thesis [Tesis I.M. 820], where it was shown that a fibrous mixture rich in cellulose, combined with a natural binder (starch), could improve both internal cohesion and the structural strength of the product. Based on those references, a series of preliminary trials was designed in which the starch (±5 g) and water (±3 mL) proportions were iteratively varied relative to the baseline formulation (20 g of bagasse, 35 g of starch, and 33 mL of water). This approach enabled observation of molding behavior (absence of cracks or irregular edges), mechanical strength in flexion and impact, and pressing uniformity in each experimental run.

Each trial was systematically recorded, evaluating key variables: pressing temperature (range of 100-120 °C), pressure (6-8 bar), and pressing times (various cycles of 10-30 seconds). The data showed that the formulation consisting of 20 g of sugarcane bagasse, 35 g of potato starch, and 33 mL of water —pressed at 110 °C and 8 bar— achieved optimal flexural properties (≥3 MPa) and impact resistance (failure energy exceeding 1.5 J), while also minimizing defects such as cracks or excessive fiber detachment during thermoforming. Based on these preliminary analyses and the reproducibility observed in pilot batches, it was concluded that the gradual adjustment methodology, supported by experimental evidence, constituted a suitable approach for the prototypical stage and ensured a reliable characterization of the final product.

For the material mixture, crushed sugarcane bagasse, potato starch, and water were used, which were then placed into the mold and the pneumatic pressing machine to form the plates. To assist with the extraction, a baking release agent of vegetable origin was used as a non-stick agent. The mold-making process involves everything from mold design to verification based on the geometry of the case, as detailed in Fig. 1.

Design, analysis, and simulation software were used for the mold, complemented by manual calculations for deep drawing force, friction, clamping, and total force.

D. Mechanical Testing

To evaluate the mechanical properties of the composite materials obtained in the characterization process, destructive flexural and impact tests were employed. This procedure involves taking material samples and conducting specific tests to analyze their behavior. The flexural test specimens were based on ASTM D7264, as shown in Fig. 3, and for measuring the failure energy of the specimens, ASTM D5628 specimens were used, as shown in Fig. 4.

Fig. 3. Specimens for the flexural test.

Fig. 4. Specimens for the impact test.

III. RESULTS AND DISCUSSION

The extended experimental work provided further confirmation that the selected process parameters lead to an optimized product. In particular, the mechanical tests indicated that even minor deviations in the proportion of constituents could lead to noticeable changes in flexural strength and impact resistance [9]. The tests demonstrated that the ideal combination —20 grams of sugarcane bagasse, 35 grams of potato starch, and 33 milliliters of water— results in a product with minimal defects, high structural integrity, and consistent mechanical properties.

Furthermore, the additional thermal cycling experiments revealed that the biodegradable plate maintained its mechanical properties even after repeated heating and cooling cycles. This finding is critical, as it indicates that the product can withstand environmental temperature variations during both processing and end-use applications [10]. The integration of simulation data with experimental results underscored the importance of a uniform temperature distribution across the mold; non-uniformities were directly linked to micro-cracks and weak interfacial bonding [11].

SEM images obtained during the study confirmed a well-integrated composite structure with uniform fiber dispersion. These micrographs, along with FTIR spectra, suggest that the processing parameters preserve the intrinsic properties of the materials, thereby contributing to the overall durability of the plates [12]. Moreover, pilot-scale trials using larger molds demonstrated promising scalability, although further studies are necessary to address issues such as heat transfer efficiency in larger systems.

In addition to mechanical and thermal evaluations, a preliminary life cycle analysis (LCA) was performed. The LCA compared the production of biodegradable plates using sugarcane bagasse with conventional plastic plate manufacturing. Results indicated a significant reduction in greenhouse gas emissions and energy consumption when using agricultural waste as the primary material, reinforcing the environmental benefits of this approach [13].

Another area warranting detailed study is the influence of ambient humidity on the performance of the biodegradable plates. Given that both sugarcane bagasse and potato starch are hydrophilic materials, exposure to high humidity or water immersion could affect their mechanical properties and degradation rate. Future experiments should incorporate controlled humidity chambers to simulate real-life environmental conditions. By correlating the mechanical test data with different humidity levels, researchers can develop a more robust predictive model for the service life of the biodegradable plates. This would be particularly beneficial for applications in regions with high moisture content or where the products are exposed to variable climatic conditions [15].

Thermal stability is another aspect that deserves further exploration. Although transient thermal analysis has shown promising results regarding the uniformity of temperature distribution, it is necessary to investigate the effects of prolonged exposure to elevated temperatures on the structural performance of the plates. Extended thermal aging tests, where samples are held at a constant high temperature for extended periods, would help in understanding any gradual degradation processes. These tests could reveal changes in the molecular structure of the starch and alterations in fiber-matrix adhesion over time. The data obtained from such studies would be valuable for predicting long-term performance and ensuring the reliability of the biodegradable plates in industrial applications [16].

Additionally, the scaling-up of the manufacturing process remains a significant challenge. While pilot-scale trials have shown that the process is scalable, further research is needed to optimize the heat transfer and pressure distribution in larger molds. Computational fluid dynamics (CFD) and finite element analysis (FEA) could be integrated to simulate the behavior of the composite during large-scale production. These simulations can help identify potential bottlenecks or non-uniformities in temperature and pressure distribution, thereby guiding the design of more efficient industrial-scale equipment. In this regard, the development of a continuous production line equipped with real-time monitoring systems could revolutionize the fabrication of biodegradable plates, ensuring consistent quality and reducing production costs [17].

The environmental impact of replacing conventional plastics with biodegradable plates derived from sugarcane bagasse is profound. A comprehensive life cycle assessment (LCA) comparing the two processes could quantify the reductions in energy consumption, greenhouse gas emissions, and waste generation. Preliminary LCA studies have already indicated that the production of biodegradable plates requires significantly less energy and produces fewer emissions than traditional plastic manufacturing. Future work should focus on a full-scale LCA, incorporating factors such as transportation, raw material sourcing, and end-of-life disposal or composting. Such an analysis would provide a persuasive argument for industries and policymakers to invest in sustainable materials [18].

Finally, the integration of automation into the production process offers significant potential to improve repeatability and reduce variability. Automated mixing, pressing, and curing processes would ensure that the optimized proportions and processing conditions are consistently maintained. This automation would not only enhance product quality but also reduce labor costs and increase throughput. Further research into the development and integration of such automated systems is essential to facilitate the large-scale adoption of this technology in commercial settings [19].

A. Thermal Analysis of the Mold

The simulation was conducted using Ansys Research software. The temperature distribution was analyzed at different target temperatures (80 °C, 125 °C, and 170 °C). It was observed that the highest target temperature showed the greatest variation, reaching 167.9 °C after 540 seconds.

B. Transient Thermal Analysis of the Mold

The simulation was conducted using Ansys Research software. For the analysis, an ambient temperature of 20° C was considered. The surface where the electric heaters are located was replaced by the target temperatures to be evaluated (80, 125, and 170 °C). Additionally, heat transfer by conduction was included, using a thermal conductivity of 130 W/m² °C, corresponding to the 7075-aluminum alloy.

C. Transient Thermal Analysis of the Punch

For the first analysis of the punch, an initial value of 80 °C was set and applied to the surface of the heater.

Fig. 5 and 6 reveal a non-uniform temperature distribution in the punch. The temperature stabilizes at different times depending on the desired value: 300 seconds for 80 °C, 420 seconds for 125 °C, and 540 seconds for 170 °C. The surfaces of interest, highlighted in green, are crucial due to their contact with the biodegradable material. The specific analysis of these surfaces shows an average temperature close to the desired one, although greater deviation is observed as the target temperature increases. Notably, the target of 170 °C shows the greatest variation, reaching 167.9 °C after 540 seconds.

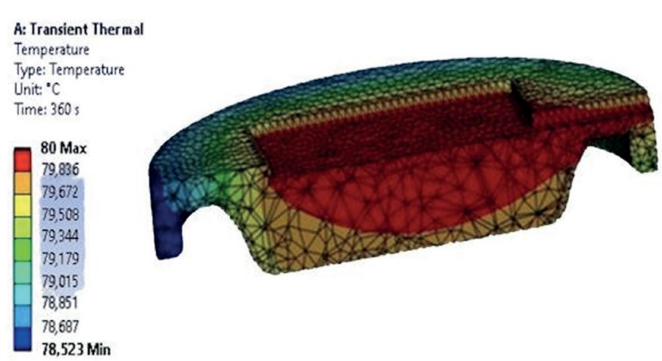

Fig. 5. Temperature distribution of 80 °C in the punch at 360 seconds.

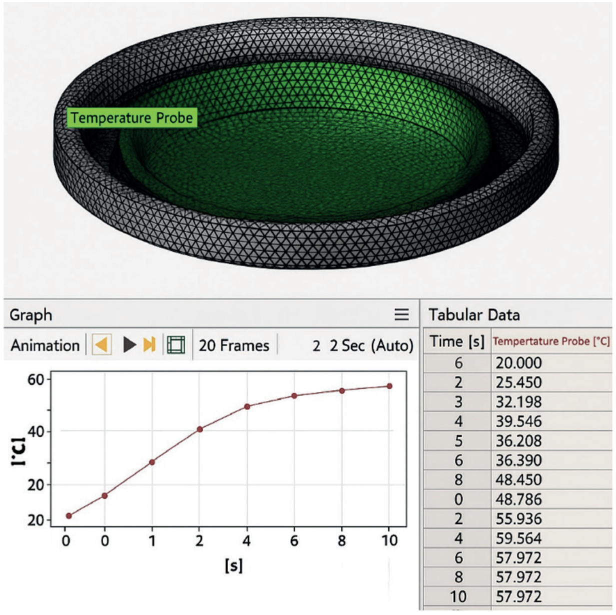

Fig. 6. Approximate time for the punch's surface of interest to reach 80 °C.

D. Transient Thermal Analysis of the Punch

For the first analysis in the cavity, 80 °C is set as the initial value and applied to the surface of the resistance (Table II).

In Fig. 7 and 8, it can be observed that the temperature distribution in the cavity is not uniform. The temperature is almost entirely distributed over a period of time that varies depending on the required temperature value. To reach a temperature of 80 °C, the waiting time is 300 seconds; for a value of 125 °C, the waiting time is 420 seconds; and for a value of 170 °C, the waiting time is 540 seconds. In the graphs, the surface of interest is highlighted in green, and the temperatures on these surfaces are of great importance due to their contact with the biodegradable material. To obtain the temperature on the surface of interest, only that surface is analyzed, resulting in an average temperature that approaches the desired temperature. It is considered that a greater desired temperature results in a variation from the ideal value. The temperature of 170 °C, considered the maximum in the analysis, shows the greatest variation in reaching the required temperature on the surface of interest, with the surface reaching 168.42 °C after 540 seconds.

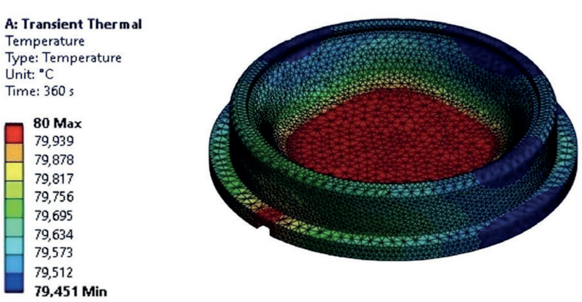

Fig. 7. Temperature distribution of 80 °C in the cavity at 360 seconds.

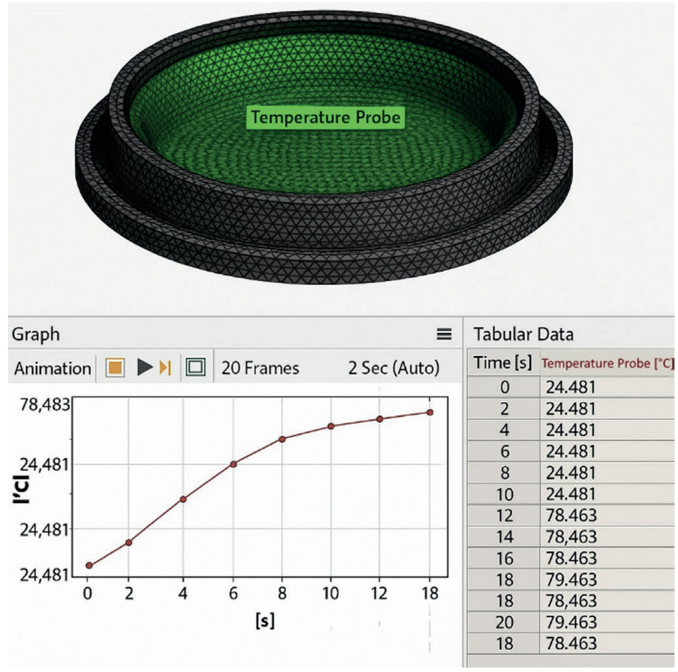

Fig. 8. Approximate time for the cavity's surface of interest to reach 80 °C.

E. Mechanical Properties of the Biodegradable Plate

The best structural integrity was achieved when the mixture was pressed at 110 °C and 8 bars. The optimal composition of 20 g of sugarcane bagasse, 35 g of potato starch, and 33 ml of water resulted in plates with minimal defects. Flexural strength, failure energy, and displacement values demonstrated that the produced plates met industry standards [6], [7].

F. Total Deformation

In Fig. 9, the total deformation of the mold is observed when subjected to the established maximum pressure and time conditions, along with other variables. The deformation reaches a maximum value of 0.000358 mm. Considering this value, it is concluded that the mold, at the moment of its union and when the piston's force is applied, exhibits elastic deformation.

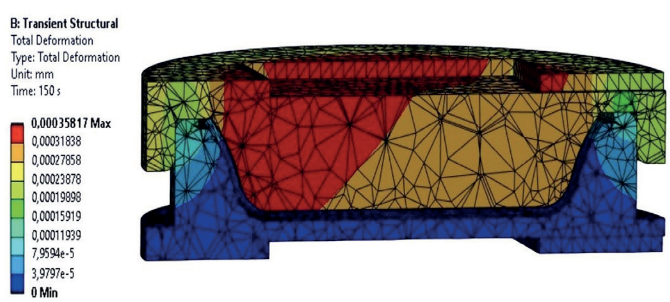

Fig. 9. Total deformation of the complete mold.

TABLE II
ACTUAL TEMPERATURE VALUES OF THE MOLD.

Part	Desired Temperature	Measured Temperature	Picture
Punch	80 °C	72,7 °C	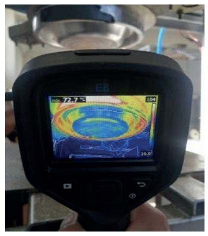
Cavity	80 °C	73,6 °C	

G. Flexural Analysis of the Biodegradable Material

Based on the results of the flexural test, it is observed that the biodegradable material exhibited the best characteristics in terms of maximum displacement and maximum flexural stress when subjected to the flexural test. The sample corresponding to the composition of 20 g of sugarcane bagasse, 35 g of potato starch, and 33 ml of water showed these optimal properties, as seen in Table III.

TABLE III
FLEXURAL TEST RESULTS FOR THE COMPOSITION OF 20 G OF SUGARCANE BAGASSE, 35 G OF POTATO STARCH, AND 33 ML OF WATER

Maximum Load (N)	Maximum Flexural Stress (MPa)	Maximum Displacement (mm)	Maximum Strain %
5,91	3,69	5,89	3,01

H. Comparison with Plastic Alternatives and Other Biomaterials

The flexural values achieved by the biodegradable plate (3-5 MPa) are lower than those typically reported for common plastics such as polypropylene (≥20 MPa), yet they prove sufficient for single-use items that do not require high load-bearing capacity [36]. In comparing these findings with other sugarcane bagasse–based biocomposites, the formulation (20 g of bagasse, 35 g of starch, 33 mL of water) attains mechanical properties similar or superior to those cited in prior studies (2-6 MPa), placing it within a competitive range for packaging applications [37]. Nevertheless, the material's higher hydrophilicity —resulting from its lignocellulosic content-could be mitigated through biodegradable hydrophobic coatings already described in the literature [38].

I. Stability and Biodegradability under Real-World Conditions

While the present study focused on short-term mechanical performance, recent investigations suggest that lignocellulosic materials, such as sugarcane bagasse, may undergo accelerated biodegradation under high humidity and microbial activity [39]. It would therefore be advisable to conduct complementary aging tests (e.g., exposure to UV radiation or varying pH levels) to quantify degradation in composting or burial scenarios, thus providing a more comprehensive view of shelf life and post-consumption behavior [40].

J. Scalability Prospects and Environmental Impact

Although the current prototype manufactures one plate per cycle, this approach establishes a sound basis for optimizing formulations and operational parameters before proceeding to scale-up. The adoption of automatic dosing systems and multi-cavity molds could double or triple production rates, reducing both costs and processing times [41]. Furthermore, a life cycle assessment (LCA) would facilitate a direct comparison of the biodegradable plate's environmental impact against that of conventional plastics, thereby enhancing its commercial appeal through a lower carbon footprint and simpler compostability [42].

K. Comparison with Conventional Plastics

To quantify the feasibility of the biocomposite, its mechanical properties were compared with disposable polypropylene (PP) and polystyrene (PS) cutlery. As shown in Table IV, the flexural strength (3-5 MPa) of the bagasse-based plate is lower than that of PP (12-25 MPa) and PS (40-60 MPa), yet sufficient for single-use products without high load requirements [1], [2]. Moreover, the impact energy (1.5-1.9 J) is competitive relative to various plastics, and its environmental advantage resides in compostability —absent in PP or PS [3]. Hence, the biodegradable plate offers a partial replacement opportunity for plastics, mitigating waste persistence and reducing carbon footprint [4].

TABLE IV
COMPARATION OF MECHANICAL PROPERTIES.

Material	Flexural (MPa)	Impact (J)	Compostable
Bagasse plate	3-5	1,5-1,9	Yes
PP (disposable)	12-25	2-3,5	No
PS (disposable)	40-60	1-2	No

L. Novelty and Environmental Contribution

The proposed material provides compostability and a low-impact production process compared to petrochemical plastics. Although it shows somewhat lower mechanical strength, its rapid degradation under composting conditions makes it suitable for single-use objects. Future improvements may include hydrophobic coatings and reinforcing additives to increase stiffness without sacrificing biodegradability. Thus, the plate meets the goals of reducing pollution and making use of agroindustrial residues —a key advantage for fostering a circular economy in packaging and tableware.

M. Impact Analysis of the Biodegradable Material

The impact test results indicate that the biodegradable material with the highest maximum impact resistance was the sample composed of 20 g of sugarcane bagasse, 35 g of potato starch, and 33 ml of water. Additionally, this sample exhibited the best characteristics in the first plate design, as shown in Table V.

TABLE V
IMPACT TEST RESULTS FOR THE COMPOSITION OF 20 G OF SUGARCANE BAGASSE, 35G OF POTATO STARCH, AND 33 ML OF WATER

Mean Failure Height (mm)	**Dart Mass (kg)**	**Mass Increment (kg)**	**Mass Increment (J)**
150	0,231	0,88	1,63

The prototype of the plate obtained using sugarcane bagasse can be seen in Fig. 10.

Fig. 10. Prototype of a plate made from sugarcane bagasse.

IV. CONCLUSION

In alignment with the initial objective of developing a biodegradable plate from sugarcane bagasse, this study successfully optimized both material composition (20 g of bagasse, 35 g of potato starch, and 33 mL of water) and process conditions (110 °C and 8 bars), resulting in plates with superior structural integrity and minimal defects. Mechanical testing based on ASTM D5628 and ASTM D7264 standards demonstrated that these specimens exhibited adequate strength, confirming the potential of sugarcane bagasse as an effective raw material for biodegradable product manufacturing.

By achieving mechanical properties suitable for single-use items, the research addresses the urgent need for sustainable alternatives in the disposable plastics industry. Furthermore, the transient thermal analyses highlighted the importance of uniform temperature profiles in both punch and cavity, reinforcing the controlled parameters (temperature, pressure, and pressing cycles) as critical factors for minimizing defects and ensuring consistent formation of sugarcane bagasse fibers with starch matrices. This robust manufacturing approach meets another key objective: enhancing the feasibility of large-scale production of biodegradable plates while reducing the environmental impact associated with conventional plastics.

Lastly, the feasibility of utilizing sugarcane bagasse —an abundant agricultural byproduct— for environmentally friendly processes has been clearly established. Consequently, this study not only delivers practical guidelines for optimizing process parameters, but also strengthens the foundation for further research on long-term biodegradation, automated systems, and scaling-up trials. In doing so, it lays out a realistic pathway toward replacing disposable plastics with biodegradable solutions, thus fulfilling the overarching goal of fostering sustainability and reducing plastic pollution.

VI .ACKNOWLEDGMENT

The authors express their gratitude for the availability of machinery, equipment, tools, and technical personnel at the Mechanical Engineering Laboratory of the Universidad Técnica de Ambato, where the machining, prototype manufacturing, and material testing were carried out.

REFERENCES

[1] A. Ashori, "Wood–plastic composites as promising green-composites for automotive industries!", *Bioresource Technology*, vol. 99, no. 11, pp. 4661-4667, 2008. https://doi.org/10.1016/j.biortech.2007.09.043

[2] L. Averous and N. Boquillon, "Biocomposites based on plasticized starch: Thermal and mechanical behaviours", *Polymer Degradation and Stability*, vol. 86, no. 1, pp. 95-102, 2004. https://doi.org/10.1016/j.carbpol.2003.11.015

[3] R. Geyer, J. R. Jambeck and K. L. Law, "Production, use, and fate of all plastics ever made", *Science Advances*, vol. 3, no. 7, e1700782, 2017. https://doi.org/10.1126/sciadv.1700782

[4] D. Gunning, C. Hills and G. Leeke, "Natural fibre composites: a review", *Journal of Cleaner Production*, vol. 204, pp. 194-215, 2018. https://doi.org/10.1016/j.jclepro.2018.06.305

[5] INEC, *Principales Resultados de la Encuesta de Superficie y Producción Agropecuaria Continua (ESPAC) 2024*, Quito, Ecuador: Instituto Nacional de Estadística y Censos, 2023.

[6] A. Kaushik, V. K. Thakur and R. K. Gupta, "Starch-based biodegradable polymers: Present status and applications", *Food Chemistry*, vol. 120, no. 3, pp. 804-812, 2010. https://doi.org/10.1016/j.foodchem.2009.08.021

[7] A. Mendes, D. Salgado, J. Oliveira and C. Martins, "Biodegradable plates from sugarcane bagasse: a solution to the environmental impact of disposable plastics", *Carbohydrate Polymers*, vol. 265, p. 117840, 2021, https://doi.org/10.1016/j.carbpol.2021.117840

[8] N. Reddy and Y. Yang, "Biofibers from agricultural byproducts for industrial applications", *Trends in Biotechnology*, vol. 23, no. 1, pp. 22-27, 2005. https://doi.org/10.1016/j.tibtech.2004.11.002

[9] V. K. Thakur, M. K. Thakur, P. Raghavan and M. R. Kessler, "Progress in green polymer composites from lignin for multifunctional applications: A review", *Industrial Crops and Products*, vol. 41, pp. 304-317, 2012. https://doi.org/10.1016/j.indcrop.2012.05.019

[10] R. Yadav, M. Misra, A. K. Mohanty and S. Parija, "Characterization and analysis of mechanical properties of biocomposites prepared from sugarcane bagasse fibers and polypropylene", *Materials and Design*, vol. 29, no. 10, pp. 1928-1937, 2008.

[11] MatWeb, "Aluminum 7075-T6; 7075-T651," [Online]. Available: https://www.matweb.com/search/datasheet.aspx?atGUID=4f19a42be94546b686bbf43f79c51b7d. [Accessed: Dec. 15, 2023].

[12] B. M. Guaman Cando, "Prototipo de plato biodegradable a partir de bagazo de caña de azúcar: Evaluación de la formación y propiedades mecánicas", *Tesis de Ingeniería Mecánica*, Universidad Técnica de Ambato, 2024.

[13] M. Cajahuaman and L. Huaranga, "Evaluación de la resistencia tensil de un plástico biodegradable obtenido a partir de almidón de papa (Solanum tuberosum)", Universidad Nacional del Centro del Peru, Huancayo, 2020. [Accessed: Nov. 23, 2023]. [Online]. Available: http://repositorio.uncp.edu.pe/handle/20.500.12894/6327 [89].

[14] F. Barreiro and A. Coronel, "Bagazo de caña de azúcar (Saccharum officinarum) y almidón de yuca (Mianihot esculenta) como sustituto de poliestireno en la elaboración de platos biodegradables", Proyecto de investigación, Escuela Superior Politécnica Agropecuaria de Manabí, Calceta, 2021. [Accessed: Jan. 20 2024]. [Online]. Available: http://repositorio.espam.edu.ec/handle/42000/1402

[15] F. Forero, D. Santana and H. Piracun, "Diseño de máquina termoformadora didáctica para el laboratorio de materiales de ingeniería de la Universidad Distrital Francisco José de Caldas", Universidad Distrital Francisco José de Caldas, Bogotá, 2018. [Accessed: Oct. 22, 2023]. [Online]. Available: https://repository.udistrital.edu.co/handle/11349/13586

[16] E. Briones y J. De la Cruz, "Diseño y construcción de un troquel para elaborar platos a base de hojas de banano", Escuela Superior Politécnica del Litoral, Guayaquil, 2019. [Accessed: Sept. 29, 2023]. [Online]. Available: http://www.dspace.espol.edu.ec/handle/123456789/52851

[17] Asociación Española de Normalización, "UNE-EN 13432:2001 Envases y embalajes. Requisitos de los envases y embalajes valorizables mediante compostaje y biodegradación". [Accessed: Sept. 27, 2023]. [Online]. Available: https://www.une.org/encuentra-tu-norma/busca-tunorma/norma?c=N0024465

[18] American Society for Testing and Materials, "D7264/D7264M Standard Test Method for Flexural Properties of Polymer Matrix Composite Materials". [Accessed: Nov. 20, 2023]. [Online]. Available: https://www.astm.org/d7264_d7264m-21.html

[19] Asociación Española de Normalización, "UNE-EN 1186-1:2002 Materiales y artículos en contacto con productos alimenticios". [Accessed: Nov. 20, 2023. [Online]. Available: https://www.une.org/encuentratu-norma/busca-tu-norma/norma?c=N0027893

[20] V|lex, "Resoluciones. 17 415 Nte INEN-EN 1672-2 (maquinaria para procesado de alimentos. Conceptos Básicos. Parte 2: Requisitos de higiene (en 1672- 2:2006+a1:2009, Idt))", V|lex. [Accessed: Nov. 19, 2023. [Online]. Available: https://vlex.ec/vid/17-415-nte-inen-693614005

[21] Asociación Española de Normalización, "UNE-EN 1672-2:2020 (Ratificada) Maquinaria para procesado de alimentos". [Accessed: Nov. 19, 2023]. [Online]. Available: https://www.une.org/encuentra-tu-norma/busca-tu-norma/norma?c=N0065067

[22] V. Reyes, J. Gonzabay, G. Herrera and C. Deza, "Determining factors of sustainability in a sugarcane company in Ecuador", *Rev Cienc Soc,* vol. 28, pp. 288-302, 2022. [Accessed: Sept. 27, 2023]. [Online]. Available: https://www.redalyc.org/journal/280/28069961021/html/

[23] D. Bermeo and P. Reyes, "Evaluación del residuo corte de caña de azúcar como materia prima para producir biocombustibles sólidos", Universidad de Guayaquil, Guayaquil, 2023. [Accessed: Sept. 16, 2023]. [Online]. Available: http://repositorio.ug.edu.ec/handle/redug/67222

[24] G. Cornejo, E. Marinero, C. Funes and P. Toruño, "Biopolímeros para uso agroindustrial: Alternativa sostenible para la elaboración de una película de almidón termo plástico biodegradable", *Revista Iberoamericana de Bioeconomía y Cambio Climático*, vol. 6, núm. 11, pp. 1359-1382, jul. 2020. https://doi.org/10.5377/RIBCC.V6I11.982

[25] Instituto Ecuatoriano de Estadísticas y Censos, "Encuesta de Superficie y Producción Agropecuaria Continua-2020". [Accessed: Sept. 14, 2023]. [Online]. Available: https://www.ecuadorencifras.gob.ec/encuestade-superficie-y-produccion-agropecuaria-continua-2020/

[26] G. Salgado, "Valorización energética de residuos agrícolas: cáscara de plátano, cascarilla de arroz y bagazo de caña mediante procesos de biodigestión y combustión", Escuela Politécnica Nacional, Quito, 2020. [Accessed: Sept. 15, 2023]. [Online]. Available: http://bibdigital.epn.edu.ec/handle/15000/20707

[27] C. Borrowman, P. Johnston, R. Adhikari, K. Saito and A. Patti, "Environmental degradation and efficacy of a sprayable, biodegradable polymeric mulch", *Polym Degrad Stab*, vol. 175, p. 109126, may 2020. https://doi.org/10.1016/J.POLYMDEGRADSTAB.2020.109126

[28] J. Posada y E. Montes, "Revisión: materiales poliméricos biodegradables y su aplicación en diferentes sectores industriales", *Informador técnico,* vol. 86, núm. 1, pp. 94-110, 2022. https://doi.org/10.23850/22565035.3417

[29] V. Tashiguano, "Revisión de literatura y propuesta de un laboratorio de innovación y desarrollo de materiales biodegradables en la Escuela Agrícola Panamericana Zamorano", Escuela Agrícola Panamericana Zamorano, Zamorano, 2020. [Accessed: Sept. 18, 2023]. [Online]. Available: https://bdigital.zamorano.edu/handle/11036/6936

[30] A. Sánchez, T. Vayas, F. Mayorga, y C. Freire, "Sector azucarero del Ecuador", Observatorio Económico y Social de Tungurahua, 2018, [Accessed: Sept. 27, 2023]. [Online]. Available: https://fca.uta.edu.ec/v4.0/images/OBSERVATORIO/dipticos/Diptico_N39.pdf

[31] J. Gil, L. Sánchez, S. Ortega, A. Grisales and M. Pinzón, "Recipientes biodegradables tipo bandeja o plato, elaborados a partir de residuos de plátano", *Investigaciones Universidad de Quindío*, vol. 34, núm. 1, pp. 263-267, 2022.

[32] American Society for Testing and Materials, "D5628 Standard Test Method for impact resistance of flat, rigid plastic specimens by means of a falling dart (Tup or Falling Mass)". [Accessed: Nov. 20, 2023]. [Online]. Available: https://www.astm.org/d5628-10.html

[33] A. Mendoza, M. Torres and P. Paredes, "Biocompuestos a partir de bagazo de caña y almidón de papa: caracterización mecánica y térmica," *Revista Iberoamericana de Polímeros,* vol. 18, pp. 55–63, 2021.

[34] F. López, J. Villacrés and C. Vaca, "Estudio comparativo de platos biodegradables basados en fibras de bagazo de caña," *Ingeniería y Desarrollo Sostenible*, vol. 25, no. 2, pp. 112-120, 2022.

[35] B. M. Guamán Cando (2024). "Diseño y construcción de un molde para la elaboración de platos desechables a partir de material biodegradable de bagazo de caña de azúcar". Facultad de Ingeniería Civil y Mecánica, Universidad Técnica de Ambato.

[36] M. A. Mansor, S. H. Salleh, N. Ismail, M. N. M. Warikh and M. T. H. Sultan, "Mechanical properties of natural fiber reinforced bagasse–starch biocomposites: A review," *Polymers*, vol. 14, no. 3, Art. no. 587, Feb. 2022. https://doi.org/10.3390/polym14030587

[37] S. O. Adekomaya and S. A. Adama, "Mechanical, thermal and morphological behavior of sugarcane bagasse composites: A review," *Heliyon*, vol. 8, no. 10, Art. no. e11192, Oct. 2022. https://doi.org/10.1016/j.heliyon.2022.e11192

[38] B. Mousavi *et al*., "Ecofriendly sugarcane bagasse-based composites for sustainable packaging," *Sustainability*, vol. 13, no. 5, Art. no. 2651, Mar. 2021. https://doi.org/10.3390/su13052651

[39] M. O. Pimentel *et al.,* "Biodegradation and mechanical performance of sugarcane bagasse/PLA composites under composting conditions," *Materials*, vol. 14, no. 2, Art. no. 273, Jan. 2021. https://doi.org/10.3390/ma14020273

[40] N. Rajabi *et al*., "Life cycle assessment and environmental implications of bagasse-based biodegradable products," *Sustainability*, vol. 14, no. 18, Art. no. 11223, Sept. 2022. https://doi.org/10.3390/su141811223

[41] A. Rojas, K. Del-Valle, V. López and P. Jiménez, "Influence of surface modifications in sugarcane bagasse for enhancing water resistance in starch-based bioplastics," *Polymers,* vol. 15, no. 1, Art. no. 148, Jan. 2023. https://doi.org/10.3390/polym15010148

[42] L. Yu *et al*., "Improvement of mechanical properties for bagasse-based composites using a novel pre-treatment," *Scientific Reports*, vol. 11, Art. no. 20912, Nov. 2021. https://doi.org/10.1038/s41598-021-00216-3

ENFOQUE UTE REVISTA
Facultad Ciencias de la Ingeniería e Industrias
RESEARCH ARTICLE
ENFOQUE UTE, VOL. 16, NO. 3, pp. 25-36, E-ISSN: 1390-6542
RECEIVED APRIL 16, 2025; ACCEPTED JUNE 2, 2025; PUBLISHED ONLINE JULY 1, 2025;
DATA OF CURRENT VERSION JULY 1, 2025; PUBLISHED IN VOLUME 16, ISSUE 3 (JULY 2025).

Optimized Fairing Development for Electric Motorcycle Using CFD Simulation and Finite Element Analysis (FEA)

Martínez-Reategui Cristian H.[1*], León-Japa Rogelio S.[2], Jurado Francisco[3]

Abstract — **The growth of urbanization has generated an increase in the use of motorized transport, which has intensified problems such as road congestion, environmental impact and health and safety risks. Currently, the automotive field is responsible for more than 10 % of global greenhouse gas (GHG) emissions. In response to this problem, manufacturers have developed several solutions, with electric vehicles playing the leading role as a sustainable alternative. Electric motorcycles have shown a growth in sales in recent years in Ecuador; however, their growth is limited by factors such as lack of infrastructure and government regulations. Manufacturers focus on aerodynamics as a key aspect to improve efficiency; to optimize their design, tools such as wind tunnels or computational simulations are used, the latter being a more accessible option. This study proposes the design of a fairing for an electric motorcycle using CAD/CAE software, based on the IDes process. Three proposals were developed, evaluating their aerodynamic performance under the conditions of Loja province. The results indicated that design 3 obtained the best performance, with an average drag coefficient of 0.283 and a lift coefficient of -0.273, subjected to different speeds. From the structural point of view, epoxy resin with unidirectional prepreg S-glass fiber was selected for its balance between mechanical properties and cost. The simulation showed a maximum deformation of 0.35339 mm under various stresses. Furthermore, in the modal analysis, at 78.802 Hz, the fairing presented a deformation of 15.788 mm with a maximum amplitude of 6.5 Hz, validating its ability to withstand the dynamic conditions of the motorcycle without compromising its structure.**

Keywords: **Electric motorcycle; Finite element; Computational fluid dynamics (CFD); Drag coefficient; Lift coefficient; Structure.**

Resumen — **El crecimiento de la urbanización ha generado un aumento en el uso de transporte motorizado, lo que ha intensificado problemas como la congestión vial, el impacto ambiental y riesgo en la salud y seguridad. Actualmente, el campo automotriz es responsable de más del 10 % de las emisiones globales de gases de efecto invernadero (GEI). Como respuesta a esta problemática, los fabricantes han desarrollado diversas soluciones, teniendo el papel principal los vehículos eléctricos como una alternativa sostenible. Las motocicletas eléctricas han mostrado un crecimiento en ventas en los últimos años en Ecuador; sin embargo, su crecimiento se ve limitado por factores como la falta de infraestructura y regulaciones gubernamentales. Los fabricantes se enfocan en la aerodinámica como un aspecto clave para mejorar la eficiencia, para optimizar su diseño, se emplean herramientas como túneles de viento o simulaciones computacionales, siendo este último una opción más accesible. Este estudio propone el diseño de una carenado para una motocicleta eléctrica utilizando software CAD/CAE como el SolidWorks para el diseño y el Ansys workbench para la simulación, basado en el proceso IDEs. Se desarrolló tres propuestas, evaluando su desempeño aerodinámico bajo las condiciones de la provincia de Loja. Los resultados indicaron que el diseño 3 obtuvo el mejor desempeño, con un coeficiente de arrastre promedio de 0.283 y una fuerza de sustentación de -0.273, sometido a distintas velocidades. Desde el punto de vista estructural, se seleccionó la resina epoxi con fibra de vidrio S preimpregnado unidireccional, por su equilibrio entre propiedades mecánicas y costo. La simulación determinó una deformación máxima de 0.35339 mm bajo diversos esfuerzos. Además, en el análisis modal, se halló 78.802 Hz, el carenado presentó una deformación de 15.788 mm con una amplitud máxima de 6.5 Hz, validando su capacidad para soportar las condiciones dinámicas de la motocicleta sin comprometer su estructura.**

Palabras Clave: **Motocicleta eléctrica; Elementos finitos; Dinámica de fluido computacional (CFD); Coeficiente de arrastre; Coeficiente de sustentación; Estructura.**

* *Corresponding autor:* cristian.martinez@unl.edu.ec

1. Ing. Martínez Reategui Cristian Humberto, Facultad de Energía, Industrias y Recursos Naturales No Renovables, Universidad Nacional de Loja, Loja, Ecuador. E-mail: cristian.martinez@unl.edu.ec, ORCID number https://orcid.org/0009-0000-8639-9662
2. Ing. León Japa Rogelio Santiago Mg. Sc., Facultad de Energía, Industrias y Recursos Naturales No Renovables, Universidad Nacional de Loja, Loja, Ecuador. E-mail: rogelio.leon@unl.edu.ec. ORCID number https://orcid.org/0000-0003-2142-3769
3. Ing. Jurado Francisco Ph.D., Departamento de Ingeniería Eléctrica, Universidad de Jaén, Jaén, España. E-mail: fjurado@ujaen.es. ORCID number https://orcid.org/0000-0001-8122-7415.

DOI: https://doi.org/10.29019/enfoqueute.1173
Associate Editor: *Víctor Suntaxi*

I. INTRODUCTION

THE growth of urbanization and the increase in motorization have posed significant challenges related to congestion, the environment, health, and safety [1]. In this context, electric vehicles have emerged as a key solution for more sustainable mobility, by reducing the impact of urban transportation on air quality, road traffic, and equitable access to transportation [2]. This is especially relevant, considering that the automotive sector is responsible for more than 10 % of global greenhouse gas (GHG) emissions and is one of the largest consumers of oil worldwide [3].

In vehicle design, aerodynamics plays a crucial role as it directly influences energy efficiency, performance, and safety. The use of numerical tools such as computational fluid dynamics (CFD) complements traditional wind tunnel testing [4], enabling the optimization of drag coefficient and aerodynamic load. These improvements positively impact maneuverability, structural stress, and energy consumption [5].

In Ecuador, despite the commercial growth of electric motorcycles—with a 5.4 % increase in sales compared to 2021 and a 37.2 % increase compared to 2019 [6]—challenges related to geography and limited range still persist. Manufacturers have developed solutions such as higher-capacity batteries and regenerative braking systems, but have also turned to less efficient alternatives like the incorporation of trailers [7]. Additionally, the lack of specific regulations has led to operational issues with electric motorcycles, prompting the Ecuadorian Transit Commission (CTE) to announce regulations to govern their use [8].

The objective of this research is to design a fairing prototype for an electric motorcycle using computer-aided engineering (CAE) tools. Based on an existing chassis structure, the project aims to develop a design that integrates aerodynamic and structural parameters, optimizing performance through specialized software such as SolidWorks for CAD modeling and Ansys for aerodynamic simulations. Various proposals will be evaluated to select the most efficient design.

The methodology combines the IDeS approach (Industrial Design Structure) with Stylistic Design Engineering (SDE), integrating aesthetic and functional principles [9]. This enables the development of preliminary designs tailored to local needs and the comparison of alternatives to identify the best option in terms of energy efficiency and structural performance.

A recent study analyzes the charging infrastructure for electric vehicles along the Cuenca-Loja route, identifying fourteen optimal locations for charging stations [10]. In line with this finding, this project proposes a conceptual fairing design that optimizes energy consumption, reduces reliance on charging stations, and minimizes implementation costs by maximizing the aerodynamic and structural properties of the fairing.

The optimized fairing design for the electric motorcycle, developed at the Universidad Nacional de Loja (UNL), emerges as a comprehensive response to the challenges of energy efficiency and limited range faced by these vehicles, particularly in Ecuador's geographic and urban context. Considering the country's topographical conditions and the growing demand for sustainable mobility solutions, the project focuses on reducing aerodynamic drag through a design adapted to the local environment. This initiative not only significantly enhances the vehicle's performance and range but also contributes meaningfully to national technological innovation, promoting the adoption of electromobility as a viable, accessible, and environmentally responsible alternative.

II. METHODOLOGY

A. Specific Fairing Requirements

The MotoStudent regulations specify the design and accessory requirements for the fairing. All edges must be rounded with a minimum radius of approximately 1 mm. This measure not only aims to prevent cuts when handling the fairing—whether during removal or installation—but also to protect the rider from potential injuries in case of an accident. These specifications ensure that the design is safe for both daily use and unforeseen situations, prioritizing ergonomics and user safety [11].

The minimum and maximum dimensions of the motorcycle must comply with certain parameters. The minimum distance between the ends of the clip-on handlebars must be approximately 450 mm. Additionally, the motorcycle must allow a minimum lean angle of 50° without any part touching the ground. The seat must have a width of 450 mm and must not exceed a maximum width of approximately 600 mm at the front. On the other hand, the ground clearance in an upright position must be at least 100 mm when the motorcycle is stationary. Finally, the maximum permitted height from the seat to the highest part of the tail section will be approximately 150 mm. All of these parameters are better illustrated in Figure 1. [12]

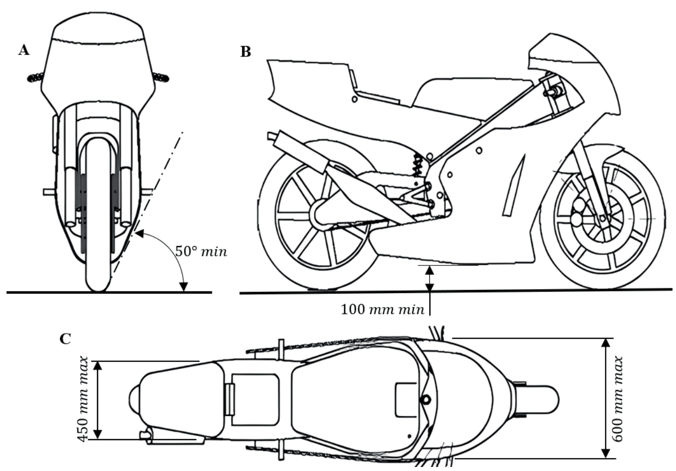

Fig. 1. Motorcycle design parameters.

B. Fairing Sketch Design

A market study was conducted on different types of urban designs with the aim of identifying various detail lines in correlation with the IDeS methodology [9]. As part of the initial stage of the manufacturing process, hand-drawn sketches were developed to select the most suitable design [13] (see Figure 2). This process considered elements that cannot be modified, based on previous studies of the frame and its dynamics. Additionally, existing auxiliary components were evaluated, such as the front headlight, which features an external round-shaped design concept.

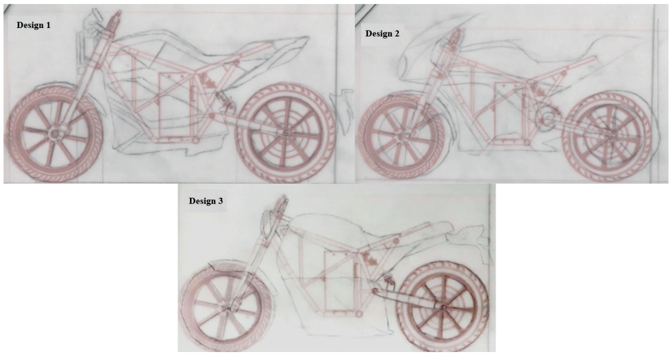

Fig. 2. Most suitable final designs with easy adaptability for modification.

C. CAD Designs of the Fairing Models

Using SolidWorks software, detailed conceptual designs were developed with the use of surface modeling tools, as shown in Figure 3. In the development of complex parts, this process is essential. The modeling process varies greatly from person to person, as there is no strictly right or wrong way to model—some approaches involve more operations, while others use fewer. However, fewer operations do not always mean a better model, as this can affect the flexibility for making design changes if needed [14].

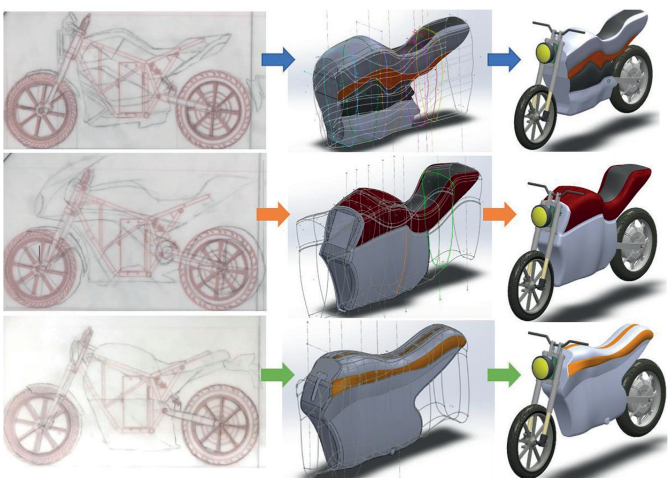

Fig. 3. Modeling of the highlighted designs.

D. Aerodynamic Analysis of the Fairing Using CFD

The aerodynamic analysis is carried out using Ansys' CFD simulation library within the Fluid Flow (CFX) module. As a first step, a Boolean operation is created to generate a cavity by subtracting the target body from the general body in order to remove the intersection zone, as shown in Figure 4.

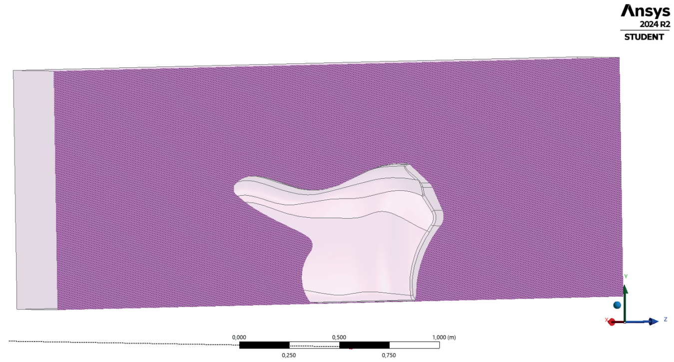

Fig. 4. Fairing removal from the control volume.

As for external parameters, the average temperature in the city of Loja—where the electric motorcycle will operate—is approximately 24°C. This value is also used to estimate air density based on the standards defined in ISO 2533:1975, as shown in Equation 1 [15].

$$\rho = \frac{m_{\mathrm{air}} {}^{*} P_{\mathrm{atm}}}{R^{*}T}$$
$$\rho = \frac{0.02896351244^{*}101220}{8.314472^{*}(24+273.15)} \tag{1}$$
$$\rho = 1.187\ \frac{\mathrm{kg}}{\mathrm{m}^3}$$

Where P_{atm} represents the atmospheric pressure in the city of Loja in $[Pa]$, R is the universal gas constant with a value of 8.314472 in $[\mathrm{Pa}^{*}m^3/\mathrm{mol}^{*}K]$, m_{air} is the molar mass of dry air, equal to 0.02896351244 $[kg/mol]$, and T corresponds to the average ambient temperature in Loja expressed in $[K]$.

Meshing involves dividing the geometry of the model into small parts known as finite elements, breaking the model into more manageable pieces that facilitate computational calculation (see Figure 5).

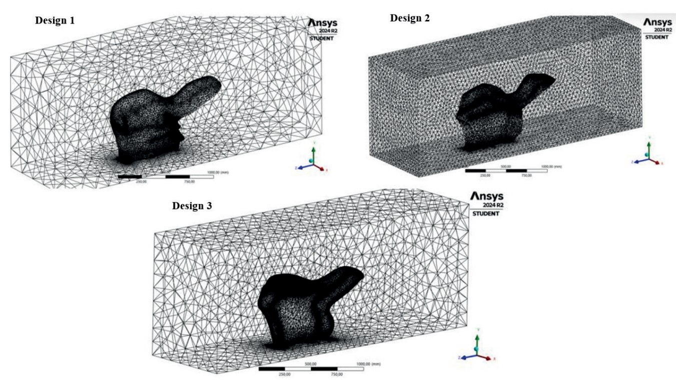

Fig. 5. Meshing of the fairing control volume

During mesh creation, it is recommended to maintain a maximum skewness ratio below 0.95 to ensure proper mesh quality [16]. According to this criterion, a skewness ratio between 0 and 0.25 is considered excellent; between 0.25 and 0.50, very good; from 0.50 to 0.80, good; from 0.80 to 0.94, acceptable; from 0.95 to 0.97, poor; and between 0.98 and 1.00, unacceptable [17]. These mesh quality ranges are detailed more clearly in Table I.

Orthogonal quality is another parameter that measures mesh quality. The minimum acceptable orthogonal quality index is below 0.1 [16]. In this case, the model meets the requirement with a minimum index of 0.17. Additionally, values between 0.95 and 1.00 are considered perfect mesh quality [17], as shown in Table I.

TABLE I
STANDARD VALUES FOR MESH QUALITY PARAMETERS REGARDING ASPECT RATIO AND SKEWNESS

Parameters	**Standard Values**						
Aspect Ratio	**0.2 – 0.5 Equilateral**	**Excellent**	**Very Good**	**Good**	**Acceptable**	**Poor**	**Unacceptable**
Skewness	0	0 – 0.25	0.25 - 0.50	0.50 - 0.75	0.75 - 0.90	0.90 - < 1	1
Orthogonal Quality	-	0.95 – 1	0.70 - 0.95	0.20 - 0.69	0.10 - 0.20	0.001 - 0.10	0 - 0.001

Turbulence models are essential numerical tools that allow the linkage of average fluctuations with mean values of variables, thus facilitating the resolution of equations that describe turbulent fluid behavior. These models are widely applied in CFD analysis programs and include a variety of approaches such as $K-\varepsilon, K-\omega, Sparlat Allmaras, Low-RE\ K-\varepsilon$ algebraic, SST, and $L-VEL$ [18].

The $K-\varepsilon$ model is preferred due to its specific advantages in aerodynamic and turbomachinery simulations [19] [20]. The model is known for its accuracy in calculating flows near solid surfaces and its adaptability to a wide range of flow conditions. Its selection is also based on the computational limitations imposed by the student license of Ansys, which restricts the number of nodes and elements used in CFD analysis [16].

E. Material Selection Method

The most suitable material for the construction of the fairing is considered to be composite materials due to their numerous advantages and properties. These materials are widely used in the transportation industry thanks to their combination of lightness, stiffness, and high impact resistance. Additionally, they stand out for their durability, offering excellent resistance to corrosion and wear, making them an ideal option for demanding applications [21].

An optimal material selection should be based on the evaluation of essential properties, among which tensile strength and economic feasibility of the material are highlighted, ensuring that its acquisition cost is affordable. Furthermore, it is important to consider the manufacturing process, as some composite materials present complexities that require highly skilled personnel for proper handling and the production of special parts, such as auto parts [22].

The fairing fulfills a crucial function, as it optimizes the aerodynamics of the assembly. The main objectives of the selection were to reduce the total weight of the fairing, which initially was 4.32 kg, while ensuring that the structural strength was not compromised. Key constraints that the material had to meet were established, such as impact and vibration resistance, corrosion and fatigue resistance, as well as ease of manufacturing and a reasonable cost. Within the selection process, the fiber type, polymer matrix, fiber orientation, and fiber content in the composite structure were defined as free variables.

The performance index table provided by the CES Edupack software was used, a tool that allows comparison and classification of materials according to their mechanical and physical properties. To create the Ashby diagram, a key constraint was applied that requires a minimum strength with the lowest possible mass, aiming to reduce the initial weight of the fairing without compromising its structural integrity. To select the optimal materials for manufacturing the fairing, an analysis was carried out based on the relationship between acquisition cost and mechanical strength. The goal was to identify materials that offered a balance between high structural performance, low cost, and ease of manufacturing, as illustrated in Figure 6.

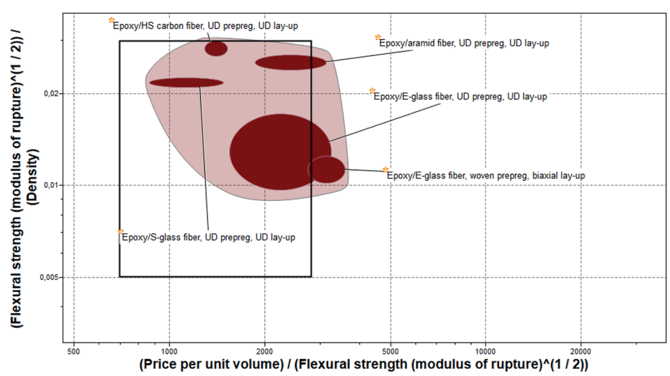

Fig. 6. Results of selected materials in CES Edupack Software.

Two evaluation methods were used for the material selection. The first is based on a decision matrix, in which the obtained values are normalized using the most relevant results as a reference. Then, a weighting is assigned to each result based on the total value of each evaluated criterion on a scale from 1 to 10. Finally, a summation is performed to determine the material with the best performance, considering cost optimization and the maximization of mechanical properties.

The second evaluation method used is the Analytical Hierarchy Process (AHP), a methodology that facilitates the selection of alternatives through the comparison of a series of criteria or variables organized in a hierarchical structure. In this approach, the top level represents the main objective, while the criteria and sub-criteria are distributed across lower levels. Since these criteria often conflict, AHP allows priorities to be established and the best option to be determined. This method is based on the use of a pairwise comparison scale [23]. This approach is especially effective due to the human brain's natural ability to evaluate and compare two criteria or alternatives at a time, thus facilitating decision-making. However, when it is necessary to compare multiple options simultaneously, the complexity of the analysis increases considerably, which can generate uncertainty and hinder optimal choice [23].

The use of Expert Choice software requires entering detailed descriptions of each criterion and sub-criterion of analysis, as shown in Figure 7. This is essential for properly structuring the decision model, as it allows organizing and prioritizing the determining factors in the selection of the most suitable material.

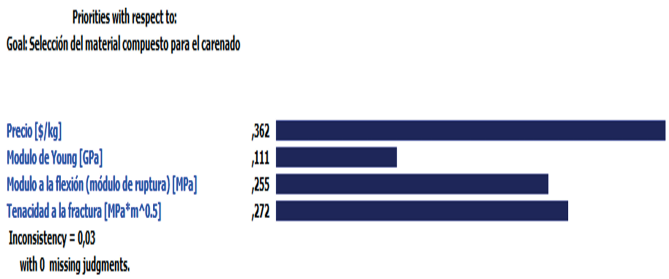

Fig. 7. Valuation criteria for material selection.

F. Structural Method for Fairing Analysis

The structural simulation begins with the preparation of the CAD designs generated in SolidWorks for analysis in Ansys, using the Workbench module. A compatible format is used to allow a smooth transition between both software environments. Subsequently, solid elements were converted into surface sheets using the SpaceClaim interface.

For meshing, a methodology based on mesh convergence was employed, which consists of identifying the optimal mesh resolution to ensure accurate and reliable results in simulations. This directly affects the number of vertices, as it controls both the expansion and the allowed element size in critical regions, establishing a resolution from 0.02 to 5 % [24]. The convergence rate (Tc) is equal to the difference between the latest and previous stress results, divided by the previous stress result, as described in Equation 2:

$$T_c = \frac{\text{Last}_{Result} - \text{Previous}_{result}}{\text{Previous}_{result}} * 100 \qquad (2)$$

This approach not only ensures higher accuracy in aerodynamic or structural simulations, but also optimizes computational performance by balancing the mesh density in key areas of the analysis, as demonstrated in Figure 8.

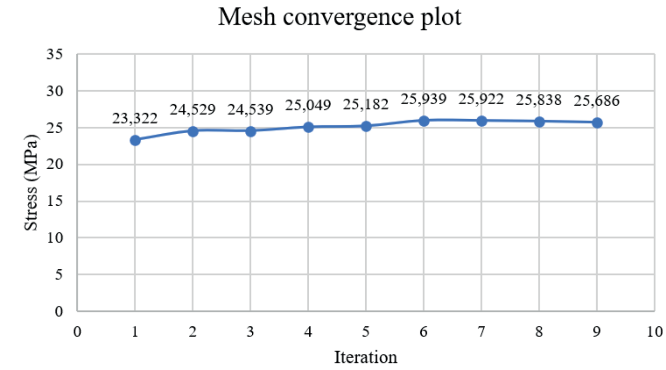

Fig. 8. Valuation criteria for material selection.

For refinement, a quadrilateral mesh was implemented to study a 2D surface-type mesh, which improved the quality of the analysis [25]. A mesh thickness of 8 mm was established, while in critical areas a refinement was applied with a reduced thickness of 5.5 mm, as illustrated in Figure 9. This adjustment was made to improve the representation of stress and strain gradients, ensuring greater fidelity in the results. The validity of this approach was verified through an iterative process, whose results are presented in Figure 8, confirming that the refinement improves convergence without oversaturating the fairing with excessive mesh density.

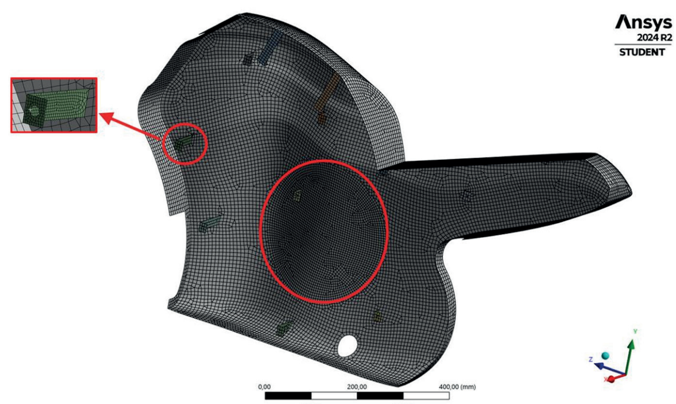

Fig. 9. Mesh refinement in the deformation zone.

The predetermined material thickness was set at 3 mm, defined based on an evaluation of its mechanical properties to ensure its capacity for impact absorption and structural resistance [18]. The design must withstand both the loads generated by the weight of the motorcycle itself, which includes the motor, controller, and battery, as well as the weight of a person, totaling 162.2 kg, in accordance with the manufacturer's manual [26]. Additionally, it must resist external forces without compromising structural integrity. In this way, the durability of the rider's fairing is ensured, even under operational conditions, as defined in Equation 3:

$$F_x = \frac{1}{2} * \rho_{aire} * A_{surf} * C_x * V^2 \qquad (3)$$

III. RESULTS AND DISCUSSION

A. Preliminary Design Results

The design process was based on the Industrial Design Structure (IDes) approach, integrating tools such as Quality Function Deployment (QFD) and Stylistic Design Engineering (SDE), which optimize efficiency in product development. Technologies such as Augmented Reality (AR) and Additive Manufacturing (AM) allow real-time visualization of the models, facilitating early detection of improvements in the fairing structure [9].

The fairing design was also adapted to the guidelines of the MotoStudent 2018 regulation, which establishes key requirements for vehicle safety and functionality. The minimum edge radius of 1 mm was respected, and designs that laterally covered the rider were avoided to minimize risks in the event of a fall. Additionally, the minimum lateral tilt angle of 50° was met, ensuring that no part of the fairing interferes with the frame. Dimensional constraints were also respected, such as a maximum width of 600 mm and a minimum ground clearance of 100 mm, resulting in designs like the one shown in Figure 10.

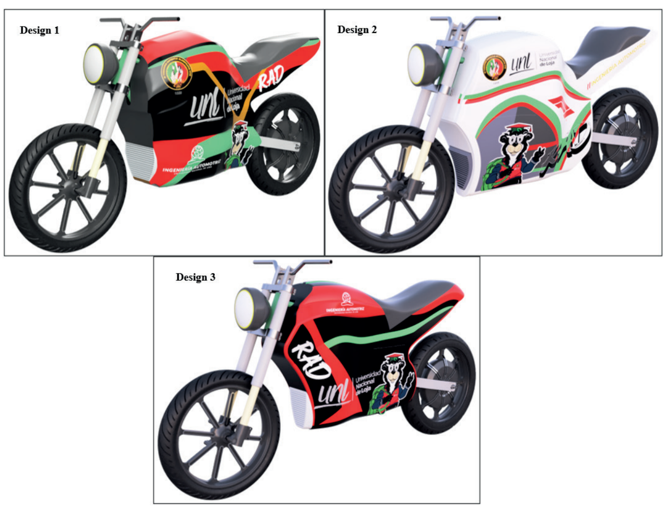

Fig. 10. Rendering of the fairing designs.

B. CFD Methodology Results

From an aerodynamic standpoint, three fairing configurations were analyzed, with drag coefficients of 0.367, 0.468, and 0.282, the latter being selected due to its better performance, as shown in Table II. In other studies, where coefficients range between 0.5915 and 0.7629, a significant reduction in air resistance is observed [27]. Another study reports values of 0.32 and 0.36 in prototype designs for the Shell Eco Marathon competition, reinforcing the validity of the results of this research. Additionally, the obtained lift forces were -0.317, -0.11, and -0.273 [28], showing correlation with previous studies and confirming the aerodynamic stability of the design.

TABLE II
MESH RESOLUTION AND ASPECT RATIO METRICS

Aspects	Design 1	Design 2	Design 3
Nodes	81720	102392	205000
Elements	437487	548708	1115586
Frontal area (m²)	0.27	0.3	0.19
Skewness metric	0.23743	0.23265	0.23311
Orthogonal quality	0.76127	0.7661	0.76563
Fluid temperature		25°C	
Reference pressure		101220 Pa	
Turbulence model		k-epsilon	
Element type		Tetrahedral	
Minimum speed		45 km/h	
Maximum speed		150 km/h	

In Design 1, a slight pressure increase was detected on the lateral side of the fairing, especially in the area where the motorcycle seat mount is located. This behavior indicates a potential interaction point between the airflow and the fairing structure in that region. In Design 2, a pressure concentration was observed in the tail section, within a well-defined area of approximately 150 mm. In contrast, Design 3 showed a significantly different behavior. In this model, the pressures on the fairing body were considerably lower, and air fluctuations on the lateral areas remained minimal. This favorable aerodynamic behavior reduces disturbing forces on the fairing, granting it important advantages in terms of stability and aerodynamic efficiency, positioning it as a strong candidate in the optimal design selection process.

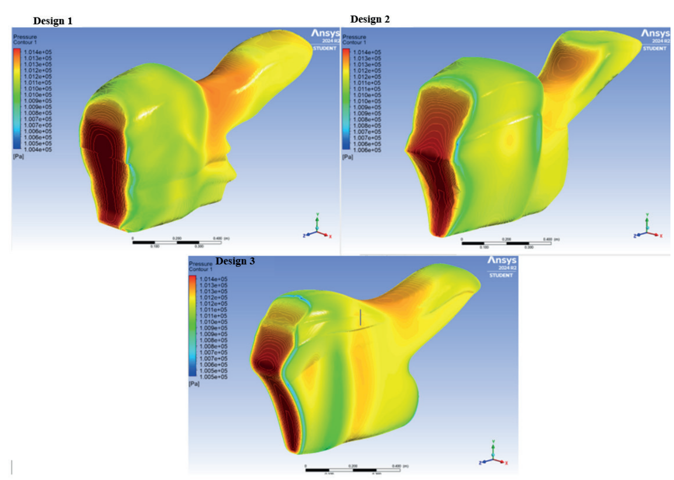

Fig. 11. Pressure map of the three fairing designs.

One of the most relevant aspects analyzed in the simulations was the airflow behavior inside the fairing, including fluctuations and effects from its interaction with ventilation grids designed to facilitate air intake and exhaust. Design 3 showed outstanding results regarding well-distributed and efficient internal airflow, with an adequate exit of hot air through the ventilation outlets. This behavior not only ensures better thermal control by maintaining optimal internal temperatures, but also minimizes internal airflow fluctuations, enhancing the aerodynamic stability of the fairing.

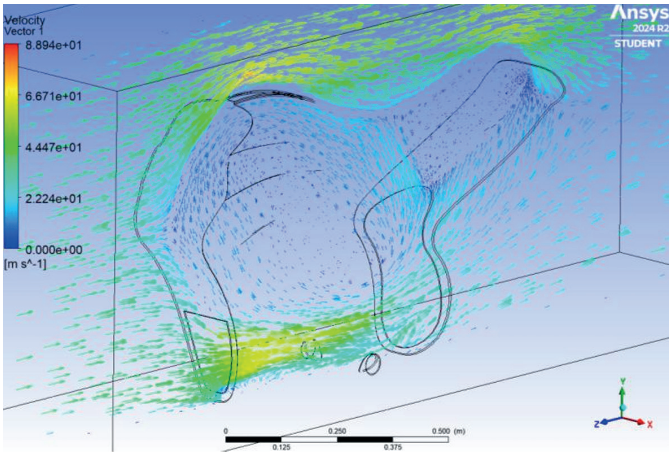

Fig. 12. Internal airflow of the fairing for Design 3.

To determine the drag and lift coefficients using Ansys software, specifically in the CFX library, the drag force value was initially obtained in order to analytically calculate the corresponding coefficients. The drag coefficient was calculated for speeds of 45, 65, and 150 km/h, starting from the drag force equation.

$$C_d = \frac{2{*}F_d}{\rho_{air}{*}A_{front}{*}V^2}$$

$$C_d = \frac{2{*}9.57701\ N}{1.187{*}\frac{\text{kg}}{m^3}{*}0.276588\ m^2{*}\left(45{*}\frac{\text{km}}{h}{*}\frac{5}{18}\right)^2\frac{m}{s}} \tag{4}$$

$$C_d = 0.374$$

For the lift coefficient, a mathematical model was applied starting from the lift force, which is the component perpendicular to the airflow acting on the fairing, considering air density, the frontal area of the fairing, and the speeds defined in the study.

$$C_l = \frac{F_l}{\frac{1}{2}{*}\rho_{air}{*}V^2{*}A_{front}}$$

$$C_l = \frac{-8.07668\ N}{\frac{1}{2}{*}1.187{*}\frac{\text{kg}}{m^3}{*}\left(45{*}\frac{\text{km}}{h}{*}\frac{5}{18}\right)^2\frac{m}{s}{*}0.276588\ m^2} \tag{5}$$

$$C_l = -0.315$$

Turbulence formation was also observed in the rear zone, specifically around the rear tire. These 2D streamlines have a direct impact on the motorcycle's aerodynamics, as their continuity promotes reduced aerodynamic drag and improved stability. The effect is more evident in Designs 1 and 2, as seen in Figure 13, where flow disturbances are more pronounced. On the other hand, Design 3 shows a significant reduction in turbulence formation, suggesting improved aerodynamic performance of the fairing and reduced drag.

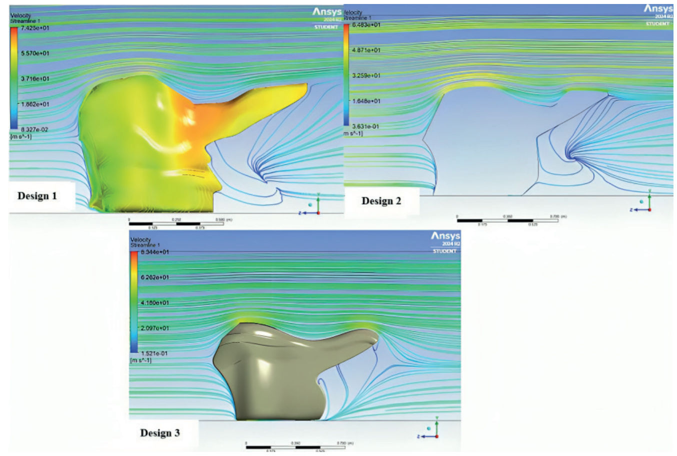

Fig. 13. Streamlines in the models.

C. Aerodynamic Boundary Layer

The boundary layer is a thin region of fluid flow, such as air, that develops parallel to solid surfaces, in this case, the fairing wall [29]. In order to minimize additional mass on the chassis and preserve the rolling efficiency of the motorcycle, the use of composite materials for its construction is foreseen. Likewise, restrictions on the use of original accessories are considered to avoid increases in manufacturing costs.

With the development of computational capabilities in recent decades, it has become possible to numerically solve the Navier-Stokes equation in flows with complex geometries. This has revolutionized fluid analysis, eliminating the need to separate the flow into outer zones and boundary layer regions, since the use of CFD now allows solving all the equations of motion throughout the entire flow field [29], as shown in Figure 14.

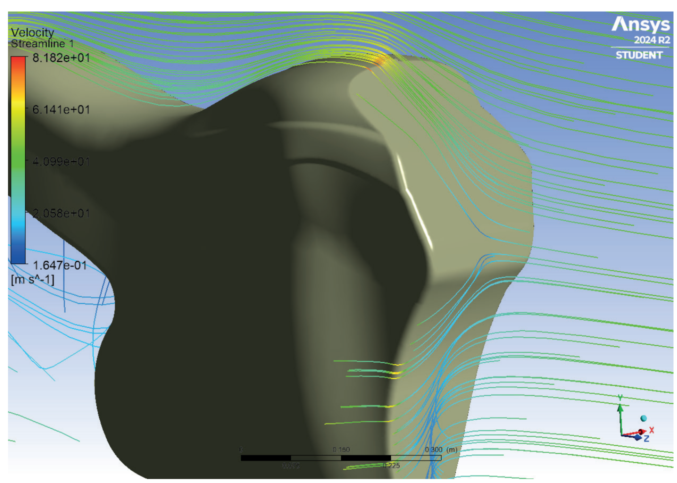

Fig. 14. Effect of the boundary layer on the fairing.

To begin the analysis, it is essential to understand the behavior of the air over the fairing. This is achieved by calculating the Reynolds number (*Re*), using equation 6. This value allows determining whether the flow is laminar or turbulent, which is key to properly approximating the boundary layer. According to established criteria, the flow is considered laminar if the Reynolds number is less than $5 * 10^5$ and turbulent if it is greater [29]. This calculation uses the different velocities at which the motorcycle will travel (V) in meters per second [m/s], the length of the fairing from the leading edge to its rear end (L) in meters [m], and the kinematic viscosity of air (v), whose average value is approximately $1.5 * 10^{-5}$ [m^2/s].

$$R_{ex} = \frac{V \cdot L}{\nu} = \frac{V_x}{\nu} \tag{6}$$

The boundary layer thickness (δ) is defined as the distance from the wall to the point where the parallel velocity reaches 99 % of the fluid velocity outside the layer. For its calculation, the formulation for turbulent flow was used, since the Reynolds number exceeded the limit for laminar flow. These values allow the use of three significant figures due to their higher precision; in turbulent regime, two significant figures were chosen due to the high characteristic uncertainty. To describe the flow properties, two approaches were considered: the one-seventh power law and a variant that incorporates empirical data for smooth surfaces [29], as described in Table III, with the latter being the option selected for the calculations.

TABLE III
COMPARISON OF LAMINAR AND TURBULENT BOUNDARY LAYER PROPERTIES

Property	Laminar	Turbulent(1)	Turbulent(2)
Boundary Layer Thickness	$\frac{\delta}{x} = \frac{4.91}{\sqrt{R_{ex}}}$	$\frac{\delta}{x} \simeq \frac{0.16}{(R_{ex})^{\frac{1}{7}}}$	$\frac{\delta}{x} \simeq \frac{0.38}{(R_{ex})^{\frac{1}{5}}}$
Displacement Thickness	$\frac{\delta^*}{x} = \frac{1.72}{\sqrt{R_{ex}}}$	$\frac{\delta^*}{x} \simeq \frac{0.020}{(R_{ex})^{\frac{1}{7}}}$	$\frac{\delta^*}{x} \simeq \frac{0.048}{(R_{ex})^{\frac{1}{5}}}$
Momentum Thickness	$\frac{\theta}{x} = \frac{0.664}{\sqrt{R_{ex}}}$	$\frac{\theta}{x} \simeq \frac{0.016}{(R_{ex})^{\frac{1}{7}}}$	$\frac{\theta}{x} \simeq \frac{0.037}{(R_{ex})^{\frac{1}{5}}}$
Local Friction Coefficient	$C_{f,x} = \frac{0.664}{\sqrt{R_{ex}}}$	$C_{f,x} \simeq \frac{0.027}{(R_{ex})^{\frac{1}{7}}}$	$C_{f,x} \simeq \frac{0.059}{(R_{ex})^{\frac{1}{5}}}$

For better understanding, the graph 15 has been created to demonstrate the theory mentioned by [29], which states that at a given position x, the higher the Reynolds number, the thinner the boundary layer will be, with everything else remaining constant, and the boundary layer approximation becomes more reliable.

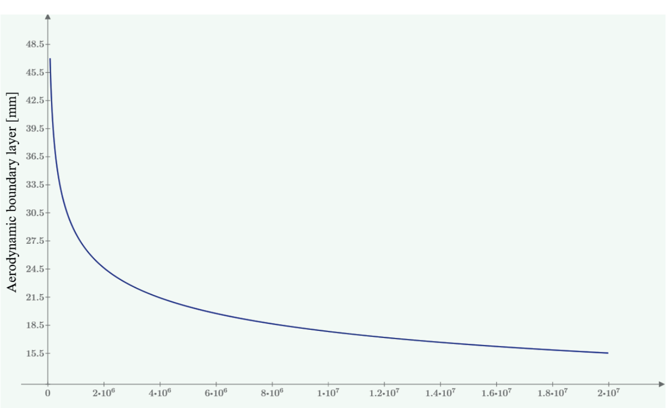

Fig. 15. Reynolds number Vs Boundary layer.

The analysis of turbulent flow around the fairing was carried out using Ansys software, selecting design 3 to evaluate the entire surface exposed to the wind tunnel. The solution converges by applying the continuity equation. The residuals of kinetic energy and turbulent dissipation, shown in figure 16, stabilize around $1.0e^{-03}$, an acceptable value that does not compromise aerodynamic drag, showing behavior similar to studies on laboratory turbomachinery [30]. This interaction helps reduce resistance on objects and reveals vortex formation [31]. Aerodynamic simulations show that controlling the flow improves vehicle efficiency [32] [33]. In motorcycles, this control also promotes more stable riding and lower energy consumption.

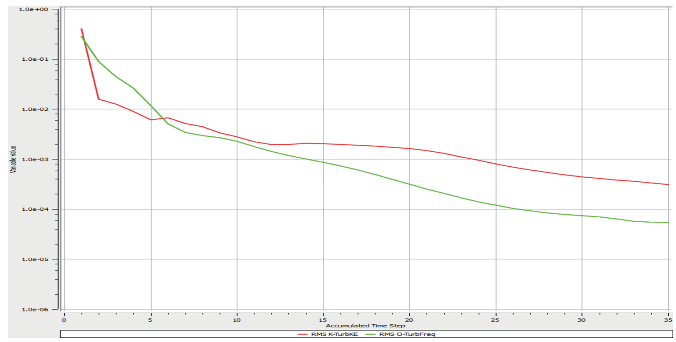

Fig. 16. Turbulent kinetic energy and dissipation.

D. Material Selection Result

The best alternative was unidirectionally pre-impregnated S-glass fiber with epoxy resin, obtaining a score of 8.22 in the weighting analysis, following a methodology similar to the one used by [34]. In addition, the selection was validated using the Expert Choice software, where this material achieved the best result with 38.7 % and an inconsistency ratio of 0.03 (see Figure 17), which correlates with the study conducted by [34].

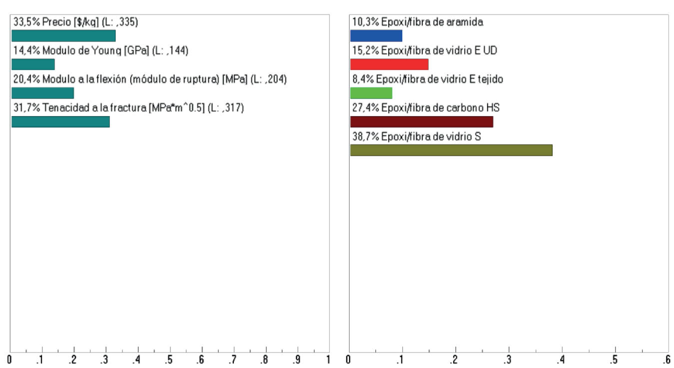

Fig. 17. Result of the most optimal material in Expert Choice.

The results obtained with the Expert Choice software confirm that epoxy/S-glass fiber is the best option due to its high selection percentage and lower cost compared to other alternatives. While carbon fiber presents better properties in terms of Young's modulus and flexural modulus, epoxy/S-glass fiber stands out for its higher fracture toughness, making it a more balanced alternative when considering both mechanical properties and economic feasibility, as shown in Figure 18. This type of methodology was used by replicating the use of similar studies such as that of [35], for the design and construction of uprights and wheel hubs of an electric Formula SAE competition vehicle, using the decision matrix methodology and implementing a validation with the AHP hierarchical method used in the study of [34] for the selection of a type of composite material according to the intended use.

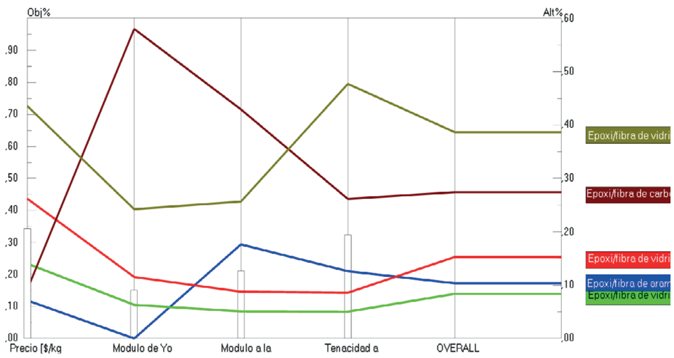

Fig. 18. Result by each criterion in Expert Choice.

E. Structural Simulation Results

The fairing was designed with a thickness of 3 mm, achieving a maximum deformation of 0.35339 mm under a load of 2100 N, which is higher than the combined weight of the motorcycle accessories. Another study reported a deformation of 8.43 mm under different loading scenarios, highlighting the greater stiffness of the fairing developed in the present work [18]. To ensure result accuracy, the mesh was adjusted within a resolution range between 0.02 and 5 % [24]. A total of 9 iterations were performed. In this process, 16,153 nodes and 16,071 elements were generated, achieving a Quality ratio of 0.98512, indicating high mesh quality, as shown in Figure 19, which ensured convergence without compromising computational efficiency.

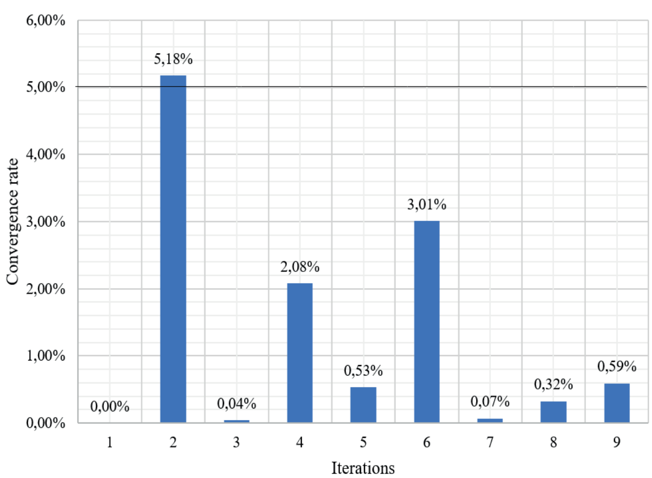

Fig. 19. Iteration diagram vs. convergence rate analysis.

Both aerodynamic forces and the total weight of the mounted accessories were considered in the event of a crash. Additionally, high forces were simulated to replicate impact conditions and analyze the material's response under extreme scenarios. Significant deformation was observed in the area where the rider's legs are positioned, along with minor deformations in other regions. However, the latter can be considered negligible, as no excessive stresses are generated in these regions under normal operating conditions.

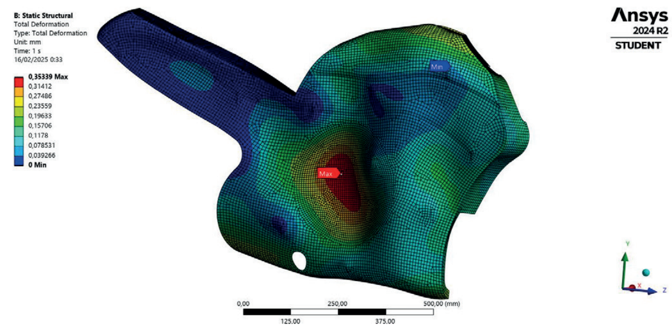

Fig. 20. Deformation zones of the fairing.

Multiple simulations were conducted to evaluate the material behavior under various loading conditions. As shown in Figure 21, the first two stress cases analyzed correspond to aerodynamic forces generated at speeds of 45 km/h and 65 km/h. Subsequently, at a speed of 150 km/h, the applied force reached 297.8620 N. From this point, predefined loads were applied to assess material deformation. The results indicate that, under a load of approximately 2100 N, the deformation factor obtained was 0.35339 mm, showing an exponential increase in deformation. This analysis helps determine the material's reliability and its ability to withstand high structural demands.

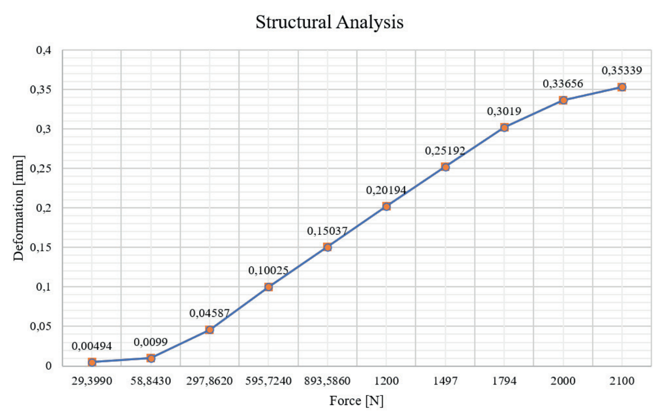

Fig. 21. Force vs. Deformation diagram.

The Von Mises criterion was used to evaluate load distribution in the fairing. As observed in Figure 22, a higher stress concentration was identified at support point B, located at the bottom of the fairing, specifically in the area where the rider places their feet. This result is consistent with the observations in Figure 22, suggesting that this area is particularly susceptible to mechanical stress due to the load it bears and the vibrations generated during motorcycle operation.

The onset of stress occurs with a force of 58.8430 N, corresponding to a speed of 65 km/h, with an equivalent stress of

1.5207 MPa. At this stage, stress distribution remains low and does not significantly impact the structure. However, as the applied load increases, stress progressively grows, showing an upward trend in the material's response to the imposed loading conditions.

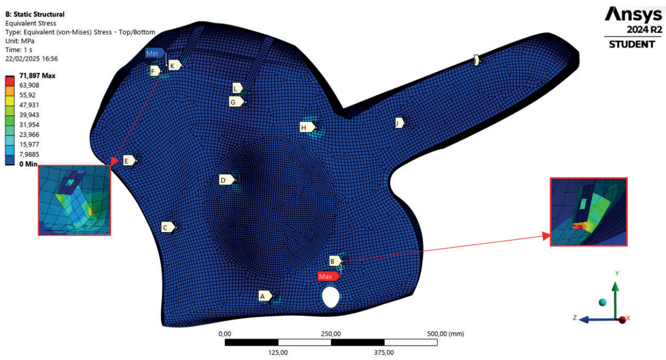

Fig. 22. Deformation stress, Von Mises criterion.

By analyzing the reaction forces at different fairing anchorage points, it was found that one of these points exhibited a significantly higher reaction compared to the others. This behavior is explained by its proximity to an area of the fairing where lateral deformation occurs. The presence of this deformation indicates a stress concentration in that specific area, allowing for an evaluation of the effectiveness of the supports used, as illustrated in Figure 23. These supports play a crucial role in distributing the loads, demonstrating their capability to prevent failures at the most critical anchorage points. Thanks to this proper load distribution, potential breakage or crack formation in the fairing is prevented, thus ensuring its structural integrity and extending its service life.

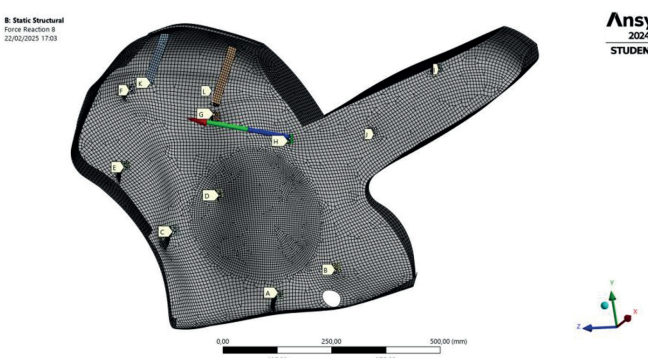

Fig. 23. Fairing reaction force distribution diagram.

F. Modal Simulation Results

The results obtained in Ansys Modal allow for the analysis of the natural frequencies and the maximum deformation of the motorcycle fairing. The simulation reveals a total of 6 vibration modes, showing displacements in the three Cartesian axes, as described in Table IV. Additionally, in the final vibration mode, a dual action is observed on the X-axis, indicating a greater influence of this axis on the dynamic behavior of the fairing.

TABLE IV
NATURAL FREQUENCY, MAXIMUM DEFORMATION AND NATURE OF FAIRING DISPLACEMENT

Mode	Natural Frequency [Hz]	Maximum. Deformation [mm]	Nature of displacement
1	42.194	31.371	Bending along Y-axis
2	54.703	25.653	Curving along Z-axis
3	60.425	28.566	Curving along Z-axis
4	61.924	44.787	Curving along X-axis
5	69.393	30.851	Twisting along X-axis
6	78.022	15.788	Twisting and bending along X-axis

Complementing the data in Table IV, Figure 24 visually illustrates the different ways the structure deforms when subjected to various natural frequencies. Through this schematic representation, it is possible to analyze the behavior of the fairing under different vibration conditions, allowing for the identification of deformation patterns.

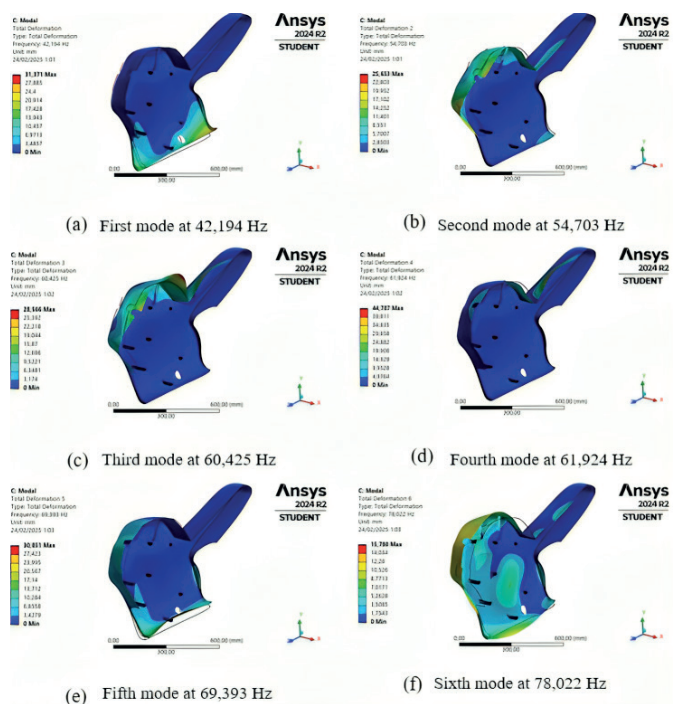

Fig. 24. Modal displacement shapes of the fairing.

In the modal analysis, the highest recorded deformation reaches a value of 44.787 mm, corresponding to mode 4, which has a frequency of approximately 61.924 Hz. On the other hand, the minimum deformation observed is 15.78 mm, associated with the last mode, with a frequency of 78.022 Hz—values within the range of 65 Hz to 135 Hz established for internal combustion motorcycles [36], adapted here for electric motorcycle conditions.

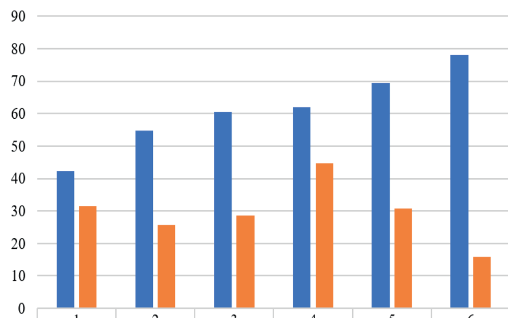

	1	2	3	4	5	6
Natural Frequency [Hz]	42,194	54,703	60,425	61,924	69,393	78,022
Max. deformation [mm]	31,371	25,653	28,566	44,787	30,851	15,788

Fig. 25. Comparison of natural frequency and maximum deformation.

In the harmonic analysis, shown in Figure 26, the deformation of the fairing along the X, Y, and Z axes is presented, each with distinct behavior. The maximum amplitude recorded is 4.0105 mm at a frequency of 6.5 Hz in the Y and Z axes, while for the X-axis, the maximum amplitude reaches 2.3558 mm at the same frequency. As the frequency increases, a progressive decrease in deformation amplitude is observed. In the X-axis, deformation decreases to 0.14686 mm at a frequency of 13 Hz. Meanwhile, the Y and Z axes also show a downward trend, reaching an equal value of 0.26355 mm at a frequency of 26 Hz.

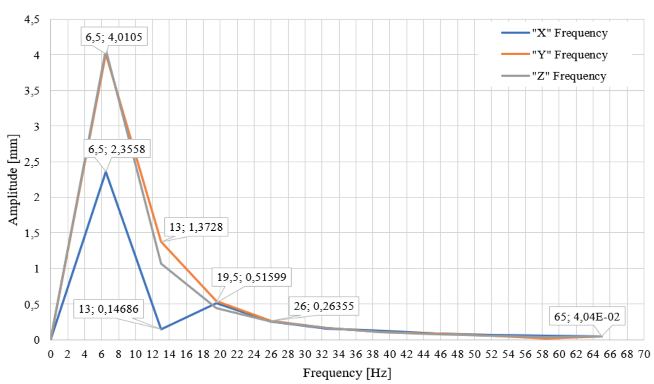

Fig. 26. Graphical comparison of frequency and amplitude.

IV. CONCLUSIONS

First, for the development of the designs, the Industrial Design Structure (IDes) methodology was key to analyzing current trends in motorcycle design to have an initiative with the initial sketches and CAD models. This allowed defining the fairing's aesthetics with its own identity. Considering the guidelines of the MotoStudents Regulations, which helped delimit key aspects such as external dimensions and edge thickness, enabling the creation of a functional and aerodynamic fairing criterion.

In the selection of the most efficient design, priority was given to reducing drag resistance and lift. Design 3 obtained the best results, with a drag coefficient of 0.282 and a lift coefficient of -0.273. These values were validated through a meshing analysis that yielded a skewness of 0.23 (rated as excellent) and an orthogonal aspect ratio of 0.76 (very good). Additionally, the airflow around the fairing prevents vortex formation at the outlet, which could affect the motorcycle's stability, and inside, a balanced flow is achieved, promoting better heat exchange.

The best material option is epoxy resin with S-type pre-impregnated unidirectional fiberglass, with a thickness of 3 mm. In the structural simulation, this material showed a deformation of 0.35339 under a force of 2100 N, confirming its resistivity. The validation demonstrates that a balanced mesh was achieved by the ninth iteration, remaining within the range of 0.02 to 5%, allowing to avoid unnecessary computational resource expenses.

The modal analysis allowed studying the fairing's behavior under vibrations. It was identified that the most impactful frequency is 78.022 Hz, with a total deformation of 15.788 mm. A maximum amplitude of 6.5 Hz was also observed in the X and Y axes, indicating that the fairing can withstand the motorcycle's dynamic conditions without compromising its structure.

REFERENCES

[1] M. T. Folgôa, C. Grande, C. Vásquez, L. Suárez, L. M. Navas, R. Ramirez, R. Pérez, R. Andara, and C. Fajarta, "Ide y movilidad sostenible: Estado del arte en iberoamérica," *Universidade de Évora*, p. 14, 2022. [Online]. Available: http://hdl.handle.net/10174/35665

[2] D. Moser, Ed., *Movilidad eléctrica sostenible: Componentes esenciales y recomendaciones de políticas*, 2021. [Online]. Available: https://www.sum4all.org/data/files/buildingblocksandpolicyrecommendations_spanish.pdf

[3] L. Abarca and L. J. Choque, "Estado actual de los impactos ambientales producidos por actividades del sector automotriz en latinoamérica, revisión sistemática de los últimos 10 años," Ph.D. dissertation, Universidad César Vallejo, Ubicación, 2022, sistemas de Gestión Ambiental. [Online]. Available: https://repositorio.ucv.edu.pe/handle/20.500.12692/110424

[4] K. Wiński and A. Piechna, "Comprehensive cfd aerodynamic simulation of a sport motorcycle," *Energies*, vol. 15, no. 16, p. 27, 2022. [Online]. https://doi.org/10.3390/en15165920

[5] F. Concli, M. Gobbi, and C. Gorla, "Aerodynamic study of motorcycle racing wheels: A performance evaluation based on numerical cfd simulations," *International Journal of Computational Methods and Experimental Measurements*, vol. 7, no. 3, pp. 275-284, 2019. [Online]. https://doi.org/10.2495/CMEM-V7-N3-275-284

[6] A. de Empresas Automotrices del Ecuador, Ed., *Anuarios 2023*, 2023. [Online]. Available: https://www.aeade.net/anuario/

[7] J. Trujillo and L. Joseph, "Diseño aerodinámico del carenado de una motocicleta eléctrica fabricada en la usiek," Ph.D. dissertation, Universidad Internacional SEK, Ubicación, 2022, mecánica Automotriz. [Online]. Available: https://repositorio.uisek.edu.ec/handle/123456789/4886

[8] K. Puga S., "Tant trabaja en reglamento para regular motos eléctricas y scooters en ecuador," El Comercio, Dec 2024. [Online]. Available: https://www.elcomercio.com/actualidad/ecuador/ant-reglamento-regulacion-motos-scooter.html

[9] L. Frizziero, C. Leon, G. Galiè, G. Alessandri, L. Iannarelli, L. Lucci, S. Merighi, and P. Polignano, "Ides method applied to an innovative motorbike–applying topology optimization and augmented reality," *Inventions*, vol. 7, no. 4, 2022. [Online]. https://doi.org/10.3390/inventions7040091.

[10] E. Méndez, I. Coronel Villavicencio, E. Pacha Herrera, B. Briceño Martínez, E. Tapia Viñan, and J. Camacho Muñoz, "Feasibility analysis of charging stations for electric vehicles: Case study route e35, loja-cuenca in ecuador," *IOP Conference Series: Earth and Environmental Science*, vol. 1370, no. 1, 2024. [Online]. https://doi.org/10.1088/1755-1315/1370/1/012003

[11] O. Farrerons Vidal and I. Roldán Aguilar, "Competición motostudent diseño de un carenado," *IV Jornada de Recerca Enginyeria Gràfica i*

de Disseny UPC, p. 10, 2022. [Online]. Available: https://upcommons.upc.edu/bitstream/handle/2117/364817/Dise%C3%B1o_carenado_competicion_Recerca_EGD_2022%20.pdf?sequence=1

[12] MotoStudent, *V. Competición Internacional MotoStudent*, 2018. [Online]. Available: https://www.academia.edu/32627471/Reglamento_de_la_Competici%C3%B3n

[13] T. Gómez Morales, J. M. Navarro, E. Águera Casado, and J. L. García Jiménez, *Estructuras del vehículo*. Paraninfo S.A., 2016.

[14] H. Granados, (2022). *Aprender a usar SolidWorks Superficies - nivel principiante*. [Online]. Available: https://intelligy.com/blog/2022/02/01/aprende-a-usar-solidworks-superficies-nivel-principiante/

[15] J. Constante, "Metodología de "análisis de densidad del aire" y "análisis horario"," *Instituto de Investigación Geológico y Energético*, p. 7, 2022. [Online]. Available: https://www.geoenergia.gob.ec/wp-content/uploads/downloads/2022/05/documento_densidad_del_aire.pdf

[16] Y. F. Görgülü, M. A. Özgür, and R. Köse, "Cfd analysis of a naca 0009 aerofoil at a low reynolds number," *Politeknik Dergisi*, vol. 24, no. 1, pp. 191-198, 2021. [Online]. https://doi.org/10.2339/politeknik.877391.

[17] S. Gancang, R. Sugeng, Abdurrouf, P. S. Setyawan, and N. Muhammad, "Stretched meshing in a 2d computational domain with elbow edges for cfd applications," *Journal of Advanced Research in Fluid Mechanics and Thermal Sciences*, vol. 116, no. 2, pp. 41-50, 2024. [Online]. https://doi.org/10.37934/arfmts.116.2.4150.

[18] J. L. Vásquez, "Diseño asistido por computador y construcción de la carrocería de una moto eléctrica," Ph.D. dissertation, Universidad Autónoma de Bucaramanga - UNAB, Colombia, 2020. [Online]. Available: https://redcol.minciencias.gov.co/Record/UNAB2_4fcad73f77b35585a14d2757eb168ed

[19] D. C. Wilcox, "Reformulation of the k-ω turbulence model revisited," *AIAA Journal*, vol. 46, no. 11, pp. 2823-2838, 2008. [Online]. https://doi.org/10.2514/1.36541.

[20] E. Douvi and D. Margaris, "Evaluation of the turbulence models for the simulation of the flow over a national advisory committee for aeronautics (naca) 0012 airfoil," *Journal of Mechanical Engineering Research*, vol. 4, no. 3, pp. 100-111, 2012. [Online]. https://doi.org/10.5897/JMER11.074.

[21] F. Stupenengo, *Estructuras del vehículo*. Inet, 2011. [Online]. Available: https://www.inet.edu.ar/wp-content/uploads/2012/11/materiales-compuestos.pdf

[22] S. Kalpakjian and S. R. Schmid, *Manufactura, ingeniería y tecnología*, 5th ed., México, 2008.

[23] T. L. Saaty and L. G. Vargas, *Models, Methods, Concepts Applications of the Analytic Hierarchy Process*, springer ed., United States, Jun 2012.

[24] C. Devals, T. C. Vu, Y. Zhang, J. Dompierre, and F. Guibault, "Mesh convergence study for hydraulic turbine draft-tube," *IOP Conference Series: Earth and Environmental Science*, vol. 49, no. 8, 2016. [Online]. https://doi.org/10.1088/1755-1315/49/8/082021

[25] J. Leguisamo and D. Cuaspud, "Análisis estructural en cargas de impacto posterior por alcance de un bus interprovincial mediante el método de elementos finitos," Ph.D. dissertation, Universidad Internacional SEK, Ecuador, 2018. [Online]. Available: https://repositorio.uisek.edu.ec/bitstream/123456789/2768/2/tesis%20impacto%20posterior%20%20bus.pdf

[26] E. R. Tapia Viñán and C. A. González Herrera, "Estudio de dimensionamiento y caracterización de un motor eléctrico en rueda para una motocicleta," Ph.D. dissertation, Universidad Nacional de Loja, Ecuador, 2024. [Online]. Available: https://dspace.unl.edu.ec/jspui/handle/123456789/31555

[27] J. V. Molina Osejos and L. J. Trujillo Tinizaray, "Diseño aerodinámico del carenado de una motocicleta eléctrica fabricada en la usiek," Ph.D. dissertation, Universidad Internacional SEK, Ecuador, 2022. [Online]. Available: https://repositorio.uisek.edu.ec/handle/123456789/4886

[28] D. P. Cajamarca Sumba and C. D. Vásquez Remache, "Diseño y construcción de la carrocería para el prototipo de competencia shell eco marathon," Ph.D. dissertation, Universidad del Azuay, Ecuador, 2016. [Online]. Available: https://dspace.uazuay.edu.ec/handle/datos/6258

[29] Y. A. Çengel and J. M. Cimbala, *Mecánica de Fluidos: Fundamentos y Aplicaciones*, 1st ed. México: McGraw-Hill, 2012.

[30] K. Lluguay Duchi, "Desarrollar un modelo cfd para el análisis del comportamiento del fluido en tuberías del banco de perdidas de turbomaquinaria hidráulica y laboratorio," Ph.D. dissertation, Escuela Superior Politécnica de Chimborazo, Ecuador, 2016. [Online]. Available: https://dspace.espoch.edu.ec/handle/123456789/4650

[31] Z. M. Saleh and A. H. Ali, "Numerical investigation of drag reduction techniques in a car model," *IOP Conference Series: Materials Science and Engineering*, vol. 671, no. 1, 2020. [Online]. https://doi.org/10.1088/1757-899X/671/1/012160.

[32] A. N. M. M. I. Mukut and M. Z. Abedin, "Review on aerodynamic drag reduction of vehicles," *International Journal of Engineering Materials and Manufacture*, vol. 4, no. 1, pp. 1-10, 2019. [Online]. https://doi.org/10.26776/ijemm.04.01.2019.01

[33] R. D. R. Mariaprakasam, S. Mat, P. Mohd Samin, N. Othman, M. Ab Wahid, and M. Said, "Review on flow controls for vehicles aerodynamic drag reduction," *Journal of Advanced Research in Fluid Mechanics and Thermal Sciences*, vol. 101, no. 1, pp. 11-36, 2023. [Online]. https://doi.org/10.37934/arfmts.101.1.1136

[34] N. Bekraoui, Z. El Qoubaa, and E. Essadiqi, "Weibull integrated ahp for the selection of natural fiber composites material," *Jordan Journal of Mechanical and Industrial Engineering*, Mar 2023. [Online]. Available: 05_JJMIE_263_22

[35] W. P. Medina Toledo and J. F. Morocho Salinas, "Diseño y construcción de manguetas y cubos de rueda de un vehículo de competencia fórmula sae eléctrico," Ph.D. dissertation, Universidad Politécnica Salesiana Sede Matriz Cuenca, Ecuador, 2017. [Online]. Available: https://dspace.ups.edu.ec/handle/123456789/15056

[36] F. Yu, J. Xie, and Z. M. Xu, "The vibration reduction design of single-cylinder engine based on the balance shaft," *Vibroengineering Procedia*, vol. 26, pp. 20-25, 2019. [Online]. https://doi.org/10.21595/vp.2019.20651

ENFOQUE UTE REVISTA
Facultad Ciencias de la Ingeniería e Industrias

RESEARCH ARTICLE

ENFOQUE UTE, VOL. 16, NO. 3, pp. 37-43, E-ISSN: 1390-6542
RECEIVED FEBRUARY 26, 2025; ACCEPTED MAY 21, 2025; PUBLISHED ONLINE JULY 1, 2025; DATA OF CURRENT VERSION JULY 1, 2025; PUBLISHED IN VOLUME 16, ISSUE 3 (JULY 2025).

Use of carbon activated impregnated with Fe to enhance methane production of wastewater from nixtamalization process

Vianey A. Burboa Charis[1], Margarita S. Escalante Torres[2], Miguel A. Armenta Gutiérrez[3], Lourdes M. Tenorio Diaz[4], Luis A. Leyva Soto[5], Angel R. Meza[6], Luis H. Álvarez Valencia[7*]

Abstract — **Wastewater from the nixtamalization process represents a challenge due to its complex and highly alkaline composition. The present work aims to enhance methane production by anaerobic digestion of nejayote with conductive materials based on carbon modified with iron. Through two experimental phases, the most significant results show that the metal load in granular activated carbon (GAC) does not stimulate electron transfer in a medium such as nejayote. On the other hand, when the pH is kept at neutral values, an 88 % reduction in COD and high values of accumulated methane are obtained. The study describes the relationship between using GAC and nejayote as a methane promoter in anaerobic digestion, which can be a sustainable alternative.**

Keywords: **Anaerobic digestion, wastewater, nejayote, methane production, conductive materials, direct interspecies electron transfer (DIET).**

Resumen — **Las aguas residuales provenientes del proceso de nixtamalización representan un reto por su composición compleja y altamente alcalina. El presente trabajo tiene como objetivo potenciar la producción de metano mediante la digestión anaeróbica de nejayote con materiales conductores a base de carbón modificado con hierro. A través de dos fases experimentales, los resultados más significativos muestran que la carga metálica en el carbón activado granular (CAG) no estimula la transferencia de electrones en un medio como el nejayote. Por otro lado, cuando el pH se mantiene en valores neutros, se obtiene una reducción del 88 % en la DQO y altos valores de metano acumulado. El estudio describe la relación entre el uso del CAG y el nejayote como promotor de metano en la digestión anaeróbica, lo que puede ser una alternativa sustentable.**

Palabras Clave: **Digestión anaerobia, agua residual, nejayote, producción de metano, materiales conductores, transferencia directa de electrones entre especies (DIET).**

I. INTRODUCTION

CORN is the crop that generates the most significant economic value in Mexico (seven largest producer worldwide) [1]. The tortilla is the main way of consuming corn in Mexico and is a fundamental part of its diet [2], the annual per capita tortilla consumption in urban areas is 56.7 kg, and in rural areas is 79.5 kg [3]. Most corn-based products are subjected to an alkaline treatment called nixtamalization, which allows them to increase their nutritional value [4]. Nixtamalization is a thermo-alkaline treatment that consists of cooking corn by adding calcium hydroxide, this preparation is cooked for 50 to 90 minutes and left to soak in the cooking water for 14 to 18 hours [5], [6]. This treatment helps to remove the pericarp from the grain, making amino acids (niacin and tryptophan) and minerals such as calcium more available; it also facilitates milling and improves the adhesiveness and extensibility of the dough produced [7]. After soaking, the cooking water known as “nejayote” is removed. Nejayote has an approximate composition of 92 - 94% water with a large amount of organic matter, and 6-8% solid corn residues, which include the pericarp, endosperm, germ, calcium and carotenoids, which give it its characteristic yellow pigmentation [6], [8]. It is estimated that a tortilla factory with a capacity of 600 tons of corn/day generates between 1500 and 2000 m^3 of nejayote [9]. Nejayote is one of the most challenging effluents to treat because it is

* *Corresponding autor:* luis.alvarez@itson.edu.mx
1. Vianey A. Burboa Charis. Dpto. Biotecnología y Ciencias Alimentarias, Instituto Tecnológico de Sonora, Ciudad Obregon, Sonora, México. vburboach@gmail.com, ORCID number https://orcid.org/0000-0001-7210-7219
2. Margarita Sarai Escalante Torres. Dpto. Ciencias del Agua y Medio Ambiente, Instituto Tecnológico de Sonora, Ciudad Obregon, Sonora, México. E-mail: Margarita.escalante213000@potros.itson.edu.mx.
3. Miguel A. Armenta. Dpto. Biotecnología y Ciencias Alimentarias, Instituto Tecnológico de Sonora, Ciudad Obregon, Sonora, México. E-mail: angel456_1@hotmail.com, ORCID number https://orcid.org/0000-0001-7865-618X
4. Lourdes M. Tenorio Diaz. Dpto. Biotecnología y Ciencias Alimentarias, Instituto Tecnológico de Sonora, Ciudad Obregon, Sonora, México. E-mail: lourdes.diaz@itson.edu.mx, ORCID number https://orcid.org/0000-0002-8941-3965
5. Luis A. Leyva Soto. Dpto. Biotecnología y Ciencias Alimentarias, Instituto Tecnológico de Sonora, Ciudad Obregon, Sonora, México. E-mail: luis.leyva@itson.edu.mx, ORCID number https://orcid.org/0000-0002-8101-7925
6. Angel R. Meza. Dpto. Biotecnología y Ciencias Alimentarias, Instituto Tecnológico de Sonora, Ciudad Obregon, Sonora, México. E-mail: angel_esquer@hotmail.com, ORCID number https://orcid.org/0000-0002-4048-8958
7. Luis H. Álvarez. Dpto. Biotecnología y Ciencias Alimentarias, Instituto Tecnológico de Sonora, Ciudad Obregon, Sonora, México. E-mail: luis.alvarez@itson.edu.mx, ORCID number https://orcid.org/0000-0003-1809-9304.

DOI: https://doi.org/10.29019/enfoqueute.1144
Associate Editor: *Miriam Recalde*

highly alkaline (pH>10) and has high concentrations of dissolved and suspended organic matter, with values of biological oxygen demand (BOD) between 7000 to 14 000 mg/L and Chemical oxygen demand (COD) in a range from 10 000 to 20 000 mg/L [10], [11]. Nejayote is rarely treated and is discharged directly into surface waters or public sewers [12]. This effluent generates turbidity and causes a reduction in dissolved oxygen, compromising the survival of various aquatic organisms. It also increases the content of nutrients (N and P), which contribute to the eutrophication process, leading to a significant environmental impact [11], [13].

Aerobic water treatment systems are not considered an option due to the characteristics of nejayote; however, anaerobic digestion (AD) is a viable option for eliminating the organic load and producing biogas. AD is a four-stage biological process (hydrolysis, acidogenesis, acetogenesis, and methanogenesis); in the absence of oxygen, a mixed consortium of microorganisms transforms complex organic matter into its most oxidized (CO_2) and most reduced (CH_4) states [14]. The strategy through AD of generating clean energy from methane and biohydrogen has been explored [12], [15]. Currently, strategies have been established to improve the stages of AD, especially for complex compounds, and adequate electron transfer is required to increase the methane content in biogas. Direct electron transfer between species (DIET) is a syntrophic process that effectively promotes electron transfer in the anaerobic microbial consortium, being able to give up and accept electrons directly between species, promoting methane production during anaerobic digestion, in which they can involve electroactive bacteria, methanogens, anaerobic methane-oxidizing consortia, *Geobacter* species and co-cultures [10], [17]. Several studies have reported using electron-conducting materials, which improve the syntrophic relationships between fermentative bacteria and methanogenic archaea during methane production. Some processes in which conductive materials participate and promote during anaerobic digestion are shown in Fig. 1. In the last decade, carbon-based materials have been widely studied; in 2012, the use of iron oxide minerals was reported, obtaining favorable results, such as an increase in the maximum methane production rate and a significant reduction in the lag phase [18]. Adding carbon-based materials and metals is an option to improve methanogenesis during AD processes.

The main objective of this work is to treat wastewater from the nixtamalization process (nejayote) using carbon-based conductive materials, with and without iron, to enhance methane production. The objective was achieved through two experimental phases: 1) To evaluate the impact of different percentages of Fe in activated carbon to increase methane production during anaerobic digestion of nejayote; 2) To evaluate the production and composition of biogas by anaerobic digestion of nejayote, in a reactor with continuous stirring (CSTR) added with conductive material.

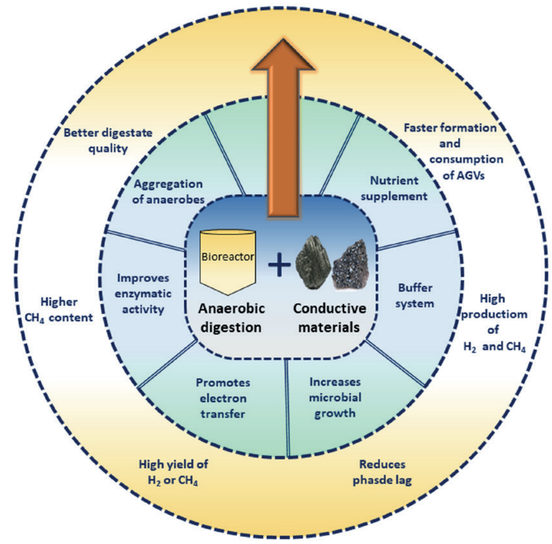

Fig. 1. Processes in which conductive materials participate and promote during anaerobic digestion and their impact on the productivity of methane and other products. Adapted from [19].

II. MATERIALS AND METHODS

A. Wastewater and inoculum

The nejayote wastewater was collected from a small corn tortilla factory that uses the nixtamalization process, located in Cd. Obregon, Mexico. The wastewater was sedimented for 24 hours, and pH and soluble chemical oxygen demand (CODs) were subsequently determined. The anaerobic granular sludge used for both experimental phases contained 16 % volatile suspended solids (VSS) in wet weight, collected from a large-scale UASB reactor of a local brewery, and dispersed to obtain a particle size of 425 µm. It was used as inoculum without prior acclimation to nejayote.

B. Conductive materials

Granular activated carbon (GAC) was used during the AD kinetics for methane production, which was produced from bituminous coal (Carbotecnia), was crushed and sieved to obtain particles between 150 and 250 µm; it was subsequently washed with distilled water to remove fine particles and dried at 55 ºC for 24 h. The modification of the GAC was carried out by an impregnation method [20], with Fe doses of 0.25, 0.5, and 1 %, in a solution of iron nitrate ($Fe(NO_3)_3 \cdot 9H_2O$) (Sigma-Aldrich) by weight according to Equation 1:

$$\frac{\%A}{100}/\mathrm{MW}_A \times \mathrm{MW}_B \times C \quad (1)$$

A is the metal used, *MWA* is the molecular weight of the metal, *MWB* is the molecular weight of the precursor metal, and *C* is the mass of the supporting material. The impregnation was carried out with 10 g of GAC with the iron nitrate solutions at 80 °C for 8 h at neutral pH, then the water present in each solution was evaporated at 110 °C for 12 h and finally thermally activated at 350 °C for 4 h with a temperature ramp of 10 °C/min.

C. Methane production kinetics with nejayote

The first experimental phase was carried out in 120 mL serological bottles, with 60 mL of nejayote operating volume. The initial CODs concentration was 15,688± 90 mg/L, inoculated with 1 g of SSV/L of anaerobic sludge. The bottles were sealed with rubber stoppers and aluminum caps, and then N2 was bubbled into the liquid to establish an anaerobic atmosphere. The incubations in triplicate were placed in an orbital shaker at 37 ºC and 130 rpm for 15 days. The liquid displacement method used a 2 % NaOH solution to determine the volume of methane produced. At the end of the kinetics, pH, and COD were determined; likewise, the results of methane production were analyzed to determine the kinetic parameters using the modified Gompertz model (Eq. 2) [21].

$$P = P_{\max} \cdot \exp\left\{-\exp\left[\frac{2.71828 \cdot R_{\max}}{P_{\max}} \cdot \left(\lambda - t\right) + 1\right]\right\} \qquad (2)$$

Where P is the cumulative methane production (mL), $Pmax$ is the maximum methane production (mL), $Rmax$ is the maximum methane production rate (mL/day), t is the time (days), and λ is the lag phase (days). Parameters were estimated using Statistic Six Sigma 13 with minimal sum-of-squares residual errors between the experimental data and the model curves. Additionally, analysis of variance and Tukey test were performed with statistical software (InfoStat) to determine differences between means ($p < 0.05$).

To carry out the second phase, based on the results obtained in the first experimental phase, the iron-free GAC was selected to be added into a tank reactor with continuous stirring (150 rpm) at 37 ºC for 20 days, with an operating volume of 2 L, initial pH of 12.54 that was adjusted to 7.05, during the operation it was regulated to pH 7.1, using a NaOH solution (5M), this pH was selected because it favors the metabolism of methanogenic bacteria, the reactor was inoculated with 1 g SSV/L of granular anaerobic sludge and 10 g/L of the selected conductive material was added. The initial CODs was 12392 ± 153 mg/L. 2 mL were taken each day to evaluate CODs, which was previously centrifuged at 5000 rpm for 5 minutes. The methane produced was quantified by an automatic methane meter (AMPTS II equipment from BPC Instruments, Sweden); the composition of the gas produced was a gas chromatograph (Shimadzu Nexis GC-2030), equipped with a polar capillary column (ZB-624PLUS, 30 m length, 0.32 mm diameter, 1.0 µm film thickness), in the same equipment ethanol, acetic, propionic and butyric acids were determined from liquid samples taken periodically, previously centrifuged at 5000 rpm for 5 minutes and filtered through a 0.22 µm membrane.

III. RESULTS AND DISCUSSION

Nejayote wastewater is a complex effluent with a high variation in COD; this may be due to the tortilla production method, type of corn, quality of water used, amount of lime, and cooking time [22]. Nejayote water cannot be treated by a biological system without prior conditioning, specifically pH adjustment, due to its high alkalinity, inhibiting microorganism's metabolism. To achieve DA, it is necessary to consider that if the objective is to produce methane, the pH must range between 6.8 and 7.2 [23].

A. First experimental phase: impact of different percentages of Fe in activated carbon to increase methane production during anaerobic digestion of nejayote

The results of accumulated methane volume are shown in Fig. 2, in order from highest to lowest production for each condition evaluated: Control>GAC>GAC + Fe 0.25 % > GAC + Fe 0.5 % > GAC + Fe 1 %. The accumulated volume does not show a significant difference between the control and GAG with the lowest Fe loads (0.25 and 0.5 %). On the other hand, the CAG with the highest load obtained the lowest methane production (56.5 mL), being 14 % lower than the control. Use trace metals like Fe, Co and Ni has been proved to stimulate the growth of anerobic microorganisms and improve bacteria activity and increase the yield of gas [24], [25]. Nonetheless, research reported in 2024, where they evaluated GAC impregnated with 1.5 and 3 % of Fe, values higher than those carried out in this work, suggests that the increase in the metal load blocks the pores of the GAC, which limits the interaction between the effluent and the microbial consortium [26]. The increase in the metal load in the GAG does not favor methane production with treat nejayote.

The final COD are shown in Table 1, the highest GAC + Fe 0.5 % had the highest COD consumption, followed by GAC + Fe 0.25 %. GAC reduced COD by 23 % more compared to the control. GAC + Fe 1% only reduced COD by 7.3 % less than the final control value. The results with a lower metal load (Fe 0.25 %) favor a reduction in organic load, however, the DIET mechanism is not promoted because it does not increase methane production.

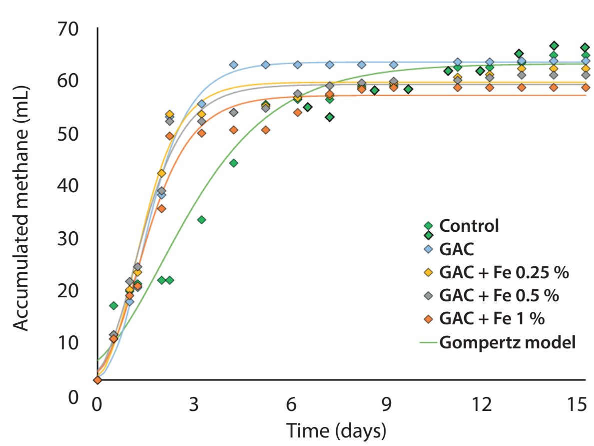

Fig. 2. Production of accumulated methane from nejayote DA with Fe-impregnated conductive materials.

Carbon-based conductive materials have been widely used to stimulate the DIET by enhancing electron transfer for methane production [27], especially the use of GAC, due to their electrical conductivity, surface area, biofilm formation capacity, corrosion resistance, and potentially toxic substance adsorption capacity [28], [29]. Depending on the type of GAC, the adsorption mechanism can occur through physical interactions (microporosity and particle size) and chemical interactions (elemental composition, functional groups, and point of zero charge) [30]. In order to select the material that can achieve the best performance for producing methane, not only its properties and characteristics must be considered, but it will also depend on the interaction between the microbial consortium and the working medium, which is the case in nejayote. According to the results, the CAG does manage to reduce the organic load present in the nejayote, compared to the GAC impregnated with Fe and the control. For this reason, the Gompertz kinetic parameters will be crucial to determine the selection of the conductive material.

TABLE I
FINAL PH, REMOVAL COD AND ACCUMULATED METHANE OF ANAEROBIC DIGESTION OF NEJAYOTE WITH GAC AND GAC WITH DIFFERENT PERCENTAGES OF FE

Condition	Final COD (mg/L)	Removal COD (%)	Accumulated methane (mL)	Final pH
Control	8,596.6	45.2	64.4	4.78
GAC	6602.5	57.9	63.3	4.72
GAC + Fe 0.25%	5875.0	62.5	61.8	4.76
GAC + Fe 0.5%	5300.8	66.2	60.5	4.72
GAC + Fe 1%	7965.0	49.2	56.5	4.71

The kinetic parameters obtained from the accumulated methane production, according to the maximum methane production, GAG obtained the highest value (66.11 mL), followed by the control (62.81 mL), while the GAC impregnated with Fe obtained similar values, with an average of 58.09 mL ± 1.13 mL, all conditions do not show statistically significant difference between them (Tukey test $p < 0.005$), this reiterate that adding iron salts does not stimulate methane production when the medium is nejayote. The use of GAG + magnetite was reported, in concentrations of 20 to 40 g/L with dairy industry wastewater, which also has a highly alkaline pH, has been reported, achieving an 80% increase in the methane production rate and a 90% increase in methane conversion [31]. The difference in the results suggests that the interactions between the conductive material, medium, and consortium change according to the origin and composition of the wastewater, even when they share physicochemical characteristics, such as alkalinity and organic matter content.

The *Rmax* results (Fig. 3) show the impact of the conductive material on the DA process, where the production rate is stimulated by the effect of the DIET, being 2.3 times faster GAC and GAG + Fe 0.25 % with respect to the control, while GAG with 0.5 and 1.0 % of Fe, were 2 times faster compared to the control. Therefore, GAC without metal loading can produce faster and higher volumes of methane since there is a statistically significant difference with respect to the control and GAC with iron (Tukey test $p < 0.005$). Iron can be easily dissolved, allowing it to be used as a micronutrient in methanogenesis in different ways, both positive and negative, all depending on its physicochemical properties and its syntrophic partners [32], which directly influences methane production.

The efficiency of methane production is one of the most important criteria during anaerobic digestion [33], there are several factors that influence it, such as pH, temperature, inoculum, among others; however, the pH value is the fundamental factor. The final average pH of the conditions tested was 4.73 (Table 1), this can cause inhibition for the methanogenic consortium, which is why methane production can be stopped; The optimal pH range to obtain the maximum methane yield in anaerobic digestion is 6.5 to 7.5, the range is relatively wide on the plant scale and the optimal pH value varies with the type of effluent and mode of operation [34]. It is highly recommended to keep this physical parameter at neutral values to promote COD consumption, which can allow high methane production.

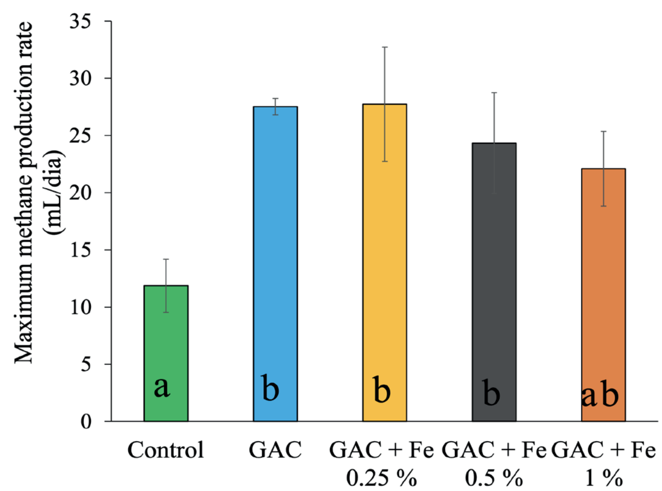

Fig. 3. Maximum methane production rate (*Rmax*) determined from Gompertz model.

B. Second experimental phase: production and composition of biogas in CSTR added with conductive material.

The use of a CSTR reactor allows the control of the pH in an optimal range for methane production. The results showed that the COD was reduced by 88 %, considering the initial and final values. At the end of the kinetics, the accumulated methane volume was 6312 mL. Fig. 4 shows the COD consumption over time, in contrast to the generation of produced methane. GAC has been used before in real and synthetic effluents, reporting values ranging from 60 to 70 % in methane production with residual water from the brewing industry with 5 g GAC/L [35]; with residual activated sludge with 27 g GAC/L, an increase of 37 % in methane production [36]. GAC is a material that stimulates the DIET process by promoting electron transfer. Fig. 4 shows a null lag phase and a direct relationship between the consumption of organic matter and methane production obtained from the DA of nejayote, which has not been previously reported.

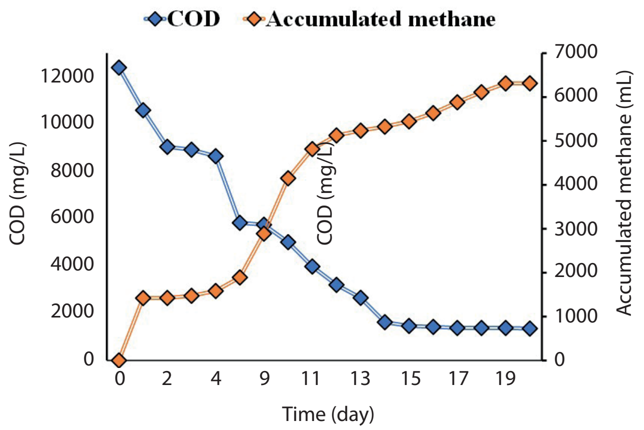

Fig. 4. Methane production and COD consumption of nejayote DA with GAC.

In several studies, the increase of methane content in the biogas produced has been reported when GAC is added to AD systems [37], [38]. Fig. 5 shows the biogas composition produced during days 2, 6, 10, and 12; the percentage of methane during the first days confirms methanogenic activity, with values close to 90%, positively impacting the methane production rate. However, the percentage of methane in the biogas is reduced on day 6; this may be due to a change in the composition of the medium or a change in the metabolic route by the consortium since there is a considerable increase in the CO_2 content, however, from day 10, the methane content remained between 85-90% approximately, suggesting that GAC promotes DIET by significantly increasing the methane content in the biogas produced during the AD of nejayote. The typical composition of CH_4 is reported to be between 50 to 75 % and CO_2 to be between 25 and 50 % [39]. GAC could allow biomethane generation from the anaerobic digestion of nejayote, representing an alternative energy source.

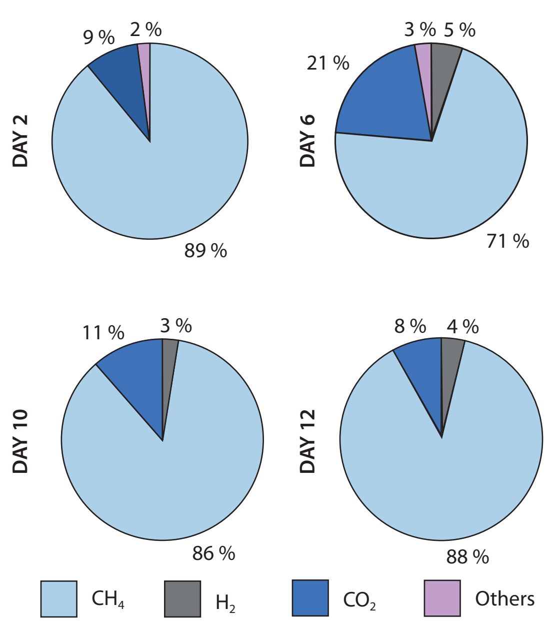

Fig. 5. Composition of biogas produced during AD of nejayote with GAC.

The final pH was 7.31, which favors the methanogenic consortium due to the high consumption of organic matter. The acidification obtained in the first experimental phase could occur due to the accumulation of organic acids, such as volatile fatty acids (propionic, butyric, valeric, among others). Fig. 6 shows the production of ethanol (ET), acetic acid (AA), propionic acid (PA) and butyric acid (BA). Raw nejayote contains 26.5 % ET, 42.9 % AP, and 30.5 % BA. During the first days, the concentration of these intermediate products increases. From the fifth day on, the ET is reduced to 12 %, decreasing as the days go by until reaching values of 1 %, causing an accumulation of PA and BA.

GAC stimulates DIET through the consumption of VFA [40]; however, the accumulation of PA and BA, which are compounds not directly consumed by methanogenic bacteria, favors the stabilization of methanogenic microorganisms [41]. Therefore, it is necessary to continue evaluating the different conductive materials to understand better and describe the interactions between the medium, microorganisms, and the tested material. It is advisable to work with a controlled medium, where the optimal pH range of the metabolism of the microorganisms of the producer of interest is maintained, methane being the objective of this work, to interpret a response and behavior mechanism. This allows to continue developing research and to be able to generate a universally accessible database to consider proposals to treat a complex effluent such as that of the nixtamalization process.

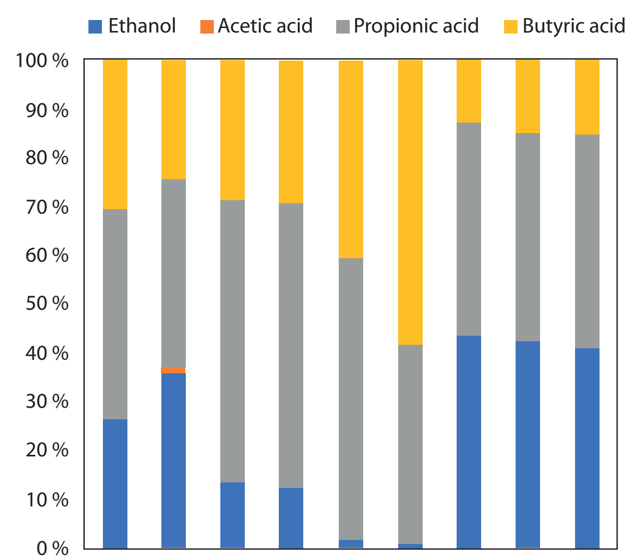

Fig. 6. VFA production during AD of nejayote with GAC.

IV. CONCLUSIONS

Nejayote is a complex effluent, which represents a challenge for its treatment, where DA is a viable option, which promotes an energetic valorization of said effluent, methane is an alternative source of energy with a calorific value higher than that of hydrocarbons. The GAC modified with iron does not stimulate the direct transfer of electrons when the aqueous medium is nejayote. The GAC promotes the DIET mechanism, increasing the consumption of organic matter and AGV, increasing the methane production rate and significantly reducing the lag phase. This study represents a precedent for understanding the syntrophic interactions between the species of anaerobic microorganisms, type of residual water, and conductive material. Future research is proposed to promote the generation of alternative energy sources and establish sustainable treatment strategies, even in complex waters, such as nejayote.

IV. REFERENCES

[1] Secretaría de Agricultura y Desarrollo Rural, S. (s. f.). *Maíz, cultivo de México*. (2023). https://www.gob.mx/agricultura/articulos/maiz-cultivo-de-mexico#:~:text=Cultivo%20de%20ma%C3%ADz%20en%20M%C3%A9xico,los%2032%20estados%20del%20pa%C3%ADs.

[2] Quintero-Herrera S., Rueda Avellaneda J., Zwolinski P., Evrard D., Rivas-García P. (2023). Towards a cleaner Mexican tortilla industry: a prospective life cycle assessment approach, Procedia CIRP, Volume 116, 2023, Pages 504-509, ISSN 2212-8271, https://doi.org/10.1016/j.procir.2023.02.085.

[3] M. v. Espejel-García, J.S. Mora-Flores, J.A. García-Salazar, S. Pérez Elizalde, R. García-Mata, Caracterización del consumidor de tortilla en el Estado de México, Agricultura Sociedad y Desarrollo. 13 (2016) 371. https://doi.org/10.22231/asyd.v13i3.401.

[4] Valenzuela E., Gutiérrez-Uribe J., Franco-Morgado M., Cervantes-Avilés P. (2024). Navigating the waters of nixtamalization: Sustainable solutions for maize-processing wastewater treatment, Science of The Total Environment, Volume 911, 2024, 168674, ISSN 0048-9697, https://doi.org/10.1016/j.scitotenv.2023.168674.

[5] Paredes López, O., Guevara Lara, F., & Bello Pérez, L. A. (2010). La nixtamalización y el valor nutritivo del maíz. Ciencias, 92(092). Recuperado a partir de https://www.revistas.unam.mx/index.php/cns/article/view/14831.

[6] Teresa Zayas, Alejandra de Gante, María Guadalupe Tenorio Arvide, Miriam Vega Hernández, Guillermo Soriano-Moro, Leonardo Salgado, Treatment of nixtamalization wastewater (nejayote) using electrocoagulation and combined chemical coagulation/electrocoagulation processes, Desalination and Water Treatment, Volume 280, 2022, Pages 44-51, ISSN 1944-3986, https://doi.org/10.5004/dwt.2022.29113.

[7] Martínez-Bustos, F., Martínez-Flores, H. E., Sanmartín-Martínez, E., Sánchez-Sinencio, F., Chang, Y. K., Barrera-Arellano, D., & Rios, E. (2001). Effect of the components of maize on the quality of masa and tortillas during the traditional nixtamalisation process. Journal of the Science of Food and Agriculture, 81(15), 1455–1462. https://doi.org/10.1002/jsfa.963

[8] Velasco-Martinez M, Angulo O, Vazquez-Couturier DL, Arroyo-Lara A, Monroy-Rivera JA. Effect of dried solids of nejayote on broiler growth. Poult Sci. 1997 Nov;76(11):1531-4. https://doi.org/10.1093/ps/76.11.1531.

[9] Salmerón-Alcocer, A., Rodríguez-Mendoza, N., Pineda-Santiago, V., Cristiani-Urbina, E., Juárez-Ramírez, C., Ruiz-Ordaz, N., & Galíndez-Mayer, J. (2003). Aerobic treatment of maize-processing wastewater (nejayote) in a single-stream multi-stage bioreactor. *Journal of Environmental Engineering and Science*, 2(5), 401-406. https://doi.org/10.1139/s03-046

[10] Díaz-Montes, E., Castro-Muñoz, R., & Yáñez-Fernández, J. (2016). An overview of nejayote, a nixtamalization by product. *Ingeniería Agrícola y Biosistemas*, 8(2), 41-60. https://doi.org/10.5154/r.inagbi.2016.03.002

[11] España-Gamboa, E., Domínguez-Maldonado, J.A., Tapia-Tussell, R. et al. Corn industrial wastewater (nejayote): a promising substrate in Mexico for methane production in a coupled system (APCR-UASB). *Environ Sci Pollut* Res 25, 712–722 (2018). https://doi.org/10.1007/s11356-017-0479-z

[12] Román-Escobedo, L.C.; Cristiani-Urbina, E.; Morales-Barrera, L. Bioremediation with an Alkali-Tolerant Yeast of Wastewater (Nejayote) Derived from the Nixtamalization of Maize. Fermentation 2024, 10, 219. https://doi.org/10.3390/fermentation10040219

[13] Meraz, K. A. S., Vargas, S. M. P., Maldonado, J. T. L., Bravo, J. M. C., Guzman, M. T. O., & Maldonado, E. A. L. (2016). Eco-friendly innovation for nejayote coagulation–flocculation process using chitosan: Evaluation through zeta potential measurements. Chemical Engineering Journal, 289, 536-542. https://doi.org/10.1016/j.cej.2015.09.026.

[14] Khanh Nguyen, V., Kumar Chaudhary, D., Hari Dahal, R., Hoang Trinh, N., Kim, J., Chang, S. W., … Nguyen, D. D. (2021). Review on pretreatment techniques to improve anaerobic digestion of sewage sludge. *Fuel*, 285, 119105. https://doi.org/10.1016/j.fuel.2020.119105

[15] Campos-Flores, R.C.; Reyna-Gómez, L.M.; Suárez-Vázquez, S.I.; Robledo-Olivo, A.; Cruz-López, A. Effect of Inoculum Pretreatment and Operational Mode of Reactor on BioH2 Production from Nixtamalization (Nejayote) and Abattoir Wastewater. Waste Biomass Valor. 2023, 15, 2145–2158.

[16] Rotaru AE, Shrestha PM, Liu F, et al (2014) Direct interspecies electron transfer between Geobacter metallireducens and Methanosarcina barkeri. Appl Environ Microbiol 80:4599–4605. https://doi.org/10.1128/AEM.00895-14

[17] Fang, Z., Huang, Y., Tang, S. et al. Direct interspecies electron transfer for environmental treatment and chemical electrosynthesis: A review. Environ Chem Lett 22, 3107–3133 (2024). https://doi.org/10.1007/s10311-024-01774-8

[18] Kato S, Hashimoto K, Watanabe K (2012) Methanogenesis facilitated by electric syntrophy via (semi)conductive iron-oxide minerals. Environ Microbiol 14:1646–1654. https://doi.org/10.1111/j.1462-2920.2011.02611.x

[19] Burboa Charis, V. A., Orrantia López, M., & Alvarez Valencia, L. H. (2023). Electron transfer via conductive materials and their impact on the anaerobic methane production. *Entreciencias: Diálogos En La Sociedad Del Conocimiento*, 11(25), 1–17. DOI: https://doi.org/10.22201/enesl.20078064e.2023.25.85046

[20] Armenta MA, Maytorena VM, Buentello-Montoya DA, Arroyo E, Cota-Leal M, Yong D, et al. Effect of catalytic hydrodynamics over microagglomerates of Mn2O3 and PdO supported on γ-χ-Al2O3 for dimethyl ether production. *Fuel* 2022;317: 123509.

[21] Lin CY, Lay CH. Effects of carbonate and phosphate concentrations on hydrogen production using anaerobic sewage sludge microflora. Int J Hydrogen Energy. 2004;29(3):275-281. https://doi.org/10.1016/j.ijhydene.2003.07.002

[22] Argun, M. S., & Argun, M. E. (2017). Treatment and alternative usage possibilities of a special wastewater: Nejayote. *Journal of Food Process Engineering*, 41(1), e12609. https://doi.org/10.1111/jfpe.12609

[23] Wang S, Yuan R, Liu C, Zhou B. Effect of Fe2+ adding period on the biogas production and microbial community distribution during the dry anaerobic digestion process. *Process Saf Environ Prot*. 2020 Jan 1;136:234–41. https://doi.org/10.1016/j.jenvman.2022.116783

[24] Zhang, W., Wu, S., Guo, J., Zhou, J., & Dong, R. (2015). *Performance and kinetic evaluation of semi-continuously fed anaerobic digesters treating food waste: Role of trace elements. Bioresource Technology, 178, 297–305.* https://doi.org/10.1016/j.biortech.2014.08.046

[25] Wei, Q., Zhang, W., Guo, J., Wu, S., Tan, T., Wang, F., & Dong, R. (2014). *Performance and kinetic evaluation of a semi-continuously fed anaerobic digester treating food waste: Effect of trace elements on the digester recovery and stability. Chemosphere, 117, 477–485.* https://doi.org/10.1016/j.chemosphere.2014.08.060

[26] Orrantia, Miriam, Armenta, M.A., Alvarez, Luis H., Burboa-Charis, Vianey A.,Meza-Escalante, Edna R., Olivas, A., Arroyo, E., Maytorena, V.M. (2024). Enhanced methane production via anaerobic digestion assisted with Fe3O4 nanoparticles supported on microporous granular activated carbon, *Fuel*, Volume 360,130517, ISSN 0016-2361, https://doi.org/10.1016/j.fuel.2023.130517.

[27] Jiaji Sun, Eldon R. Rene, Yuhe He, Weifang Ma, Qian Hu, Bin Qiu (2023). Carbon, iron, and polymer-based conductive materials for improving methane production in anaerobic wastewater treatment systems: A review on their direct interspecific electron transfer mechanism, Fuel, Volume 342, 2023, 127703, ISSN 0016-2361, https://doi.org/10.1016/j.fuel.2023.127703.

[28] Watanabe, K. (2008) Recent Developments in Microbial Fuel Cell Technologies for Sustainable Bioenergy. Journal of Bioscience and Bioengineering, 106(6), 528–536. [online] http://dx.doi.org/10.1263/jbb.106.528.

[29] Pham, T. H., Aelterman, P., & Verstraete, W. (2009). *Bioanode performance in bioelectrochemical systems: recent improvements and prospects. Trends in Biotechnology, 27(3), 168–178.* https://doi.org/10.1016/j.tibtech.2008.11.005

[30] Gulizhaer Abulikemu, David G. Wahman, George A. Sorial, Mallikarjuna Nadagouda, Eva K. Stebel, Erika A. Womack, Samantha J. Smith, Eric J. Kleiner, Brooke N. Gray, Rose D. Taylor, Cameron X. Gastaldo, Jonathan G. Pressman, Role of grinding method on granular activated carbon characteristics, Carbon Trends, Volume 11, 2023, 100261, ISSN 2667-0569, https://doi.org/10.1016/j.cartre.2023.100261.

[31] Zhao, Z., Li, Y., Quan, X., & Zhang, Y. (2017). Towards engineering application: Potential mechanism for enhancing anaerobic digestion of complex organic waste with different types of conductive materials. Water Research, 115, 266–277. https://doi.org/10.1016/j.watres.2017.02.067

[32] Gahyun Baek, Jinsu Kim, Changsoo Lee, A review of the effects of iron compounds on methanogenesis in anaerobic environments, Renewable and Sustainable Energy Reviews, Volume 113, 2019, 109282, ISSN 1364-0321, https://doi.org/10.1016/j.rser.2019.109282.

[33] Molnar, L., & Bartha, I. (1989). Factors influencing solid-state anaerobic digestion. Biological Wastes, 28(1), 15-24. https://doi.org/10.1016/0269-7483(89)90045-1

[34] LIU, C., YUAN, X., ZENG, G., LI, W., & LI, J. (2008). Prediction of methane yield at optimum pH for anaerobic digestion of organic fraction of municipal solid waste. Bioresource Technology, 99(4), 882–888. https://doi.org/10.1016/j.biortech.2007.01.013

[35] Xu, S., He, C., Luo, L., Lü, F., He, P. y Cui, L. (2015). Comparing Activated Carbono f Different Particle Sizes on Enhancing Methane Generation in Upflow Anaerobic Digester. Bioresource Technology, 196. 606-612. http://dx.doi.org/10.1016/j.biortech.2015.08.018.

[36] Peng, H., Zhang, Y., Tan, D., Zhao, Z., Zhao, H., & Quan, X. (2018). Roles of magnetite and granular activated carbon in improvement of anaerobic sludge digestion. Bioresource Technology, 249, 666–672. https://doi.org/10.1016/j.biortech.2017.10.047

[37] Lee, J., Lee, S., and Park, H. (2016) Bioresource Technology Enrichment of specific electro-active microorganisms and enhancement of methane production by adding granular activated carbon in anaerobic reactors. BIORESOURCE TECHNOLOGY, 205, 205–212. [online] http://dx.doi.org/10.1016/j.biortech.2016.01.054.

[38] Yang Y, Zhang Y, Li Z, et al (2017) Adding granular activated carbon into anaerobic sludge digestion to promote methane production and sludge decomposition. J Clean Prod 149:1101–1108. https://doi.org/10.1016/J.JCLEPRO.2017.02.156

[39] Bhatt, A. H., & Tao, L. (2020). Economic Perspectives of Biogas Production via Anaerobic Digestion. Bioengineering, 7(3), 74. https://doi.org/10.3390/bioengineering7030074

[40] Mou, A., Yu, N., Yang, X., & Liu, Y. (2024). Enhancing methane production and organic loading capacity from high solid-content wastewater in modified granular activated carbon (GAC)-amended up-flow anaerobic sludge blanket (UASB). *Science of the Total Environment*, 906, 167609. https://doi.org/10.1016/j.scitotenv.2023.167609

[41] Gallert, C., and Winter, J. 2008. Propionic acid accumulation and degradation during restart of a full-scale anaerobic biowaste digester. *Bioresour. Technol.* 99(1): 170–178. https://doi.org/10.1016/j.biortech.2006.11.014.

ENFOQUE UTE REVISTA
Facultad Ciencias de la Ingeniería e Industrias

RESEARCH ARTICLE

ENFOQUE UTE, VOL. 16, NO. 3, pp. 44-51, E-ISSN: 1390-6542
RECEIVED APRIL 4, 2025; ACCEPTED MAY 29, 2025; PUBLISHED ONLINE JULY 1, 2025;
DATA OF CURRENT VERSION JULY 1, 2025; PUBLISHED IN VOLUME 16, ISSUE 3 (JULY 2025).

Development and physical-chemical and microbiological characterization of a yogurt-like product, lupine (*Lupinus mutabilis Sweet*) -based

Monserrath Vásquez[1*], Clara Villacrés[2], María Morales[3], Josué Cruz[4]

***Abstract* —In view of the growing demand for alternatives to animal products, this study presents the development and physicochemical, microbiological and sensory characterization of a yogurt-type product based on lupine milk (*Lupinus mutabilis*) and starch from arracacha (*Arracacia xanthorrhiza*). Three versions of the product were formulated with different concentrations of starch, evaluating its proximal composition, polyphenol content, rheological behavior, microbiological profile and sensory acceptance. The results showed that the incorporation of starch did not significantly affect the basic nutritional composition, maintaining an adequate protein and fiber profile. The formulation with 3 % starch (T3) presented higher viscosity, rheological stability and sensory acceptability analysis, standing out in attributes such as flavor, texture and appearance. In addition, the pseudoplastic behavior observed suggests a favorable texture for the consumer. At the microbiological level, all formulations met safety standards, showing an adequate presence of lactic acid bacteria with probiotic potential. Therefore, this work not only highlights the potential of lupin as a base for functional fermented products but also highlights the importance of arracacha starch as a natural stabilizer. The findings open new perspectives for the development of innovative, sustainable and nutritionally balanced plant-based foods, with projection towards the food industry and the growing market of vegan and food intolerant consumers.**

***Keywords:* milk-like; yogurt-like; Arracacia xanthorrhiza; Lupinus mutabilis Sweet; lactic acid bacteria.**

***Resumen* — Ante la creciente demanda de alternativas a productos de origen animal, este estudio presenta el desarrollo y caracterización fisicoquímica, microbiológica y sensorial de un producto tipo yogurt a base de leche de lupino (*Lupinus mutabilis*) y almidón de arracacha (*Arracacia xanthorrhiza*). Se formularon tres versiones del producto con diferentes concentraciones de almidón, evaluando su composición proximal, contenido de polifenoles, comportamiento reológico, perfil microbiológico y análisis de aceptabilidad sensorial. Donde los resultados evidenciaron que la incorporación de almidón no afectó significativamente la composición nutricional básica, manteniendo un perfil proteico y de fibra adecuado. La formulación con 3 % de almidón (T3) presentó mayor viscosidad, estabilidad reológica y aceptabilidad sensorial, destacándose en atributos como sabor, textura y apariencia. Además, el comportamiento pseudoplástico observado sugiere una textura favorable para el consumidor. A nivel microbiológico, todas las formulaciones cumplieron con los estándares de inocuidad, mostrando una adecuada presencia de bacterias ácido-lácticas con potencial probiótico. Teniendo que este trabajo no solo destaca el potencial del lupino como base para productos fermentados funcionales, sino que también resalta la importancia del almidón de arracacha como estabilizante natural. Los hallazgos abren nuevas perspectivas para el desarrollo de alimentos vegetales innovadores, sostenibles y nutricionalmente balanceados, con proyección hacia la industria alimentaria y el mercado creciente de consumidores veganos y con intolerancias alimentarias.**

***Palabras Clave:* parecido a la leche, parecido al yogur, Arracacia xanthorrhiza; Lupinus mutabilis Sweet; bacterias ácido – lácticas.**

* *Corresponding autor:* monserrath.vasquez9366@utc.edu.ec
1. Monserrath Carolina Vásquez Rodríguez is with Universidad Técnica de Cotopaxi, Latacunga, Ecuador P.O. Box 050103, Latacunga, Ecuador. E-mail: monserrath.vasquez9366@utc.edu.ec, ORCID number https://orcid.org/0009-0001-6306-5069
2. Clara Elena Villacrés Poveda is with Instituto Nacional de Investigaciones Agropecuarias, INIAP, Quito, Ecuador INIAP, P.O. Box 17 0518, Mejía, Ecuador. E-mail: elena.villacres@iniap.gob.ec, ORCID number https://orcid.org/0000-0001-9660-5845
3. María Monserrath Morales-Padilla is with Unidad Académica de Posgrado, Universidad Técnica de Cotopaxi, Latacunga - Ecuador P.O. Box 050103, Latacunga, Ecuador. E-mail: maria.morales1144@utc.edu.ec, ORCID number https://orcid.org/0000-0001-9048-1538
4. Josué David Cruz Vasquez is with Universidad Técnica de Ambato, Ambato, Ecuador. E-mail: jcruz9670@uta.edu.ec, ORCID number https://orcid.org/0009-0000-4687-852X

DOI: https://doi.org/10.29019/enfoqueute.1164
Associate Editor: *Carlota Martina Moreno*

I. INTRODUCTION

THE rejection of animal-derived products has increased notably in recent years, a trend closely associated with veganism—a dietary practice that excludes all animal-origin foods, including dairy, honey, and eggs [1]. The number of individuals identifying as vegans continues to grow, driven by motivations such as improving health and avoiding animal cruelty. Within this context, plant-based dairy alternatives have gained significant attention due to their suitability for individuals with allergies, lactose intolerance, or those transitioning to a vegan lifestyle [2].

A parallel rise in the adoption of healthier lifestyles has led consumers to seek out plant-based and functional food options [3]. Among these, plant-based yogurts stand out due to their low cholesterol content and their suitability for individuals with protein allergies or lactose intolerance [4]. Moreover, these yogurts retain high levels of probiotics and bioactive peptides, which enhance their nutritional value [2]. The texture and nutritional profile of such products depend significantly on the type of plant-based milk used (e.g., legumes or cereals) and on complementary ingredients such as starch and fiber [1]. As a result, the food industry has increasingly focused on developing plant-based functional foods that promote consumer health [5].

However, studies on plant-based yogurt alternatives have faced several limitations. Some formulations derived from legumes such as soy, pea, or oat often struggle to achieve desirable sensory attributes, particularly in terms of flavor, texture, and aroma, most notably the presence of off-flavors and insufficient creaminess [6]. Furthermore, the low gelling capacity of plant proteins compared to dairy proteins has led to the addition of stabilizers or texture enhancers, which can sometimes compromise the natural or clean-label appeal of the products [7]. Another common limitation has been the variability in the growth of probiotic cultures in non-dairy matrices, which can affect the viability and stability of probiotics over the shelf-life of the products [8], [9]. Also considering that few studies have explored the use of alternative starches such as arracacha (*Arracacia xanthorrhiza*) to improve texture, focusing predominantly on more commonly available sources such as corn or potato starch [10], [11]. These limitations highlight the need for further research into novel plant-derived matrices and stabilizers that can improve the physicochemical, microbiological and sensory qualities of yogurt-like products without compromising their nutritional profile or clean-label appeal [7], [12].

For this reason, the formulation of plant-based yogurts requires the selection of legumes with high protein content. Among these, lupine (*Lupinus spp.*) stands out for its exceptional protein concentration, ranging between 40 and 50 g/100 g dry weight [13]. Although the genus Lupinus includes nearly 300 species, only four are of major agricultural significance: *L. albus*, *L. angustifolius*, *L. luteus*, and *L. mutabilis*. The latter is particularly noteworthy for its high protein content, adaptability to agricultural systems, and potential health benefits [14]. According to the [15], lupine contains approximately 51 % protein, 21.9 % fat, 13 % fiber, 3.23 % alkaloids, 0.37 % calcium, 0.6 % iron, and 0.3 % zinc. However, due to its elevated alkaloid content, it must be subjected to heat treatment to reduce these compounds and minimize the risk of toxicity [1].

Lupine proteins include heat-stable globulins such as α-conglutin (11S legumin-type) and β-conglutin (7S vicilin-type). The denaturation of β-conglutin begins at 85-89 °C, while α-conglutin remains stable up to 102-105 °C. Under high temperatures and isoelectric pH, these globular proteins unfold due to the disruption of hydrogen bonds and hydrophobic interactions, leading to the formation of protein aggregates. These can bind to albumins, which possess excellent interfacial properties, contributing to foam formation and reduced interfacial tension [4], [16]. Heat and bacterial proteolysis further induce structural changes such as denaturation, dissociation, and aggregation, enhancing the yogurt's structural, functional, and nutritional characteristics [17]. Nevertheless, lupine has inherently weak gelling properties, which is why starch is often added to improve mouthfeel, viscosity, creaminess, reduce syneresis, and enhance gel firmness [18].

Therefore, the objective of this study was to develop a yogurt-like product based on lupine milk and *Arracacia* starch as an alternative to traditional dairy products, and to evaluate its physicochemical, microbiological, and sensory characteristics.

II. MATERIALS AND METHODS

A. Materials

Commercial lupine grain of the INIAP-450 variety was purchased from the Gralyn farm in Latacunga, Ecuador. *Arracacia xanthorrhiza* starch was provided by the Plant Genetic Resources Department of INIAP-Ecuador. Danisco (*Streptococcus thermophilus* and *Lactobacillus delbrueckii* subsp. *bulgaricus*) and sucrose were purchased from the chemist's house in Latacunga, Ecuador.

B. Lupine debittering

The lupine grains were debittered using aqueous heat processing as previously reported [19]. Briefly, grains were immersed in hot water (80 ◦C) at a 1:3 ratio (grain:water) for 10 h, then cooked at 91 ◦C for 1 h and thoroughly washed at 35 ◦C for 28 h with continuous changing of distilled water.

C. Milk-like product processing

In the preparation of the lupine-based milk product, the grain previously free of bitterness was used, which was ground in a colloid mill (Wenzhou Maolong Machinery Co., Ltd, China) applying a water:grain ratio of 1:4 w/v [20].

D. Yogurt-like product, lupin-based processing

For yogurt-like processing, a milk-like lupin base (1.84 % fat w/w) was used. Preliminary trials were conducted to define the inclusion levels of *A. xanthorrhiza* starch in yogurt-like product and the following test formulations were established: T1= (90.7 % milk-like, 1 % *A. xanthorrhiza* starch, 8 % sucrose, 0.3 % Danisco strain), T2= (89.7 % milk-like, 2 % *A. xanthorrhiza* starch, 8 % sucrose, 0.3 % Danisco strain) and T3= (88.7 % milk-like, 3 % *A. xanthorrhiza* starch, 8 % sucrose, 0.3 % Danisco strain).

All three formulations were pasteurized at 70 °C for 30 minutes and then cooled to 40 °C. They were then incubated at 40 °C ± 2 °C for 10 to 12 hours in an incubator (Memmert, Germany) until the pH was adjusted to a range of 4.4 to 4.6. To stop the fermentation process, the yogurts were removed from the incubator and stored under refrigeration at 4 °C.

E. Proximal analysis

Methodologies of the AOAC were used to assess moisture (930.15), crude protein (total N x 6.25) (955.39), crude fat

(920,39), crude fiber (978.10), and ash (942.05). The total carbohydrate content of the samples was calculated by the difference method (subtracting the percent crude protein, crude fiber, crude fat, and ash from 100 %), [21]. The energy content was determined by applying the method described by [22].

F. Polyphenols

The total phenolic content was determined using the Folin Ciocalteu 2N reagent. The absorbance was measured at 754 nm using an Evolution 201 spectrophotometer (Cachay-Morante *et al*., 2022) (Thermo Fisher Scientific, Massachusetts, USA), and the results are expressed in mg of gallic acid/100 g of dry sample [23].

G. pH and titratable acidity

During fermentation, standard methodologies of the Association of Official Analytical Chemical International were used to assess pH (943.02) and total titratable acidity (947.05) [24]. The pH value and total titratable acidity were determined using 10 mL of samples which were suspended in 90 mL distilled water and stirred for 10 min. The pH was measured using a pH electrode, and total titratable acidity was expressed as the amount (mL) of 0.01 mol.L^{-1} NaOH required to obtain a pH value of 8.2, and the result is reported as lactic acid percentage.

H. Viscosity

Measurements of viscosity were done with Brookfield (model DV II; Brookfield Engineering Laboratories, Stoughton, MA 02072, USA) with Helipath stand, a type D T-bar spindle and a speed of 5 rpm. The Brookfield measurements were performed in triplicate and the mean values used for further analysis were reported. All rheological measurements were made at 5 °C Spindle No 2 from 0 to 200 rpm was used for all samples, as described by [25].

I. Rheological

From the viscosity values obtained using the Brookfield viscometer (model DV II; Brookfield Engineering Laboratories, Stoughton, MA, USA), mathematical modeling was performed using the power law equation [19].

The data obtained were adjusted to the following equation:

$$\eta = K\gamma^n \quad (1)$$

Where:
η: shear stress (Pa).
γ: shear rate (1/s).
K: fluid consistency index (Pa.sn).
n: flow behavior index.

This model allowed us to characterize the relationship between shear stress and shear rate, determining whether the yogurt exhibited pseudoplastic, dilatant, or Newtonian behavior.

J. Microbiological Analysis

Microorganism enumeration was performed using the rapid Petrifilm methods (3M). A dilution of each sample was made by adding 10 g of yogurt to 90 ml of distilled water. In all cases, 1 ml of the dilution was inoculated in duplicate and incubated at 25 °C for 48 h for molds and yeasts (AOAC Method 997.02) and 35 °C for 24 h for E. coli/total coliforms (AOAC Method 991.14). At the end of the incubation, plates with between 15 and 150 colonies were selected, and the result was reported as colony-forming units per gram (CFU/g). Microbiological quality was assessed by comparing the results with the requirements established in the Ecuadorian Technical Standard INEN 2395 for Fermented Milks [27].

K. Sensory acceptability analysis

Sixty consumers between 18 and 60 years of age [28], all habitual yogurt consumers, were randomly recruited through advertisements at various locations on the campus of Cotopaxi University, La Maná, Ecuador. They were invited to participate in an acceptance test for four yogurt-like products with different concentrations of *Arracacia* starch. Each sample contained 20 mL and was presented monadically in coded plastic cups in a randomized order. First-order and carryover effects were balanced using a Randomized Complete Block Design, where each consumer evaluated all yogurt-like samples. The test was conducted under controlled conditions, with water and crackers available to consumers. 9-point hedonic scale (1 – extremely disliked, 2 – very disliked, 3 – moderately disliked, 4 – slightly disliked, 5 – neither liked nor disliked, 6 – slightly liked, 7 – moderately liked, 8 – very liked, and 9 – extremely liked) [29]. Results were subjected to one-way analysis of variance (ANOVA) to identify contrasts between yogurt samples, followed by Tukey's test with a significance level of 5.00 %.

L. Statistical analysis

All analyses were performed in triplicate; results are expressed as mean ± standard deviation. Data were analyzed using a multivariate ANOVA using the INFOSTAT statistical package (University of Córdoba, Argentina) to compare means with respect to the level of *Arracacia* starch incorporation. Tukey's multiple-range test was applied to determine significant differences at the 5 % level. For the rheological component, Python was used, using the numpy and matplotlib libraries.

III. RESULTS AND DISCUSSION

A. Proximal Analysis

A significant difference in moisture content was observed between the milk-like product made from *Lupinus mutabilis* and the three formulations containing *Arracacia xanthorrhiza* starch ($p \leq 0.05$). The milk-like product showed the highest moisture percentage (92.20 %), which can be attributed to the natural moisture of lupin and the addition of water during processing. In contrast, moisture content decreased progressively with increasing starch concentration, with formulation T3 exhibiting the lowest value (85.59 %). Regarding protein, fat, and energy content, no significant differences were found ($p \geq 0.05$) between the starch-containing formulations and the milk-like product, suggesting that the inclusion of *Arracacia* starch did not substantially alter these parameters. Ash content was higher in treatment T1 (90.7 % compared to the milk-like product, with 1 % *Arracacia xanthorrhiza* starch, 8 % sucrose, and 0.3 % Danisco culture), although the difference was not statistically significant ($p \geq 0.05$) when compared to formulations T2 and T3. This trend may be related to the mineral contribution of *Arracacia* starch. Similarly, crude fiber content did not show significant differences ($p \geq 0.05$) among the three treatments. These results are consistent with those reported by [30], in studies of plant-based yogurts enriched with starch.

TABLE I
PROXIMAL COMPOSITION AND POLYPHENOL CONTENT OF A MILK-LIKE PRODUCT, AND THREE FORMULATIONS OF YOGURT-LIKE PRODUCTS, LUPINE-BASED

	Milk-like	**T1**	**T2**	**T3**
Moisture (%)	92.20 ± 0.066^{a}	86.58 ± 0.037^{b}	86.77 ± 0.143^{b}	85.59 ± 0.042^{c}
Protein (%)	2.40 ± 0.061^{a}	2.39 ± 0.225^{a}	2.65 ± 0.130^{a}	2.71 ± 0.060^{a}
Fat (%)	1.84 ± 0.050^{a}	1.76 ± 0.027^{a}	1.83 ± 0.009^{a}	1.88 ± 0.001^{a}
Crude fiber (%)	2.66 ± 0.050^{a}	2.12 ± 0.012^{b}	2.15 ± 0.015^{b}	2.25 ± 0.023^{b}
Ash (%)	0.03 ± 0.005^{b}	0.05 ± 0.001^{a}	0.04 ± 0.005^{ab}	0.04 ± 0.004^{ab}
Carbohydrates (%)	7.09 ± 0.227^{ab}	7.08 ± 0.227^{ab}	6.51 ± 0.022^{b}	7.54 ± 0.100^{a}
Energy (kcal)	59.83 ± 1.694^{a}	58.04 ± 0.257^{a}	57.75 ± 0.601^{a}	62.19 ± 0.367^{a}
Polyphenols (mg gallic acid /100 mL)	3.17 ± 0.386^{b}	3.09 ± 0.468^{b}	3.67 ± 0.328^{a}	3.46 ± 0.36^{8a}b

Different letters in the same row indicate significant differences ($p \leq 0.05$). Mean value ± SD (n-3) T1= (90.7 % milk-like, 1% *Arracacia xanthorrhiza* starch, 8 % saccharose, 0.3 % Danisco starter), T2= (89.7 % milk-like, 2% *Arracacia xanthorrhiza* starch, 8 % saccharose, 0.3 % Danisco strain) and T3 = (88.7 % milk-like, 3 % *Arracacia xanthorrhiza* starch, 8 % saccharose, 0.3 % Danisco strain).

B. Polyphenols

The concentration of total phenolic compounds (Table I) in the yogurt-like samples ranged from 3.09 to 3.67 mg gallic acid/100 mL, starting from 3.17 mg/100 mL of milk-type, lupine-based. These results are in agreement with those mentioned by [31] for legume-based fermented products and plant-based fermented beverages, in which they reported 2.8- 4.2 mg gallic acid/100 mL. They indicate that in legumes, many polyphenols are bound to fiber or other macromolecules.

The enzymatic action of microorganisms during fermentation can break these bonds and release polyphenols, increasing their concentration in the final product, [31].

Formulation T2 showed the highest concentration of polyphenols (3.67 mg gallic acid/100 mL), which could be associated with the action of lactic acid bacteria (LAB) used in fermentation, these metabolize certain compounds present in lupine and produce new polyphenols or modify existing ones, improving their bioavailability and antioxidant activity, as reported by [32] in yogurts with functional ingredients. Meanwhile, the T3 formulation (3.46 mg of gallic acid/100 mL) presented a value lower than T2, this difference can be attributed to the higher starch content in its composition. The elevated presence of starch promotes the formation of strong starch–polyphenol interactions, which affect the bioaccessibility of these compounds. As a result, there is a slight decrease in the number of free polyphenols available for detection in the analysis [33]. However, no significant differences ($p \geq 0.05$) were found between T2 and T3, suggesting that although the numerical values vary, the changes in polyphenol concentration between these treatments are not statistically relevant. On the other hand, the lowest concentration (3.09 mg gallic acid/100 mL) showed by T1 formulation, may be due to the lower starch content in the formulation. According [26] the contribution of polyphenols to the formulation is 5.51 mg Trolox Eq./g. These results highlight the importance of optimizing the formulation to increase the content of bioactive compounds in yogurts.

C. pH and titratable acidity variation

The pH decreased progressively with the fermentation time of milk-like product, while the acidity presented an increase, as evidenced in Figures 1 and 2. This behavior was determined from the first time of fermentation, which was attributed to a greater contact area for the growth of microorganisms and their metabolic activity [34]. A decrease in pH is a desirable result for fermentation, because the opposite effect results in the overproduction of ammonia resulting from the decomposition of nitrogen-containing organic compounds [35]. The results are consistent with that reported by [36], who note that pH reduction is associated with the production of lactic acid and other secondary compounds. These secondary products include acetic, butyric and propionic acids, which contribute to pH decrease and acidification of the medium. The variation recorded was significantly ($p \leq 0.05$) dependent on the formulation composition. The greatest difference was observed in the fermentation of T2, with respect to T1 and T3, that showed lower pH between 4-6 h of fermentation.

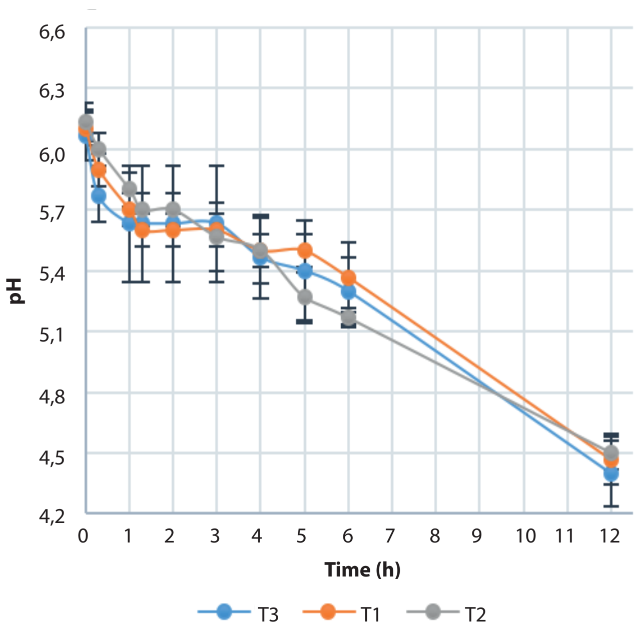

Fig. 1. pH variation with fermentation time of three formulations of yogurt-like products, lupine-based.

T1= (90.7 % milk-like, 1 % *Arracacia xanthorrhiza* starch, 8 % saccharose, 0.3 % Danisco starter), T2= (89.7 % milk-like, 2 % *Arracacia xanthorrhiza* starch, 8 % saccharose, 0.3 % Danisco starter) and T3 = (88.7 % milk-like *Arracacia xanthorrhiza* starch, 8 % saccharose, 0.3 % Danisco starter).

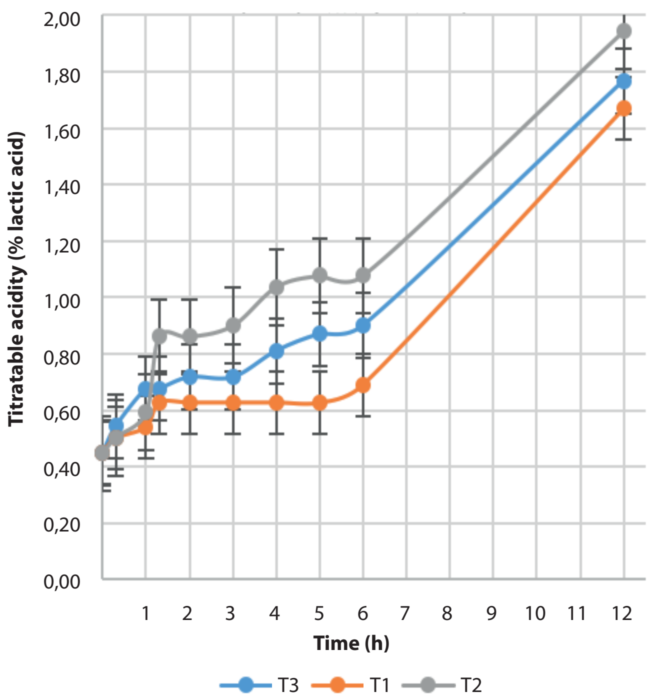

Fig. 2. Titratable acidity variation with fermentation time of three formulations of yogurt-like products, lupine-based.

T1= (90.7 % milk-like, 1 % *Arracacia xanthorrhiza* starch, 8 % saccharose, 0.3 % Danisco starter), T2= (89.7 % milk-like, 2 % *Arracacia xanthorrhiza* starch, 8% saccharose, 0.3 % Danisco starter) and T3 = (88.7 % milk-like, 3 *Arracacia xanthorrhiza* starch, 8 % saccharose, 0.3 % Danisco starter).

D. Rheological Analysis

The results showed that the flow behavior index was less than 1.00, corresponding to non-Newtonian fluid with pseudoplastic behavior, characterized by variations in its viscosity as a function of the shear rate [37] (Table II).

The consistency coefficient (K) in fluid rheology is a parameter of the power law model (Ostwald-de Waele model) that describes the behavior of non-Newtonian fluids [35]. The (k) value experienced an increased as the content of *Arracacia* starch in the formulation increased, which suggests that (K) depends on the chemical composition and molecular structure of the yogurt-like product. These results agree with those reported by [37], when observed that the consistency coefficient (k) increased with the banana powder content in soy yogurt, attributing this trend to the effect of total soluble solids. [38], after analyzing 270 yogurt samples, concluded that the addition of starch increased the consistency coefficient and the character pseudoplastic behavior of these products.

TABLE II
FLOW BEHAVIOR INDEX AND CONSISTENCY COEFFICIENT* OF THREE FORMULATIONS OF YOGURT-LIKE PRODUCTS, LUPINE-BASED

Formulation	Consistency coefficient (k) (Pa.sn)	Flow behavior index (n)	Correlation coefficient
T1	1059.97	-2.11	1
T2	1414.82	0.68	0.999
T3	199.05	0.56	0.998

*According to Waele's Ostwald power law model. T1= (90.7 % milk-like, 1 % *Arracacia xanthorrhiza* starch, 8 % saccharose, 0.3 % Danisco strain), T2= (89.7 % milk-like, 2 % *Arracacia xanthorrhiza* starch, 8% saccharose, 0.3 % Danisco strain) and T3 = (88.7 % milk-like, 3 *Arracacia xanthorrhiza* starch, 8 % saccharose, 0.3 % Danisco strain).

As observed in Figure 3, the apparent viscosity was significantly higher ($p \leq 0.05$) in the yogurt-like product with 3 % starch and lower in the formulation with 1 % *Arracacia* starch. This behavior is due to the increase in solids, which could have generated more interactions between particles and molecules, increasing resistance to flow and viscosity. Additionally, as the proportion of starch increases, its capacity for hydration too increases. In this manner, the gelatinized starch contributes to the formation of a denser and more stable matrix, enhancing consistency, reducing phase separation, and increasing the viscosity of the product [39]. It was also observed that increasing shear stress (η), the viscosity of yogurt-like products decreased, which is characteristic of systems with pseudoplastic behavior.

In this regard, [40] demonstrated that carrot and Jerusalem artichoke flour, despite its low protein content and high fructose oligosaccharide content, generated a gel with high viscosity. However, it was lower than that obtained with the addition of buckwheat powder, which had a higher protein content.

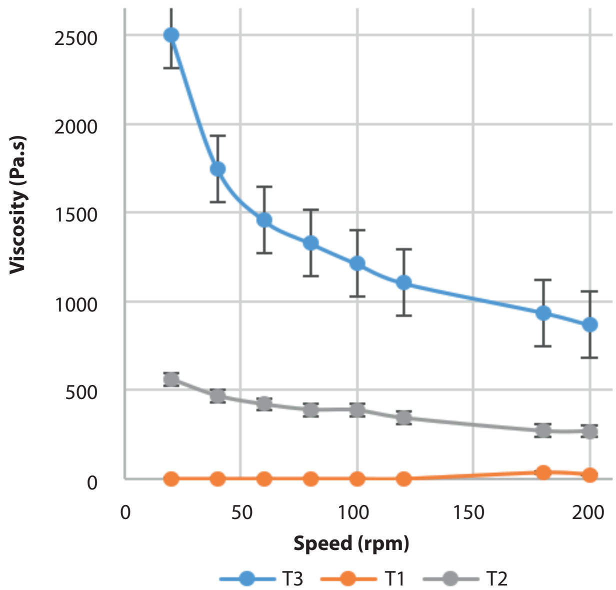

Fig. 3. Viscosity variation with shear rate of three formulations of yogurt-like products, lupin-based.

T1= (90.7 % milk-like, 1% *Arracacia xanthorrhiza* starch, 8 % saccharose, 0.3 % Danisco starter), T2= (89.7 % milk-like, 2 % *Arracacia xanthorrhiza* starch, 8% saccharose, 0.3 % Danisco starter) and T3 = (88.7 % milk-like, 3 % *Arracacia xanthorrhiza* starch, 8 % saccharose, 0.3 % Danisco strain).

E. Microbiological Analysis

During the fermentation process, microorganisms that impair the quality of the yogurt-like products can grow [41]. To ensure that their count was within the permissible limits for consumption, a microbiological analysis was performed, and the results were shown in Table III. These were compared with the [27], which specifies the maximum concentrations of pathogenic microorganisms such as *E. coli*, as well as the minimum content of lactic acid bacteria cultures.

The concentrations of total coliforms, *E. coli*, molds, and yeasts from yogurt-like products did not exceed the permissible levels established by the INEN standard. The low concentration of undesirable microorganisms showed proper sterilization of the materials used to yogurt-like, lupine-based processing and monitoring at each stage of its production. Furthermore, lupin possesses antimicrobial activity, inhibiting *E. coli* strains; this capacity could have contributed to achieving the standards established by the INEN [42].

Changes in *L. bulgaricus* and *S. thermophilus* amounts in the yogurt-like formulations obtained from lupine milk are given in Table III. In the production of non-dairy yogurt-like products from lupine milk, the relationship between the addition of *Arracacia* starch and the growth of starter cultures was found to be significant ($p \leq 0.05$). The sample with 1 % *Arracacia* starch showed a minimal lactic acid bacteria count. In contrast, the samples with 2 and 3 % *Arracacia* starch showed an increased growth and higher activity of starter. [43] reported that a lactic acid bacteria count between 10^7-10^8 ensures the conversion of sugars into lactic acid, lowering of pH, causing protein coagulation, development of flavor, aroma and beneficial probiotic effects for intestinal health; this favors the preservation of yogurt by inhibiting unwanted microbial growth.

TABLE III
MICROBIOLOGICAL COUNT OF THREE FORMULATIONS OF YOGURT-LIKE PRODUCTS, LUPIN-BASED

	T1	T2	T3
Microorganisms		**UFC/g**	
Total coliforms	10	<10	<10
Echerichia Coli	<1	<1	<1
Molds and yeasts	100	67	133
Lactic acid bacteria	$7.9x10^7$	$4.0x10^8$	$1.8x10^8$

T1= (90.7 % milk-like, 1% *Arracacia xanthorrhiza* starch, 8 % saccharose, 0.3 % Danisco strain), T2= (89.7 % milk-like, 2 % *Arracacia xanthorrhiza* starch, 8 % saccharose, 0.3 % Danisco strain) and T3 = (88.7 % milk-like, 3 % *Arracacia xanthorrhiza* starch, 8 % saccharose, 0.3 % Danisco strain).

F. Sensory acceptability analysis

Formulation T3 showed the highest scores in the key attributes color, taste, texture and acceptability, consolidating its position as the consumers' favorite. The higher score in the attribute "acceptability" is relevant because it defines the acceptance or rejection of novel functional foods, since low acceptability can discourage purchase intention [44]. No significant difference was found in the odor attribute, which showed the lowest score (4.93/9.00), suggesting a lower production of aromatic compounds that contribute complexity to the sensory profile with respect to the other sensory attributes. This result could be related to the chemical composition of lupine milk, with a predominance of globular proteins, glutamic acid and aspartic acid [45].

V. CONCLUSION

The results of the proximate analysis showed a favorable nutritional profile, with adequate protein, crude fiber and phenolic compound, comparable to other fermented plant-based products. The formulation with the highest percentage of *Arracacia* starch (T3) showed the mayor rheological stability and viscosity, suggesting that this ingredient not only contributes to texture but may also influence the preservation of yogurt's functional benefits. Microbiological analyses confirmed the presence of lactic acid bacteria at an adequate count, which guarantees the probiotic function of the yogurt for intestinal health.

Sensory analysis showed that (T3) was the best rated by consumers in the attributes and acceptability. This demonstrates the potential of this formulation as an innovative alternative in the yogurt-like, lupine-based range. Consequently, future research could focus on smell optimization and shelf-life analysis for large-scale commercialization.

REFERENCES

[1] M. Soumya, A. Suresh, R. Parameswaran and K. M. Nampoothiri, "Physico-chemical and organoleptic evaluation of probiotic plant-milk yogurt-type beverages as a functional alternative to dairy yogurts," *Biocatal Agric Biotechnol*, vol. 57, no. 103060, p. 103060, 2024. https://doi.org/10.1016/J.BCAB.2024.103060

[2] V. R. Narala, M. A. Jugbarde, I. Orlovs and M. Masin, "Inulin as a prebiotic for the growth of vegan yoghurt culture in pea protein-based vegan yoghurt-ice cream, while improving the textural properties," *Applied Food Research*, vol. 2, no. 2, p. 100136, 2022. https://doi.org/10.1016/J.AFRES.2022.100136

[3] D. Dhakal, G. Kumar, L. Devkota, D. Subedi and S. Dhital, "The choice of probiotics affects the rheological, structural, and sensory attributes of lupin-oat-based yoghurt," *Food Hydrocoll*, vol. 156, no. 5, p. 110353, 2024. https://doi.org/10.1016/J.FOODHYD.2024.110353

[4] D. Dhakal, T. Younas, R. Bhusal, L. Devkota, L. Li, B. Zhang and S. Dhital, "The effect of probiotic strains on the proteolytic activity and peptide profiles of lupin oat-based yoghurt," *Food Hydrocoll*, vol. 149, no. 1, p. 109570, 2024. https://doi.org/10.1016/J.FOODHYD.2023.109570

[5] S. A. Ahmed, W. A. Helmy and O. A. Ibrahim, "Evaluation of lupine seeds (Lupinus albus L.) neutral extract as a texture improver in low-fat yogurt production," *Int J Biol Macromol*, vol. 263, no. 13, p. 130303, 2024. https://doi.org/10.1016/J.IJBIOMAC.2024.130303

[6] L. Hanley, S. Dobson and A. G. Marangoni, "Legume milk-based yogurt mimetics structured using glucono-δ-lactone," *Food Research International*, vol. 184, no. 10, p. 114259, 2024. https://doi.org/10.1016/J.FOODRES.2024.114259

[7] J. Ran, S. Pang, H. Li, R. Zhao, Y. Li and M. Yang, "Gel properties of mung bean protein-sodium caseinate hybrid yogurt: Physicochemical properties, microstructure, and intermolecular interactions," *Food Chem X*, vol. 24, no. 77, p. 101977, 2024. https://doi.org/10.1016/J.FOCHX.2024.101977

[8] T. Pantoa, K. Wadeesirisak, S. Saah and P. Saithong, "In vitro protein digestibility and bioactive activities of yogurt from black soybean (Glycine max L.) milk," *Future Foods*, vol. 11, no. 36, p. 100636, 2025. https://doi.org/10.1016/J.FUFO.2025.100636

[9] Y. Ma, S. H. Lee, M. Guk, S. Cho and Y. Kim, "Enhancing soy yogurt texture and functionality with mealworm protein," *Journal of Food Composition and Analysis*, vol. 141, no. 10, p. 107337, 2025. https://doi.org/10.1016/J.JFCA.2025.107337

[10] M. Caponio *et al.*, "Development, optimization and integrated characterization of rice-based yogurt alternatives enriched with roasted and non-roasted sprouted barley flour," *Curr Res Food Sci*, vol. 10, no. 1, p. 101059, 2025. https://doi.org/10.1016/J.CRFS.2025.101059

[11] X. Wang, L. Wang, X. Wei, C. Xu, G. Cavender, W. Lin and S. Sun, "Invited review: Advances in yogurt development Microbiological safety, quality, functionality, sensory evaluation, and consumer perceptions across different dairy and plant-based alternative sources," *J Dairy Sci*, vol. 108, no. 1, pp. 33-58, 2025. https://doi.org/10.3168/JDS.2024-25322

[12] A. Zeinatulina, K. Tanilas, K. Ehala-Aleksejev, E. Viiard and T. Kriščiunaite, "Digestibility of protein and estimated bioavailability of mineral compounds in plant-based yoghurt alternatives," *Future Foods*, vol. 11, no. 1, p. 100545, 2025. https://doi.org/10.3168/JDS.2024-2532210.1016/J.FUFO.2025.100545

[13] N. C. Jamanca, R. W. Ocrospoma, Y. M. Eguilas, R. A. Padilla and R. J. Silva, "Food grain quality: Analysis of physical, biometric, and colorimetric properties to promote consumption," *Heliyon*, vol. 10, no. 7, p. e29234, 2024. https://doi.org/10.1016/J.HELIYON.2024.E29234

[14] A. Gulisano, S. Alves, J. N. Martins and L. M. Trindade, "Genetics and Breeding of Lupinus mutabilis: An Emerging Protein Crop," *Front Plant Sci*, vol. 10, no. 1, p. 1385, 2019. https://doi.org/ 10.3389/FPLS.2019.01385

[15] FAO, "Simposio Regional del chocho o tarwi (Lupinus mutabilis)," *Organización de las Naciones Unidas para la Alimentación y la Agricultura*, 2016. Accessed: Jun. 27, 2024. [Online]. Available: https://www.fao.org/ecuador/noticias/detail-events/en/c/453499/

[16] L. Devkota, K. Kyriakopoulou, R. Bergia and S. Dhital, "Structural and Thermal Characterization of Protein Isolates from Australian Lupin Varieties as Affected by Processing Conditions," *Foods*, vol. 12, no. 5, p. 908, 2023. https://doi.org/10.3390/foods12050908

[17] J. Yang and L. M. C. Sagis, "Interfacial behavior of plant proteins — novel sources and extraction methods," *Curr Opin Colloid Interface Sci*, vol. 56, no. 1, p. 101499, 2021. https://doi.org/10.1016/J.COCIS.2021.101499

[18] A. Hickisch, R. Beer, R. F. Vogel and S. Toelstede, "Influence of lupin-based milk alternative heat treatment and exopolysaccharide-producing lactic acid bacteria on the physical characteristics of lupin-based yogurt alternatives," *Food Research International*, vol. 84, no. 1, pp. 180-188, 2016. https://doi.org/10.1016/J.FOODRES.2016.03.037

[19] E. Villacrés, P. Cueva, M. Díaz, and C. M. Rosell, "Replacing Wheat Flour with Debittered and Fermented Lupin: Effects on Bread's Physical and Nutritional Features," *Plant Foods for Human Nutrition*, vol. 75, no. 4, pp. 569-575, 2020. https://doi.org/ 10.1007/S11130-020-00844-W/METRICS

[20] G. E. Sedó Molina, R. Shetty, C. Jacobsen, L. Duedahl-Olesen, E. B. Hansen and C. H. Bang-Berthelsen, "Synergistic effect of the coculture of Leuconostoc pseudomesenteroides and Lactococcus lactis, isolated from honeybees, on the generation of plant-based dairy alternatives based on soy, pea, oat, and potato drinks," *Food Microbiol*, vol. 118, no. 3, pp. 104427, 2024. https://doi.org/10.1016/J.FM.2023.104427

[21] AOAC, "Official methods of analysis," *Current througn,* no. 3, pp. 4-5, 2005. Accessed: Mar. 17, 2025. Available: https://www.academia.edu/43245633/Of_fi_cial_Methods_of_Anal_y_sis_of_AOAC_INTER_NA_TIONAL_18th_Edi_tion_2005

[22] Y. Deng, Y. Wang, G. Zhong and X. Yu, "Simultaneous quantitative analysis of protein, carbohydrate and fat in nutritionally complete formulas of medical foods by near-infrared spectroscopy," *Infrared Phys Technol*, vol. 93, no. 2, pp. 124-129, 2018. https://doi.org/10.1016/J.INFRARED.2018.07.027

[23] M. Quiñones, M. Miguel and A. Aleixandre, "Los polifenoles, compuestos de origen natural con efectos saludables sobre el sistema cardiovascular," *Nutr Hosp*, vol. 27, no. 1, pp. 76-89, 2012. Available: https://scielo.isciii.es/scielo.php?script=sci_abstract&pid=S0212-16112012000100009

[24] AOAC, "Official Methods of Analysis," *Association of Official Analytical*, no. 15, 1990, Accessed: Mar. 17, 2025. [Online]. Available: https://law.resource.org/pub/us/cfr/ibr/002/aoac.methods.1.1990.pdf

[25] M. J. G. Salgado *et al.*, "Impact of fiber-rich donkey milk yogurt on apparent viscosity and sensory acceptance," *LWT*, vol. 145, no. 1, pp. 111494, 2021. https://doi.org/10.1016/J.LWT.2021.111494

[26] I. Ocaña, "Caracterización fisicoquímica, nutricional y reológica de cultivos andinos infrautilizados" [Tesis de Grado, Universidad Técnica de Ambato]," Universidad Técnica de Ambato, Tungurahua, Ambato, 2019.

[27] INEN 2395, "Leche Fermentadas," *Norma Técnica Ecuatoriana* , no. 07, 2011, Accessed: Jan. 23, 2025. [Online]. Available: https://es.scribd.com/document/409014254/Leche-Yogurt

[28] M. Cuadros, "Atributos Sensoriales," *SCRIBD*, 2018, Accessed: Apr. 20, 2022. [Online]. Available: https://es.scribd.com/document/160682506/ATRIBUTOS-SENSORIALES#fullscreen&from_embed

[29] L. Taramona-Ruiz, V. Quispe-Wong and M. Huatuco-Lozano, "Evaluación sensorial de un salami con extracto de un colorante en base de Ayrampo (Opuntia soehrensii)," *Revista de Investigaciones de la Universidad Le Cordon Bleu*, vol. 11, no. 1, pp. 17-29, 2024. https://doi.org/10.36955/RIULCB.2024V11N1.002

[30] F. Afiati, G. Priadi and F. Setiyoningrum, "The improvement of functional food in yogurt enriched with purple sweet potato (Ipomea batatas var. Ayamurasaki)," *J Indones Trop Anim Agric*, vol. 43, no. 2, pp. 159-168, 2018. https://doi.org/10.14710/JITAA.43.2.159-168

[31] T. Pramanik, M. A. R. Mazumder, J. F. Jany, S. I. Akash, A. Rahman and M. K. H. Bhuiyan, "Functional yogurt: An approach to fortify yogurt by polyphenols extracted from Bengal currant," *Applied Food*

Research, vol. 5, no. 1, pp. 100715, 2025. https://doi.org/10.1016/J.AFRES.2025.100715

[32] Y. Feng, L. Niu, D. Li, Z. Zeng, C. Sun, and J. Xiao, "Effect of calcium alginate/collagen hydrolysates beads encapsulating high-content tea polyphenols on quality characteristics of set yogurt during cold storage," *LWT*, vol. 191, no. 1, pp. 115608, 2024. https://doi.org/10.1016/J.LWT.2023.115608.

[33] R. Qadir, W. N. A. Wan Mohamad Nasir, A. B. Azmi, S. Fatima, N. Mehmood, and A. S. Meor Hussin, "An insight into plant-based yogurts: Physicochemical, organoleptic properties and functional food aspects," *Journal of Food Composition and Analysis*, vol. 143, no. 1, p. 107578, 2025. https://doi.org/10.1016/J.JFCA.2025.107578.

[34] S. Priatni, A. F. Devi, L. B. S. Kardono, and V. Jayasena, "QUALITY AND SENSORY EVALUATIONS OF TEMPE PREPARED FROM VARIOUS PARTICLE SIZES OF LUPIN BEANS [Evaluasi Sensorik dan Kualitas Tempe dari Kacang Lupin Berbagai Ukuran Partikel]," *Jurnal Teknologi dan Industri Pangan*, vol. 24, no. 2, pp. 209–209, 2013. https://doi.org/10.6066/JTIP.2013.24.2.209.

[35] E. Villacrés and C. M. Rosell, "Kinetics of solid-state fermentation of lupin with Rhizophus oligosporus based on nitrogen compounds balance," *Food Biosci*, vol. 42, no.1, pp. 101118, 2021. https://doi.org/10.1016/J.FBIO.2021.101118.

[36] A. Chawafambira and T. Z. Jombo, "The effect of herbal Lippia javanica extracts on the bioactive content, functional properties, and sensorial profile of biofortified-orange maize based fermented maheu," *Applied Food Research*, vol. 4, no. 1, pp. 100367, 2024. https://doi.org/10.1016/J.AFRES.2023.100367.

[37] V. Vicent, "Influence of banana powder on proximate composition, physicochemical and rheological properties of soy yoghurt," *Applied Food Research*, vol. 4, no. 2, pp. 100450, 2024. https://doi.org/10.1016/J.AFRES.2024.100450.

[38] I. Bourouis, D. J. McClements, C. Chen, H. Li, Z. Pang, and X. Liu, "Formulations and evaluations of structural and physico-chemical properties of soy yogurts: Effect of incorporating soy protein isolate/chitosan complexed microgels," *LWT*, vol. 206, no. 1, pp. 116569, 2024. https://doi.org/10.1016/J.LWT.2024.116569

[39] Z. Pang, R. Xu, T. Luo, X. Che, N. Bansal and X. Liu, "Physiochemical properties of modified starch under yogurt manufacturing conditions and its relation to the properties of yogurt," *J Food Eng*, vol. 245, no1, pp. 11-17, 2019. https://doi.org/10.1016/J.JFOODENG.2018.10.003

[40] R. Dong *et al.*, "Enrichment of yogurt with carrot soluble dietary fiber prepared by three physical modified treatments: Microstructure, rheology and storage stability," *Innovative Food Science & Emerging Technologies*, vol. 75, pp. 102901, 2022. https://doi.org/ 10.1016/J.IFSET.2021.102901

[41] J. Arriaga and J. Gonzalo, "Control de calidad fisicoquímica, microbiológica y probiótica de yogurt artesanal de mercados de los distritos de Santiago y Cusco, 2023," Universidad Nacional San Antonio, 2024. Accessed: Feb. 06, 2025. [Online]. Available: https://repositorio.unsaac.edu.pe/handle/20.500.12918/8521

[42] K. Poma Zanabria and F. Y. Rojas Calderón, "Actividad antibacteriana in vitro del extracto etanólico de semillas de Lupinus mutabilis sweet (Tarwi) frente A Escherichia Coli ATCC 25922," Universidad María Auxiliadora, 2023. Accessed: Feb. 21, 2025. [Online]. Available: https://repositorio.uma.edu.pe/bitstream/handle/20.500.12970/1665/TESIS%20POMA-ROJAS.pdf?sequence=1

[43] M. Cerna, "Uso de bebidas vegetales de Chocho (Lupinus mutabilis), Garbanzo (Cicer arietinum) y Amaranto (Amaranthus) como sustitución de la leche de vaca en yogurt.," Universidad Técnica de Babahoyo, 2024. Accessed: Feb. 21, 2025. [Online]. Available: http://dspace.utb.edu.ec/handle/49000/16060

[44] J. Zhang, A. Perez-Gavilan and A. C. Neves, "Fortification of dairy-free yoghurt with bioactive protein from solid-state fermented brewers' spent grain," *Applied Food Research*, vol. 5, no. 1, pp. 100833, 2025. https://doi.org/10.1016/J.AFRES.2025.100833

[45] E. Villacrés, M. B. Quelal, X. Jácome, G. Cueva and C. M. Rosell, "Effect of debittering and solid-state fermentation processes on the nutritional content of lupine (Lupinus mutabilis Sweet)," *Int J Food Sci Technol*, vol. 55, no. 6, pp. 2589-2598, 2020. https://doi.org/10.1111/IJFS.14512

ENFOQUE UTE REVISTA
Facultad Ciencias de la Ingeniería e Industrias
RESEARCH ARTICLE
ENFOQUE UTE, VOL. 16, NO. 3, pp. 52-59, E-ISSN: 1390-6542
RECEIVED JANUARY 26, 2025; ACCEPTED APRIL 23, 2025; PUBLISHED ONLINE JULY 1, 2025;
DATA OF CURRENT VERSION JULY 1, 2025; PUBLISHED IN VOLUME 16, ISSUE 3 (JULY 2025).

Evaluation of weed control techniques in Schizolobium parahyba plantations: Impact on sustainable natural regeneration

Stephanny Hillary Briones Zambrano[1], Jorge Manuel Jara Minalla[2], Víctor Trajano Gallo Fonseca[3], Juan Rubén Briones Magallanes[4], Fabricio Rolando Marcillo Vera[5*]

***Abstract* — The study evaluated the initial growth of Schizolobium parahyba under different weed control techniques, both crown and parallel. A 2A × 3B completely randomized block design was used, where A represents the distribution of vegetative material (around the canopy and parallel to the planting lines) and B the canopy radius (50 cm, 75 cm and 100 cm). Twelve treatment plots and one control plot were established. Height, diameter, number of leaves and survival were measured from the second month onwards, with a periodicity of 30 days. Among the findings. Survival did not depend on the radius or distribution of the material, since the control plot did not show the lowest yield. It is noteworthy that weed control favored growth, being the treatment with 50 cm crowns and vegetative material around them the one that obtained the best results in all the variables analyzed.**

***Keywords:* Schizolobium parahyba; dasometric variables; seedling survival; weeds; sustainable natural regeneration.**

***Resumen* — El estudio evaluó el crecimiento inicial de Schizolobium parahyba bajo diferentes técnicas de control de malezas. Se utilizó un diseño de bloques completamente aleatorizados 2A × 3B, en el que A representa la distribución del material vegetativo (alrededor del dosel y paralelo a las líneas de plantación) y B el radio del dosel (50 cm, 75 cm y 100 cm). Se establecieron doce parcelas de tratamiento y una de control. La altura, el diámetro, el número de hojas y la supervivencia se midieron a partir del segundo mes, con evaluaciones cada 30 días. La supervivencia no dependió del radio ni de la distribución del material, ya que la parcela control no mostró el menor rendimiento. Sin embargo, el control de malas hierbas favoreció el crecimiento, siendo el tratamiento con coronas de 50 cm y material vegetativo a su alrededor el que mejores resultados obtuvo en todas las variables analizadas.**

***Palabras Clave:* Schizolobium parahyba; variables dasométricas; supervivencia de plántulas; arvenses; regeneración natural sostenible.**

I. INTRODUCTION

PACHACO (Schizolobium parahyba), a leguminous species native to the tropical rainforests of South America, has attracted the attention of researchers and foresters for its potential and rapid growth. The diversity of use, economic value and land management of the species has promoted the expansion of its cultivation in the recovery of degraded areas [1], [2], [3]. Thus, in disturbed lands it can reach large dimensions in a short time, becoming an important species in forest ecology or agroforestry systems [4], [5], [6]. Studies have shown that its growth patterns are influenced by climatic conditions such as photoperiod, temperature and precipitation [7], [8].

Naturally, the great advantages of forest plantations are unbeatable, as long as there are favorable conditions [9]. Within this framework, Piotto [10] found that S. parahyba presented excellent growth under mixed conditions, however, within his findings he determined that the variation within the same plot generated high mortality rates in pure and mixed plantations. Hence, in [11], [12] the various factors that influenced the growth of pachaco were studied, such as: soil type, water availability, competition with other species, height, stem diameter and climatic conditions.

From other perspectives, the growth of Schizolobium parahyba is discussed in different aspects due to its expansion as a tropical species. For example: in [13], [14] , topics related to root depths were studied, since the influence of its growth is fundamentally rooted in climatic conditions. In [15] the quality

* *Corresponding autor:* fmarcillo@itsjapon.edu.ec
1. Stephanny Hillary Briones Zambrano is with State Technical University of Quevedo, Quevedo, Ecuador; Master's Degree. E-mail: stephanny.briones2016@uteq.edu.ec, ORCID number https://orcid.org/0009-0001-9799-5803
2. Jorge Manuel Jara Minalla is with State Technical University of Quevedo, Quevedo, Ecuador; Master's Degree. E-mail: jorge.jara2015@uteq.edu.ec, ORCID number https://orcid.org/0009-0000-8917-707X
3. Víctor Trajano Gallo Fonseca is with State Technical University of Quevedo, Quevedo, Ecuador; Master's Degree. E-mail: vgallo@uteq.edu.ec, ORCID number https://orcid.org/0000-0001-6588-1708
4. Juan Ruben Briones Magallanes is with Ministry of Education, District 23D01, Santo Domingo, Ecuador; Biologist. E-mail: ruben.briones@educacion.gob.ec, ORCID number https://orcid.org/0009-0002-3614-1211
5. Fabricio Rolando Marcillo Vera is with Japan Higher University Institute, Quito, Ecuador; PhD in Information and Communication Technologies. E-mail: fmarcillo@itsjapon.edu.ec, ORCID number https://orcid.org/0000-0003-2628-9167

DOI: https://doi.org/10.29019/enfoqueute.1128
Associate Editor: *Edinson Daniel Anzules*

of Schizolobium Parahyba (vell.) S.F. Blake seedlings was evaluated under different levels of shade in nursery stages. Despite the fertilization limitations in the trial, it was not conditioned for afforestation and restoration purposes. The quality index obtained (0.33 with 0 % shade level) was above the minimum threshold (0.22). In [16], vegetative propagation by field grafting and mound layering techniques was studied. Given the high survival rate of grafted plants indicated the success of graft union, differentiation of new vascular tissue and formation of a vascular system for vegetative growth. Mound rooting was also satisfactory as it was treated with IBA (indole-3-butyric acid). While in [17] growth regulators for multiplication, elongation and rooting in vitro were evaluated in order to obtain information on cloning via micropropagation of Schizolobium parahyba. Their results showed that in in vitro multiplication and elongation, the higher the dose of cytokinin applied, the higher the shoot proliferation per explant and the lower the mean explant length.

The focus of this work is on seedling growth and competition with other species (weeds) for soil nutrients and its impact on sustainable natural regeneration. Hence, the proposed approach is related to similar works developed in [11], [12], [16]. The added value of the proposal is the self and ecological sustainability of the seedlings. In the work presented here we will induce different configurations of arvenses (circular and parallel) that will be used to assess the level of survival of S. parahyba. In this regard, the control by means of arbenses was defined both in the formation of crowns (circles) and in the distribution of vegetative material, its application allowed estimating the survival of seedlings in plantations of S. parahyba. As the main initial result, it was possible to verify by means of Tukey's test that the survival level has a high sustainable regeneration when the crown radius is 50 and 75 cm.

The hypothesis proposed for this work is: There are no significant differences in the growth and development of S. parahyba in the initial stage of planting, in the face of weed control (weed control). The main objective of this work is to examine the different treatments of weed control techniques to determine the adequate conditions for the growth of Schizolobium parahyba. Therefore, the research questions that answer the objective are: i) What effect do weed control techniques have on initial growth and survival; ii) Which treatment has been effective in survival; iii) Which treatment in statistical terms was determinant for survival; iv) Which treatment in statistical terms was determinant for survival; v) Which treatment has been effective in survival; vi) Which treatment in statistical terms was determinant for survival; vii) Which treatment has been effective in survival; and viii) Which treatment in statistical terms was determinant for survival.

The paper is organized as follows: The first section, is related to the introduction and related works. The second section establishes the work methodology and the application of statistical methods for the verification of the assumptions of weed control in plantations. The third section refers to the results of the study. The fourth section is associated with the discussion of the findings and the contrast with analogous works. The fifth section contains the conclusions of the study.

II. METHODOLOGY

A. Study area

The present study was carried out in the district of "Agua Clara" belonging to the Quinindé Canton of the Province of Esmeraldas, Ecuador. The geographical coordinates are: Latitude: 0.333333, Longitude: -79.2833, Altitude: 85 meters above sea level. The climate of the area described is rainy-tropical, its average temperature is 27 ° Celsius. A wet day is a day with at least 1 millimeter of liquid or liquid equivalent precipitation. The probability of a wet day during the summer decreases very fast, starting at 37 % and ending at 12 %. For reference, the highest probability of the year of having a wet day is 78 % on February 10, and the lowest probability is 9 % on August 7.

The probability of a given day being wet decreases in June, and decreases from 99 % to 94 % over the course of the month. For reference, on April 12, the hottest day of the year, there are sultry conditions 100 % of the time, while on September 3, the least sultry day of the year, there are sultry conditions 65 % of the time.

B. Experimental design

To carry out the study, completely randomized blocks were designed (DBCA), with a factorial arrangement of the form 2A x 3B with two replications and a control plot, where A is the form of distribution of the vegetative material produced at the time of clearing the land, which was located around the crown and parallel to the planting lines; and, on the other hand, B is the radius of the crowns which was 50 cm, 75 cm and 100 cm (See Annexes, Table V). Then, 13 plots were established: 12 corresponding to the treatment and one for control. The plot measures were 25 m x 20 m (500 m²), 30 individuals per plot. The S. parahyba plantation was established at a distance of 3 x 4 m, in a total area of 6.6 hectares. That is, the area used was 6500 m² and 390 individuals. On the other hand, and no less important was the weed control carried out mechanically using a weed cutter (Moto scythe) at 60-day intervals. In the case of the control plot, it was operated in the usual way by the owner, with intervals of three or four months.

C. Interventions

In order to isolate the effect of weed control on the dasometric variables of pachaco seedlings and to evaluate the impact of different crown radii on growth, an experimental design was established with four replicates for each treatment. At the beginning of the study, crowns of 50, 75 and 100 cm radius were formed around each seedling, eliminating competing vegetation manually. At the same time, a weed control program was implemented with a variable frequency of 30 to 60 days, depending on climatic conditions. The plant material resulting from both practices (weed control and crown formation) was distributed parallel to the planting lines and on the edges of the crowns, avoiding regrowth and minimizing its impact on seedling growth.

D. Methods for evaluation

For the estimation of survival, it was necessary to count the number of standing individuals for each treatment in both the initial and final stages. According to Eq.1 [18] the level of survival can be determined from the following mathematical expression:

$$p = \frac{\sum_{i=1}^{n} a_i}{\sum_{i=1}^{n} m_i} \cdot 100 \qquad (1)$$

Where: $\sum_{i=1}^{n}$ is the sum of the data according to “a” or “m”; p: is the proportion of live trees; is the number of live plants in sample site “i”; is the number of live and dead plants in sample site “i”. When approaching the statistical test for the verification of the treatments, they were approached in two phases: The first, descriptive analysis of the dasometric variables (diameter, height and number of leaves) was used. The second, using analysis of variance (ADEVA) to compare the means and verify the existence of significant differences between treatments, as shown in Table I. For this purpose, the Tukey test [19] was applied to compare individual means (p<=0.05). The experimental data were tabulated and processed with the IBM-SPSS-Stastistics 22 program (Free Trial Version).

TABLE I
ANALYSIS OF VARIANCE FOR A TWO-FACTOR EXPERIMENTAL DESIGN IN THE APPLICATION OF TREATMENTS IN THE SPECIES S. PARAHYBA

Source of Variation	**Sum of Squares**	**Degrees of Freedom**	**Mean Squares**	**Estimated F* value**
Treatments	SCT	$k-1$	$S_1^2 = \frac{SCT}{k-1}$	$f_1 = \frac{S_1^2}{S^2}$
Blocks	SCB	$b-1$	$S_2^2 = \frac{SCB}{b-1}$	
Residual	SCE	$(k-1)(b-1)$	$S^2 = \frac{SCE}{(k-1)(b-1)}$	
Total	STC	$kb-1$		

SCT: Sum of squares for treatments; **SCB:** Sum of squares for blocks. **SCE:** Sum of squares for error; **STC:** Total sum of squares.

III. RESULTS

In response to the research questions posed and objectives established in this work. The main results obtained can be highlighted. The survival rate, generic growth and the effect of weed control techniques on the pachaco plantation were studied.

The first research question was answered: What effect do weed control techniques have on initial growth and survival? During the first years, pachaco shows exceptionally rapid growth in height and diameter, which allows it to reach considerable heights in a short time. Growth in height, diameter and number of leaves. Pachaco (Schizolobium parahyba) is a fast-growing and highly adaptable forest species. Figures 1, 2 and 3 are the average values collected from this work. The data can be found in the annexes section described in Table VI, Table VII and Table VIII.

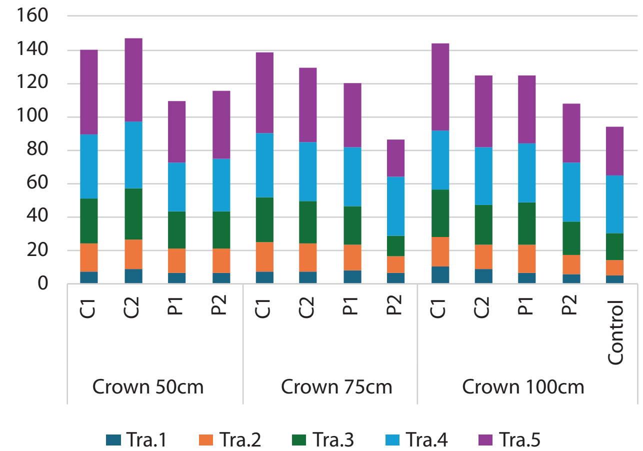

Fig. 1. Projection of the average base diameter, the abscissa shows the arrangements of the vegetative material. C corresponds to the crown arrangement and P to the parallel vegetative arrangement.

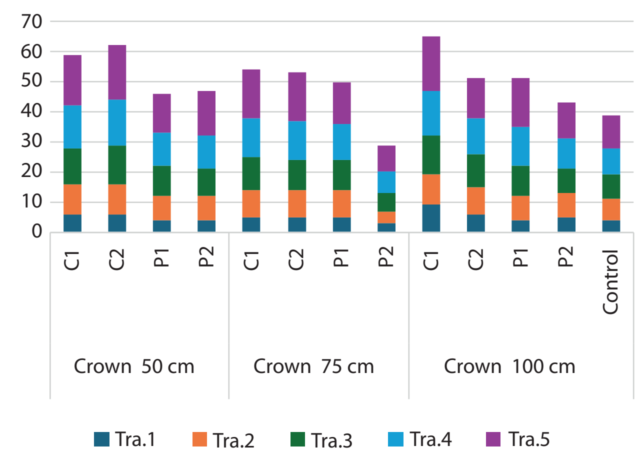

Fig. 2. Projection of the average height, the abscissa shows the arrangement of the vegetative material. C corresponds to the crown arrangement.

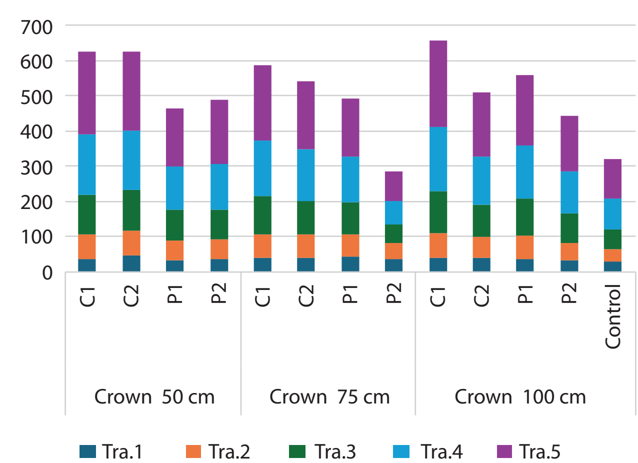

Fig. 3. Projection of the number of leaves, the abscissa shows the arrangement of the vegetative material. C corresponds to the crown arrangement and P to the parallel vegetative arrangement.

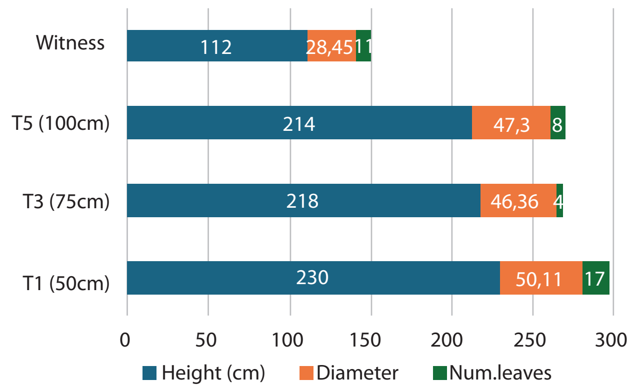

Fig. 4. Dasometric results of pachaco seedlings.

Figure 4 shows the dasometric summary of the field work carried out, the horizontal bars correspond to each treatment, with treatment 1 with a 50 cm crown being the one that reached the greatest height, diameter and number of leaves. However, Tables II, III and IV, where the calculation of Tukey's statistics is presented, will allow us to know the treatment with the best performance.

TABLE II
AVERAGE HEIGHT (CENTIMETERS) OF S. PARAHYBA RELATED TO CROWN RADIUS AND DISTRIBUTION OF VEGETATIVE MATERIAL

Tukey's test for height (centimeters)				
Treatments	**Subset for alpha = 0,05**			
	1	**2**	**3**	**4**
Tra.1	230.45 a↑			
Tra.3		214.47 ab		
Tra.5		203.58 abc		
Tra.6			183.28 bc	
Tra.2			174.97 c	
Tra.4				128.14 d
Witness				111.96 d

↑ Means with different letters show significant statistical differences according to Tukey's test *p > 0,05*.

It can be observed in Table II that, after 120 days of data recording, the height shows significant statistical differences between each treatment, with the influence of both crown size and the distribution of vegetative material on the increase in height. On the other hand, the control plot was the one that presented the lowest growth in height with an average of 111.96 cm, although the average growth was 128.14 cm in individuals of the plot of Treatment 4, these two plots had a statistically similar behavior.

Likewise, the plot with Treatment 1, the average height was 230.45 cm, this treatment being the one with the highest growth in height compared to the rest of the treatments; however, it behaves statistically similar to the plot with Treatment 5, which had a height of 214.17 cm at the end of the data collection.

TABLE III
MEAN DIAMETER (MILLIMETERS) OF S. PARAHYBA RELATED TO CROWN RADIUS AND DISTRIBUTION OF VEGETATIVE MATERIAL

Tukey's test for diameter (millimeters)			
Treatments	**Subset for alpha = 0,05**		
	1	**2**	**3**
Tra.1	50.11 a↑		
Tra.3	47.3 a		
Tra.5	46.36 a		
Tra.6		39.54 b	
Tra.2		28.45 c	
Tra.4			38.93 b
Witness			31.2 c

↑ Means with different letters show statistical differences according to Tukey's test at p > 0.05 probability.

Table III shows that, after 120 days from the beginning of data recording, plant diameter is different for all treatments. In addition, it is noted that all plots show significant statistical differences between them. This suggests that there is influence of both crown size and vegetative material distribution in relation to the increase of the dasometric variable, which in this case plant diameter.

It is highlighted that the control plot registered the lowest growth in diameter, with an average of 28.45 mm, despite the fact that the average growth was 31.2 mm in the plots with Tra.4, these two plots behaved statistically similar. In addition, it is mentioned that the plot with Tra.1, had a diameter growth of 50.11 mm, in this plot shows a statistically similar behavior to the plot with Tra.5, which had a diameter of 47.30 mm and 46.36 mm (Table III).

TABLE IV
MEAN NUMBER OF LEAVES FOR S. PARAHYBA RELATED TO CROWN RADIUS AND DISTRIBUTION OF VEGETATIVE MATERIAL.

Tukey's test for diameter (millimeters)				
Treatments	**Subset for alpha =0.05**			
	1	**2**	**3**	**4**
Tra.1	17.26 a↑			
Tra.3		16.28 ab		
Tra.5		15.58 abc		
Tra.6			14.3bc	
Tra.2			1391 c	
Tra.4				11.43 d
Witness				10.67 d

↑ Means with different letters show statistical differences according to Tukey's test.

Table IV provides a detailed description of how different treatments, specifically crown ratio and vegetative material distribution, influenced the number of leaves after a 120-day cycle, Furthermore, it is highlighted that the configured plots presented statistically significant differences. Hence, the influence of both crown size and vegetative material distribution in relation to the increase in leaf quantity is estimated.

On the other hand, the control plot (control) presented less quantity of leaves with a mean of 10.67 leaves, although the mean growth in the individuals belonging to the plots with a crown size of 75 cm with distribution of the vegetative material parallel to the planting line (Tra.4) was 11.43; these two plots behaved statistically the same. Similarly, the plot with a crown size of 50 cm, with distribution of vegetative material around the crown (Tra.1), was 17.26; this plot behaved statistically similar to the plot with a crown size of 75 cm and 100 cm with distribution of vegetative material around the crown (Tra.3 and Tra.5), with a number of leaves of 16.28 and 15.58 at the end of the data collection.

As an answer to the third question posed, the Tukey statistical test with a p-value > 0.05 shows that treatment 1 stands out in height, diameter and number of leaves. In this sense, the treatments applied in this study show that it has a significant effect on the growth and development of Schizolobium parahyba seedlings in its initial stage, therefore, the hypothesis raised in this research is rejected.

IV. DISCUSSION

Plant survival is influenced by weed control and favorable conditions for pachaco growth. For this reason, it is essential to implement integrated management that combines preventive, cultural, mechanical and, in some cases, chemical methods. The use of crowns and vegetative material as part of weed control in the research plots maintained constant pachaco survival. Thus, the control plot had a slight decrease in its survival values compared to the treatments.

Analogous to our results in [20], the survival of Eucalyptus grandis trees was studied where the type of arvense was similar to that used in our study. It was specified that survival with competing plant species in plantations has little effect. However, the same type of weed in the results of this study shows that the survival rate in the control plot was 80 %. While, the other plots showed lower results 58.33 % and 65 % respectively. In spite of the fact that ant attack was an evident factor in the plots.

Another factor, no less important and which influenced the survival rate of forest plantations, was the stress generated to the seedlings due to water shortage. In addition to the copious presence of weeds, which generally compete with the plantations in their initial state for water and this negatively affects their growth. The plots at the beginning of the experimental record had a height between 33 to 40 cm, and applying the different distributions of vegetative material, the record at 120 days after the first record of the research (180 days from the establishment of the plantation), the height was found to be between 98 to 172 cm. Likewise, in [21], [13] showed good survival and excellent growth rates during the first year of establishment of the Schizolobium parabyba plantation, although later the trees die for no apparent reason, but for lack of adaptation to the conditions and competitions of the plantation.

As observed in the field, the natural regeneration of Schizolobium parabyba grows excellently and normally forms isolated trees or in small groups. Thus, the realization of crowns and their respective arrangement of vegetative material resulting from weed control is a factor that benefits the height growth of the species. In this regard, at the conclusion of the research, each treatment exhibited a larger diameter than the control plot, which reached an average of 28.45 mm. This set of evidence is close to the results obtained by Melo [22] where he stated that the higher ratios observed at lower planting density are favorable conditions for growth, since there is less competition for soil nutrients and water.

On the other hand, the diametric study of the seedlings in the plots at the beginning of this work showed diameters ranging from 6.25 to 9.58 millimeters. However, when the crowns and subsequent application of different arrangements of the vegetative material resulting from weed control were carried out 120 days after the first record of the research (210 days after the establishment of the plantation), a diametric range was observed in the seedlings from 30.45 mm to 50.11 mm, that is, in the first case the diameter increased by 487 % and, in the second, it increased by 523 %. It is notorious that applying weed control, in general, increases diameter growth.

Among the factors of importance in plantations of S. parahyba, diameter was considered relevant. Chronologically, two stages were observed from the initial stage: 60 and 90 calendar days. In the first section, there was an increase in diameter where the mean was 199 % (7.67 mm increased to 15.29 mm). In the second tranche, the mean compared to the control plot increased by 178 % (5.20 mm increased to 9.29 mm). These findings clarify that establishing plots with different crowns and distribution of vegetative material favors the increase in diameter due to the applied weed control. When comparing these evidence, it stands out, for example, that a weak control of weeds leads to a loss of plantation diameter. According to [23], the increase in diameter obtained in the same sections was 119 %. However, in the work presented here, these values are exceeded between 6 and 8 times.

The number of leaves of the plots with different crown sizes and different arrangements of vegetative material obtained values between 14 and 17, which were higher than the control plot that obtained an average of 11 leaves. In this sense, Carranza-Patiño [13] confirms that the increase in the number of leaves and biomass is a significant indicator of healthy plant growth. In addition, Borda [24] indicated that the number of leaves increases with respect to the weed control (12 leaves). While, those with higher intensity of weed control averaged between 17 and 18 leaves.

On the other hand, Quiroz [25] established a direct correlation between leaf density and plant growth vigor. A greater number of leaves increases photosynthetic capacity and transpiration surface, which stimulates the development of a more extensive root system. The results of the research presented here corroborate this statement, showing a positive relationship between the number of leaves and the growth in height and diameter of the plants. This suggests that leaf density is a reliable indicator of the growth and development potential of plant species.

The survival rate did not depend on the treatments applied in this research, this is reflected due to the variability of this and that the control plot did not obtain the lowest survival record, when compared with the different treatments applied, however there was an attack of ants of the genus Att, which is a relevant factor that could have influenced the survival of the seedlings, this highlights the importance of considering and properly manage the factors that may affect the ability of seedlings to establish and develop.

As a limitation to this research, it was necessary to consider as part of the treatments the level of vulnerability of the seedlings. For example: ants of the genus Att could be behind the level of survival [20].

V. CONCLUSIONS

In response to the research questions and hypotheses posed. The dasometric variables, such as diameter, height and number of leaves. They were determinant for the evaluation of the different weed control treatments. Therefore, the use of crowns with different radii and distribution of vegetative material are determinant for the growth and development of pachaco plants. The control plot lacked low yield compared to the rest. Therefore, the impact of sustainable regeneration through weed control was positive by avoiding dependence on chemical herbicides. The 50 cm radius plot had a better yield. One of the limitations of this work was related to the constant monitoring of possible biotic and abiotic threats. As future work, an integrated management of external factors is suggested to permanently monitor possible biotic and abiotic threats to minimize their impact on the plantations.

APPENDIX

A. Data Analysis

TABLE V
TYPES OF TREATMENTS ESTABLISHED
FOR SCHIZOLOBIUM PARAHYBA PLANTATION

Trataments	Crown radius (cm)
Tra.1	50*
Tra.2	50**
Tra.3	75*
Tra.4	75**
Tra.5	100*
Tra.6	100**
Witness	Habitual

* Distribution of vegetative material around the crown.

** Distribution of vegetative material parallel to the planting line.

TABLE VI
AVERAGE GROWTH OF BASE DIAMETER IN MILLIMETERS,
C1 ARRANGEMENT OF VEGETATIVE MATERIAL
IN CIRCULAR FORM AND P1 ARRANGEMENT OF VEGETATIVE
MATERIAL IN PARALLEL FORM.

Crown	Config	Tra.1	Tra.2	Tra.3	Tra.4	Tra.5
50cm	C1	7.27	16.99	27.09	38.18	50.13
	C2	9.19	17.81	29.93	40.01	50.1
	P1	6.97	14.07	22.1	29.48	36.87
	P2	6.58	14.34	22.72	31.6	40.49
75cm	C1	7.61	17.25	27.43	37.77	48.12
	C2	7.81	16.5	25.34	34.97	44.6
	P1	8.26	15.22	23.17	34.97	38.42
	P2	6.69	9.91	12.23	34.97	22.49
100cm	C1	10.27	17.97	28.43	34.97	51.97
	C2	8.9	14.68	23.48	34.97	42.62
	P1	6.76	16.7	25.77	34.97	40.68
	P2	5.74	12	19.77	34.97	35.69
	Control	5.2	9.29	15.78	34.97	28.45

The values presented in Tables V and VI specify the configuration and average values of the treatments used. Thus, Table V shows the configuration of each of the treatments designed for the pachaco study process. Table VI details the configurations made at the crown level and the arrangement of the vegetative material in parallel.

B. Data collection of the different dasometric variables under study.

TABLE VII
AVERAGE GROWTH IN HEIGHT, C1 ARRANGEMENT
OF THE VEGETATIVE MATERIAL IN A CIRCULAR SHAPE
AND P1 ARRANGEMENT OF THE VEGETATIVE MATERIAL
IN A PARALLEL SHAPE

Crown	Config	Tra.1	Tra.2	Tra.3	Tra.4	Tra.5
50cm	C1	35	69	113	173	237
	C2	45	70	116	170	223
	P1	33	55	86	126	165
	P2	35	56	83	133	183
75cm	C1	40	67	106	160	215
	C2	40	65	97	145	193
	P1	43	62	91	129	166
	P2	36	45	51	68	84
100cm	C1	38	70	121	183	245
	C2	40	58	91	138	184
	P1	36	66	105	153	197
	P2	31	51	84	120	157
	Control	27	36	58	86	112

Fig. 5. Measurement of tree height.

Fig. 6. Measurement of tree diameter.

Fig. 5 shows the person measuring the height of the tree using a common flexometer. While in Fig. 6 the diameter of another tree is taken using a digital caliper. The collected values are added to databases that serve as input data for applying statistical techniques. As a follow-up of this activity, the data shown in Tables VII and VIII present the average growth in height of pachaco (Table VII) in both types of arrangements. On the other hand, in Table VIII the results refer to the amount of fallen leaves in the arrangements and treatments.

TABLE VIII
NUMBER OF LEAVES, C1 ARRANGEMENT OF VEGETATIVE MATERIAL IN A CIRCULAR SHAPE AND P1 ARRANGEMENT OF VEGETATIVE MATERIAL IN A PARALLEL SHAPE

Crown	**Config**	**Tra.1**	**Tra.2**	**Tra.3**	**Tra.4**	**Tra.5**
50 cm	C1	6	10	12	14	17
	C2	6	10	13	15	18
	P1	4	8	10	11	13
	P2	4	8	9	11	15
75 cm	C1	5	9	11	13	16
	C2	5	9	10	13	16
	P1	5	9	10	12	14
	P2	3	4	6	7	9
100 cm	C1	9	10	13	15	18
	C2	6	9	11	12	13
	P1	4	8	10	13	16
	P2	5	8	8	10	12
	Control	4	7	8	9	11

REFERENCES

[1] M. I. Castro Cordeiro, M. C. M. Oliveira Jr, A. B. Gazel Filho, P. L. C. Barros and O. A. Oliveira, "Crecimiento del Schizolobium parahyba subesp. amazonicum cultivado en presencia de Ananas comosus subesp. Erectifolius en Pará, Brasil," *Agrociencia*, vol. 50, no. 1, pp. 79-88. 2016.

[2] G. M. Olmedo, C. Fontana and J. M. Oliveira, "Primary and secondary growth phenology of Schizolobium parahyba (Vell.) Blake at different time scales,". *Dendrochronologia*, vol. 72. 2022. https://doi.org/10.1016/j.dendro.2022.125921

[3] F. M. Benitez Romero, T. de Nazaré Oliveira Novais, L. A. G. Jacovine, E. B. Bezerra, R. B. de Castro Lopes, J. S. de Holanda, E. F., Reyna and P. M. Fearnside, "Wood basic density in large trees: impacts on biomass estimates in the Southwestern Brazilian Amazon. *Forests*, vol. 15, no. 5, 2024. https://doi.org/10.3390/F15050734

[4] C. Valarezo, M. A. Villamagua, R. M. Mora, H. Maza, W. Wilcke and C. Nieto, "Respuesta del pachaco (Schizolobium parahybum vell. conc) y la melina (Gmelina arbórea roxb.) a la aplicación de biocarbón y fertilización en el sur de la Amazonía ecuatoriana," *Bosques Latitud Cero,* vol. 6, no. 1, pp. 77-89, 2017. Available: https://revistas.unl.edu.ec/index.php/bosques/article/view/183

[5] R. Akter, M. K. Hasan, K. H. Kabir, D. Darr and N. A. Roshni, "Agroforestry systems and their impact on livelihood improvement of tribal farmers in a tropical moist deciduous forest in Bangladesh," *Trees, Forests and People,* vol. 9, 2022. https://doi.org/10.1016/J.TFP.2022.100315

[6] Y. L. de O. Salomón, J. Georgin, D. S. P. Franco, M. S. Netto, D. G. A. Piccilli, E. L. Foletto, C. Manera, M. Godinho, D. Perondi and G. L. Dotto, "Development of activated carbon from Schizolobium parahyba (guapuruvu) residues employed for the removal of ketoprofen," *Environmental Science and Pollution Research*, vol. 29, no. 15, pp. 21860-21875, 2022. https://doi.org/10.1007/s11356-021-17422-5

[7] L. A. B. de Oliveira, G. S. Alves, C. L. P. Resende, D. D. C. Carvalho and F. Rodrigues, "Schizolobium parahyba var. amazonicum seedling growth by Trichoderma spp. strains under nitrogen rates. *Bioscience Journal,* vol. 40, 2024. https://doi.org/10.14393/BJ-V40N0A2024-63032

[8] M. I. C. C. Cordeiro, A. B. G. Filho, O. A. Lameira and L. de A. Coimbra, "Eco-physiological evaluation of provenances of Schizolobium parahyba subsp. amazonicum in the moltingstage and its growth in the field," *Research, Society and Development*, vol. 10, no. 1, pp. e12410111551-e12410111551, 2021. https://doi.org/10.33448/RSD-V10I1.11551

[9] D. Minini, C. Amaral Reis, D. de Moura Borges Maria, K. Pontes Teixeira das Chagas, T. R., da Silva Lins, P. H. Gonzalez de Cademartori, G. Baptista Vidaurre and S. Nisgoski, "A review on the quality of wood from agroforestry systems," *Agroforestry Systems*, vol. 98, no. 3, pp. 715-737, 2024. https://doi.org/10.1007/S10457-023-00941-0

[10] D. Piotto, E. Víquez, F. Montagnini and M. Kanninen, "Pure and mixed forest plantations with native species of the dry tropics of Costa Rica: a comparison of growth and productivity," *Forest Ecology and Management*, vol. 190, no. 2-3, pp. 359-372, 2004. https://doi.org/10.1016/J.FORECO.2003.11.005

[11] J. O. R. Matos, D. de C. Mariano, Ângelo A. Ebling, C. F. de Oliveira Neto, I. de J. M., Viégas and R. S. Okumura, "Crescimento e qualidade de mudas de Schizolobium parahyba var. amazonicum em substratos fertilizados," *Revista Em Agronegócio E Meio Ambiente,* vol. 16, no. 3, pp. 1-12. https://doi.org/10.17765/2176-9168.2023v16n3e11221

[12] M. I. C. C. Cordeiro, A. B. Gazel Filho, O. A., Lameira and L. De A. Coimbra, "Eco-physiological evaluation of provenances of Schizolobium parahyba subsp. amazonicum in the moltingstage and its growth in the field," *Research, Society and Development, [S.l.]*, v. 10, n. 1, p. e12410111551, 2021. https://doi.org/10.33448/rsd-v10i1.11551. Accessed: 11 mar. 2025. Available: https://rsdjournal.org/index.php/rsd/article/view/11551.

[13] M. Carranza-Patiño, Y. Laz-Vera, R. J. Herrera-Feijoo, E. Jiménez-Romero, Á. Cedeño-Moreira and C. Chicaiza-Ortiz, "Plant growth-promoting rhizobacteria: a promising strategy to optimize the development of schizolobium parahyba," *Revista de Gestao Social e Ambiental,* vol. 18, no. 4, 2024. https://doi.org/10.24857/RGSA.V18N4-138

[14] L. F. Silva Dionisio, J. N. de Sousa, H. D. dos Santos, C. de Almeida Milhomem, A. da Silva and J. C. de Oliveira Junior, "Emergence and initial growth of Schizolobium parahyba var. amazonicum as a function of sowing depth in the amazon biome | Emergência e crescimento inicial de Schizolobium parahyba var. amazonicum em função da profundidade de semeadura no bioma amazônico," *Revista Brasileira de Ciencias Agrarias*, vol. 17, no. 4. 2022. https://doi.org/10.5039/agraria.v17i4a2298

[15] F. Meza Bone, J. Cachipuendo Castillo and W. Garcia Cox, "Calidad de plántulas de Schizolobium parahyba (Vell.) S.F. Blake bajo diferentes niveles de sombra en fase de vivero," *Agrosilvicultura y Medioambiente*, vol. 2, no. 2, 2025. Available: https://revistas.unesum.edu.ec/agricultura/index.php/ojs/article/view/48

[16] A. Sales, A. Xavier, H. N. Paiva, I. Wendling, G. A. dos Santos, M. A. Siviero and S. B. Vieira, "Vegetative propagation of Schizolobium parahyba var. amazonicum (paricá) using field grafting and mound layering techniques" [Propagação vegetativa de Schizolobium parahyba var. amazonicum (paricá) usando técnicas de enxertia e mergulhia de cepa], *Acta Amazonica,* vol. 54, no. 4, 2024. https://doi.org/10.1590/1809-4392202301262

[17] M. F. Mendes, B. V. Félix, I. Isernhagen, A. B. baldoni, Tardin, P. C. Flôres Júnior, A. de A.Tsukamoto Filho and L. C. de Moura, Propagação in vitro de Schizolobium parahyba var. Amazonicum. *Contribuciones a las Ciencias Sociales*, vol. 17, no. 7, p. e8283, 2024. https://doi.org/10.55905/revconv.17n.7-131

[18] CONAFOR (Comisión Nacional Forestal), "Manual básico de Practicas de reforestación". Coordinación General de Conservación y Restauración. Comisión Nacional Forestal. México. 66p. 2010.

[19] H. J. Keselman and J. C. Rogan, "The Tukey multiple comparison test: 1953-1976," *Psychological Bulletin*, vol. 84, no. 5, pp. 1050-1056, 1977. https://doi.org/10.1037/0033-2909.84.5.1050

[20] J. Villava, "Efecto de diferentes niveles de interferencia en la fila de plantación en parámetros de crecimiento de Eucaliptus grandis en Uruguay," *Sci. For., Piracicaba*, vol. 46, n. 119, pp. 473-482, set. 2018. https://doi.org/10.18671/scifor.v46n119.14

[21] J. C. Calvo-Alvarado, D. Arias and D. D. Richter, "Early growth performance of native and introduced fast growing tree species in wet to sub-humid climates of the Southern region of Costa Rica," *Forest Ecology and Management,* vol. 242, no. 2-3, pp. 227-235, 2007. https://doi.org/10.1016/j.foreco.2007.01.034

[22] L. E. L. Melo, C. J. Silva, T. P. Protásio, G. S. Mota, I. S. Santos, C. V. Urbinati, P. F. Trugilho and F. A. Mori, "Planting density effect on some properties of Schizolobium parahyba wood," *Maderas: Ciencia y Tecnología,* vol. 20, no. 3, pp. 381-394, 2018. https://doi.org/10.4067/S0718-221X2018005003901

[23] F. Panduro, "Preparación del sitio de plantación para Schizolobium parahybum (Vell) S.F. Blake, (pashaco)-2014". Escuela de Formación Profesional de ingeniería Forestal. Iquitos-Perú. 2014.

[24] C. Borda, "Efecto del control de malezas con herbicida y métodos mecánicos en el crecimiento inicial de Cedrela odorata L". Universidad Nacional del Centro del Perú. Facultad de Ciencias Forestales y del Ambiente. Huancayo- Perú. 2019.

[25] L Quiroz, E. García, M. Gonzales, P. Chung and H. Soto, "Vivero Forestal: Producción de plantas nativas a raíz cubierta". INFOR. Concepción-Chile. 2009.